Title:
Dark Matter Annihilation at the Galactic Center

Author:
Linden, Timothy Ryan

Acceptance Date:
2013

Series:
UC Santa Cruz Electronic Theses and Dissertations

Degree:
Ph.D., PhysicsUC Santa Cruz

Advisor:
Profumo, Stefano

Committee:
Jeltema, Tesla, Ritz, Steve

Permalink:
http://escholarship.org/uc/item/41d7v3qd

Abstract:

Copyright Information:

UNIVERSITY OF CALIFORNIA

SANTA CRUZ

DARK MATTER ANNIHILATION AT THE GALACTIC CENTER

A dissertation submitted in partial satisfaction of the
requirements for the degree of

DOCTOR OF PHILOSOPHY

in

PHYSICS

by

Tim Linden

June 2013

The Dissertation of Tim Linden
is approved:

_____

Professor Stefano Profumo, Chair

_____

Professor Tesla Jeltema

_____

Professor Steve Ritz

_____

Dean Tyrus Miller
Vice Provost and Dean of Graduate Studies

Table of Contents

List of Figures

List of Tables

Abstract

Dark Matter Annihilation at the Galactic Center

by

Tim Linden

Observations by the WMAP and PLANCK satellites have provided extraordinarily accurate observations on the densities of baryonic matter, dark matter, and dark energy in the universe. These observations indicate that our universe is composed of approximately five times as much dark matter as baryonic matter. However, efforts to detect a particle responsible for the energy density of dark matter have been unsuccessful. Theoretical models have indicated that a leading candidate for the dark matter is the lightest supersymmetric particle, which may be stable due to a conserved R-parity. This dark matter particle would still be capable of interacting with baryons via weak-force interactions in the early universe, a process which was found to naturally explain the observed relic abundance of dark matter today. These residual annihilations can persist, albeit at a much lower rate, in the present universe, providing a detectable signal from dark matter annihilation events which occur throughout the universe. Simulations calculating the distribution of dark matter in our galaxy almost universally predict the galactic center of the Milky Way Galaxy (GC) to provide the brightest signal from dark matter annihilation due to its relative proximity and large simulated dark matter density. Recent advances in telescope technology have allowed for the first multiwavelength analysis of the GC, with suitable effective exposure, angular resolution, and energy resolution in order to detect dark matter particles with properties

similar to those predicted by the WIMP miracle. In this work, I describe ongoing efforts which have successfully detected an excess in γ-ray emission from the region immediately surrounding the GC, which is difficult to describe in terms of standard diffuse emission predicted in the GC region. While the jury is still out on any dark matter interpretation of this excess, I describe several related observations which may indicate a dark matter origin. Finally, I discuss the role of future telescopes in differentiating a dark matter model from astrophysical emission.

Acknowledgments

I am in great debt to many people without whom this work never would have been completed. I'd first like to thank my many collaborators over the last five years: Brandon Anderson, Alexander Belikov, Eric Carlson, Ilias Cholis, Alessandro Cuoco, Jay Gallagher, Dan Hooper, Tesla Jeltema, Vicky Kalogera, Elizabeth Lovegrove, Andrea Prestwich, Stefano Profumo, Jeremy Sepinsky, Jennifer Siegal-Gaskins, Tracy Slatyer, Francesca Valsecchi, Vincenzo Vitale, Christoph Weniger, Farhad Yusef-Zadeh, and Andreas Zezas. I would like to thank my graduate student compatriots for their help and support over the last five years - especially my office mates Laura Fava, Chris Moody, Lauren Porter, and Max Wainwright for always making the office an enjoyable place to work.

I would also like to thank Dan Hooper and Stefano Profumo for acting as my advisors over the last 5 years. The results presented here are largely due to their insights, optimism, encouragement, and energy. Over the course of these collaborative projects, I have learned an important lesson about the passion necessary to contribute novel ideas to this field. I am also grateful to my undergraduate advisor, Vicky Kalogera, for her continued support through my graduate years – as well as for her work and understanding in aiding my scientific progression from a careless, bumbling undergraduate into a graduate student capable of meaningful scientific research.

Most importantly, I would like to thank my family for their unwavering support over the last five years. I would like to thank my parents Ted and Kelly, and my siblings Andy and Caroline for cultivating my interest in math and science from a young age, for keeping me focused through stressful adolescent years, and for providing support in instances

to countless to remember, much less mention. Finally, and most importantly, I would like to give my sincere thanks to my wife, Colleen, for her unwavering support during the last five years. She has always been with me, through hectic travel schedules, long-distance separations, and stressful exams, and without her constant support this would never have been possible.

Reprinting of Previously Published Material

Chapter 1

Introduction

1.1 Gravitational Signatures of Dark Matter

Dark Matter is all around us – literally. The most recent measurements by the Planck Collaboration indicate that the total energy density of our universe is composed of only 4.6% baryonic matter (Planck Collaboration et al., 2013). This number includes all the stars, gas, dust, and radiation that we have ever observed. The other 95.4% of the universe is "dark", meaning it does not interact with photons with a typical electromagnetic cross-section. A significant percentage of this energy density (26.8% of the total) exists in the form of "dark matter", while the rest is composed of "dark energy". While dark energy is homogeneous throughout the entire universe, dark matter settles into clumps which then form the dominant gravitational energy source of all galaxies.

If dark matter does not interact with light, then how was it first discovered, and how can it be detected today? The large energy density of dark matter allows it to have a significant impact on the structure of the universe on large scales, where gravity acts as

a dominant force. The effect of dark matter was first discovered by Fritz Zwicky in 1933. Zwicky had analyzed the Coma Cluster, a nearby galaxy cluster hosting over 1,000 galaxies, and found that that the orbital velocity of each galaxy around the center of the cluster was far greater than would be inferred from the total luminous mass of the cluster. If only the luminous mass were holding the cluster together, it would simply fly apart! Zwicky concluded that a large amount of "dunkle Materie" (dark matter) must be present in order to hold the cluster together (Zwicky, 1933).

Several years later, Babcock (1939) observed that the rotation velocity of stars in the outer region of M31 was unexpectedly high, and noted the possibility that missing mass would be needed to account for these observations. At the same time, Jan Oort studied the galaxies NGC 3115 and NGC 4494 and found the mass distribution to be almost unrelated to the luminosity distribution (Oort, 1940). In 1959, Kahn & Woltjer (1959) calculated amount of mass needed to bind the local group of galaxies (including the Milky Way and M31) into a stable cluster, and found that the mass must be at least six times the luminous mass of the local group. They posited that a large component of intergalactic mass must be necessary in order to stabilize the orbits of local group galaxies.

However, advancements in this field progressed slowly for several decades, due to the lack of a smoking-gun signal indicating the need for a new (and dominant) source of gravitational forces in the universe. This changed in 1970 when Vera Rubin produced rotation curves of stars in the Andromeda galaxy, indicating that the rotational velocity of stars at large distances from the center of the galaxy were nearly constant, instead of falling off as $r^{-1/2}$ as would be expected if the luminous matter near the galactic center accounted

for the entire mass density of the galaxy (Rubin & Ford, 1970). This measurement, of vastly higher quality than previous work, set the stage for serious investigations into the source of this missing mass. Roberts & Whitehurst extended this measurement to the very outer reaches of M31, where they found the mass-to-light ratio to be approximately 200 times larger than the typical value found in the Milky Way (Roberts & Whitehurst, 1975). Meanwhile, Ostriker & Peebles (1973) found that a large spherically symmetric mass must be present in galaxies to explain the stability of the galactic disk. Interestingly, van den Bergh (1999) notes that this "second revolution" in searches for dark matter did not refer to the earlier works by Zwicky and Oort – as they did not tie in this missing galactic mass with the forces which controlled the motion of galaxy clusters.

If the anomalous rotation measurements identified by Zwicky, Oort, Babcock, Rubin, and others indeed stems from a new "dark" addition to the stress-energy tensor of the universe, then some new, and possibly detectable object must be responsible for this missing mass. Some early efforts concentrated on dim, but massive, objects such as solar mass black holes, or red dwarf stars which would be difficult to observe (see e.g. Roberts & Whitehurst (1975)). However these were also excluded, as the large number density of black holes in the galaxy would greatly increase the probability of that more distant stars could be observed with light which passes near the black hole, brightening in the process (Paczynski, 1986). This would create micro-lensing of visible stars, a process which has not been observed commonly enough to explain the dark matter densities with these massive objects (Tisserand et al., 2007; Graff & Freese, 1996)

Other efforts focused on weakly-interacting particles such as the neutrino, as ev-

idence was emerging that the neutrino may have a non-zero rest mass (Kuchowicz, 1969). Cowsik & McClelland (1973) noted that if the neutrino had a rest mass of only a few eV/c^2, this might be sufficient to explain the entire dark matter mass observed in galaxy and galaxy cluster observations. A consequence of this is that the dark matter would be "hot", that is, it would have a relativistic mass far in excess of its rest mass (Doroshkevich et al., 1981). However, White et al. (1983), utilizing their recent work on the evolution of cosmic structure (Frenk et al., 1983), found that the scales on which hot-dark matter, such as neutrinos, collapse to form gravitational potentials hosting galaxies does not match the large coherence length found in observations of the formation of structure in our universe. Notably, this was the first argument (of which the author is aware) which employed observations about the cosmology of our universe, and used it in order to place constraints on the unknown nature of a fundamental particle in our universe.

It was then posited that a particle heavier than the neutrino could exist, which would make the dark matter warm (Blumenthal et al., 1982) or even cold (Blumenthal et al., 1984), solving the structure formation problems indicated by White et al. (1983). A number of papers posited that a cold dark matter (hereafter CDM) particle was capable of explaining the missing mass of these galaxies, and simultaneously produced very good fits to current observations of cosmic structure (Bond & Szalay, 1983; Blumenthal et al., 1984). Two convincing candidates were put forth, including the lightest supersymmetric particle, which could be made stable through a conserved R-parity (Goldberg, 1983; Pagels & Primack, 1982), as well as axions which had been previously posited in order to explain the strong CP problem (Preskill et al., 1983; Dine & Fischler, 1983)

It is also worth noting that the addition of a new dark matter component was initially only one solution which solved the anomalous rotation curves observed in both galactic and extragalactic systems. Another possible solution was that gravity is a stronger force at large distances than predicted by General Relativity. In terms of Einstein's field equations:

$$R_{\mu\nu} - \frac{1}{2}g_{\mu\nu}R + g_{\mu\nu}\Lambda = \frac{8\pi G}{c^4}T_{\mu\nu} \tag{1.1}$$

either the stress-energy tensor ($T_{\mu\nu}$ describing the energy density which produces a curvature of space time) or the metric tensor ($g_{\mu\nu}$), describing how much space time distorts due to the existence of a given energy density) could be modified in order to create faster rotation from a given amount of luminous matter. The prior change corresponds to the addition of a new dark matter component to the energy density of the universe, while the latter component could describe a modification in the gravitational field responds to the existence of a given energy density in the universe.

As an alternative to the dark matter hypothesis, several group of theories, collectively known as MONDs (Modification of Newtonian Dynamics) Milgrom (1983), have proposed that the gravitational force may be modified for extremely small modifications. As a consequence, the flat stellar rotation rate at large differences from the galactic center may be explained by the flattening of the relationship between the acceleration and the gravitational potential from the many sources very far from the outer halo of each galaxy.

While theoretical prejudice, along with the potential of dark matter to explain the growth of cosmic structure, motivated most people to pursue a new dark matter particle,

there was, for some time, no smoking-gun which ruled out a MOND hypothesis. However, in 2006 observations of the "Bullet Cluster" provided evidence for the interpretation of dark matter as a new particle in nature (Clowe et al., 2006; Bradač et al., 2006). Specifically, astronomers found evidence for two galaxy clusters which had recently collided with a relative velocity that was nearly perpendicular to our line of sight. During the collision the collisional gases in each galaxy cluster interacted inelastically, while the dark matter particles pass through without interacting. This leads to a spatial displacement between the dark matter (and the center of the cluster gravitational potential) and the position of hot gas, which is at odds with modifications to the strength of the gravitational force. While some proponents of MOND have produced methods for overcoming this observation, recent years have seen a growing belief in the CDM hypothesis. For the remainder of this thesis, we will work within this framework, where the lightest supersymmetric particle is the dominant component of our universes dark matter.

1.2   Particle Properties of Dark Matter

Any particle CDM candidate must have three critical properties: (1) it must be electromagnetically neutral, (2) it must be stable (on the order of a Hubble time), (3) it must be cold, which means it must have a large rest mass compared to its kinetic energy. The first property rules out many known stable particles (e.g. proton, electron), the second property rules out massive neutral particles like the neutron, while the third rules out a neutrino, or other extremely light particle.

An obvious candidate which fulfills the three criteria above is the lightest super-

symmetric particle. While the properties of the supersymmetric particles are unknown, a particle fulfilling all three above the above properties is theoretically motivated. In order for all supersymmetric particles to have escaped observation, the most reasonable assumption is that they have couplings which have so far escaped the detection of colliders such as the Tevatron and LHC. This is not unreasonable, since a neutral, stable dark matter particle will not itself show up in collider detectors, and instead must be observed as a signal of missing energy, a notoriously difficult measurement. Moreover, because supersymmetric models don't generically respect experimentally verified conservation laws (like conservation of lepton and baryon number) a new symmetry is required to forbid couplings that would violate these numbers. This "R-parity" naturally implies that the lightest supersymmetric particle would be stable, as it could not decay to any combination of lighter particles while conserving supersymmetric particle number. These qualities fulfill the second and third criterion for a dark matter particle. It must, at this point, be assumed that the lightest supersymmetric particle is electromagnetically neutral, although this is the outcome of many supersymmetric models.

Interestingly, it was first pointed out by Lee & Weinberg (1977) and Steigman (1979a) that if the new particle (not yet at this point a supersymmetric particle) was a Majorana particle with a weak interaction cross-section and a mass on the weak scale, then the particle would interact with standard model particles in the early universe. In this period, the dark matter particle would obtain an equilibrium density with the various species of standard model particles. When the temperature of the thermal bath in the early universe dropped below approximately 1/20 of the particle mass, the number of dark

matter particles would lock in at the equilibrium rate. Amazingly, this current density of WIMP particles was almost equivalent to the observed energy density of dark matter in our universe! This discovery, termed as the "WIMP miracle" (Weakly Interacting Massive Particle) Steigman (1979a) explained, for the first time, why the energy densities of dark matter and baryonic matter are relatively equivalent (instead of one dominating the total energy budget of the universe by orders of magnitude. The specified velocity averaged cross-section when the particle freezes out of thermal equilibrium has a canonical value $<\sigma v> = 3 \times 10^{-26}$ cm^3 s^{-1}.

A natural consequence of this scenario is that some residual interactions between WIMP particles should persist today, albeit at a significantly smaller rate. By considering a mock Feynman diagram, shown in Figure 1.1, where two Majorana WIMP particles interact with two standard model particles, we can rotate the diagram to explain all three variations of current WIMP interactions. First, two high energy standard model particles could collide (in an experiment such as the Tevatron or LHC) producing two dark matter particles. Since dark matter particles are stable and don't interact electromagnetically (criterion 1 and 2), this would be seen as a signature of missing energy in particle physics experiments. Secondly, a dark matter particle could pass by a standard model particle and scatter through weak-scale interactions. This elastic scattering event would deposit kinetic energy into the nucleus of the standard model particle, an effect which can be observed in low-background experiments where cold standard model particles are kept isolated from any other energetic baryons or leptons. Lastly, two dark matter particles could collide and annihilate into standard model particles. It is this final process we will concern ourselves

with in the remainder of this thesis.

1.3   The Indirect Detection of Particle Dark Matter

If dark matter annihilates into standard model particles, Earth based observatories could potentially detect their flux. Since no single standard model particle can have a definite dark matter or astrophysical origin, the determination of a dark matter signal must be made on a statistical basis, using either the morphology and spectrum of incoming particles in order to determine the dark matter or astrophysical origin. Telescopes can search for either charged particle anti-particle pairs, such as electron/positron or proton/anti-proton pairs, or can search for neutral particles such as photons and neutrinos. Charged particles searches have two advantages. First, most models of dark matter annihilation distribute significantly more energy into charged particle pairs than into secondary γ-rays and neutrinos. Secondly, anti-particles are often produced in relatively small quantities by astrophysical processes, while Majorana dark matter models generically produce equivalent amounts of matter and anti-matter - creating a clear signature of dark matter annihilation. However, charged particles unfortunately isotropize quickly while moving through the random magnetic fields of the galaxy. Thus, charged particle detection yields no information about the morphology of dark matter annihilations.

While neutrinos and photons occur farther down the decay chain of dark matter annihilations and thus represent a smaller fraction of the total energy yield of each annihilation, high energy photons and neutrinos which are produced promptly in these decay chains then travel to the solar position relatively undisturbed. Thus, the observation of a

9

γ-ray photon from a dark matter annihilation event would yield information about where that annihilation occurred in the sky. This information is extremely useful, as N-body simulations and observations of astrophysical rotation curves give us detailed information about where dark matter is clustered in the sky. The ability to compare that information with observations is critical in separating any dark matter flux from astrophysical backgrounds. It is worth noting that this can become much more complicated for lower energy photons or neutrinos which are produced via energy loss mechanisms from stable charged particles propagating through the interstellar medium (e.g. via synchrotron, bremsstrahlung, or inverse-Compton scattering). These processes may still provide morphological information of the dark matter density profile, but this information must be carefully extracted from the complexities of cosmic-ray propagation.

In order to search for evidence of dark matter annihilation into photons, we must look in regions of the sky where the dark matter density is high. Due to its relative proximity and high dark matter density, the Galactic center (GC) of the Milky Way is an optimal location for these searches. Notably, simulations of dark matter structure formation almost universally predict the center of the Milky Way galaxy to provide the most luminous source of annihilating dark matter.

It is worth noting two concerns which immediately arise in searches for dark matter annihilation at the GC. First, despite the very large density of dark matter (compared to our solar neighborhood), the density of baryonic matter rises ever faster near the galactic center, meaning that dark matter is a subdominant component of the mass density in the inner region of the galaxy. Thus, gravitational models (i.e. of stellar rotation near the

galactic center) are unable to constrain the density of dark matter in this region. We must rely on simulations of the dark matter density in order to determine the dark matter density throughout the GC. This adds significant uncertainty into our calculations.

This uncertainty is compounded by the fact that the large baryon density can affect the calculated dark matter profile, a feature which was not implemented in early "dark matter only" simulations of the dark matter density profile. The addition of baryons can affect the dark matter profile in one of two ways: baryons (unlike dark matter) can interact electromagnetically and fall (condensate) into the GC. This change in the gravitational potential can cause dark matter to infall as well, increasing the dark matter density very near the GC, in a process known as adiabatic contraction (Gnedin et al., 2004a).

Alternatively, it has been argued that stellar feedback (e.g. from supernovae explosions or starburst driven outflows) can effectively smooth out the dark matter profile on kpc scales, creating a dark matter "core" of nearly constant dark matter density in the inner regions of the galaxy (Governato et al., 2010; Oh et al., 2011). This mechanism has been modeled primarily in the context of dwarf galaxies, where it has been used in order to help remedy the missing satellites problem as well as the too-big-to-fail problem (Walker & Peñarrubia, 2011; Peñarrubia et al., 2012). Both of these challenges to the ΛCDM paradigm examine the mismatch between the expected number and size of observed Milky Way dwarf galaxies, compared to simulations. Typically simulations predict more massive satellites than are observed. In these cases, the predicted mass of the dwarf spheroidal galaxies found in simulations would decrease, if baryonic effects caused the central density of the dwarf halos to decrease compared to the predictions from dark matter only simulations.

Applying models of supernova feedback to the GC, we find that the high supernova rate in this region (Crocker & Aharonian, 2011) implies that the dark matter density profile in the GC may also be cored. The final effect of the uncertain combination of adiabatic contraction and supernova driven outflows is a large uncertainty in the profile of the inner galaxy. Depending on the region of interest for different observations, this can lead to order of magnitude differences in the expected dark matter annihilation rate. These errors must be considered carefully, especially when setting limits on the expected dark matter annihilation cross-section, and comparing them between experiments.

1.4 Astrophysical Backgrounds

A second problem in searches for dark matter annihilation in the GC concerns the dense astrophysical background[1] In addition to being the brightest projected source for particle dark matter annihilation, the GC also hosts diverse high energy sources such as supernova remnants (Yusef-Zadeh et al., 1999), highly ionized gas (Wang et al., 2002), dense molecular clouds (Ferriere, 2012), massive O/B stars (Schödel et al., 2009) and both young and recycled pulsar populations (Wharton et al., 2012).

Since many of these populations produce copious γ-ray emission, spectral or morphological models of each emission class must be employed in order to subtract astrophysical components and uncover any underlying emission from dark matter. Since this is extremely difficult (due to large uncertainties in models of astrophysical emission), the most promising avenues often involve searches in regimes where the expected dark matter annihilation rate

---

[1]Of course, what is a annoying background in searches for dark matter annihilation may be a fascinating signal for other astronomers!

forms a relatively large percentage of the total emission. One of the most promising energy regimes is in γ-ray observations; assuming a standard model for WIMP dark matter (100 GeV particle annihilating to bottom quarks with a thermal cross-section and following an NFW density profile), dark matter is expected to produce $\sim$20% of the total γ-ray flux between 1-3 GeV. Thus, simple astrophysical models (with significant uncertainty) may still place interesting limits on the dark matter annihilation rate.

1.5 Telescopes and Relevant Search Techniques

The indirect detection of particle dark matter depends on observations across the electromagnetic spectrum. Since the flux of photon changes by many orders of magnitude between radio and γ-ray energies and the interactions between incoming photons and materials changes drastically as a function of photon energy, different techniques are necessary in order to measure astrophysical emission in different energy regimes.

For the highest energy γ-rays, Atmospheric Cherenkov Telescopes (ACTs), such as the High Energy Spectroscopic System (H.E.S.S.) and the Very Energetic Radiation Imaging Telescope Array System (VERITAS) have been at the forefront in γ-ray observations of the galactic center. These telescopes observe the sky by examining the Cherenkov radiation produced when high energy γ-rays pair produce through interactions with virtual photons from atoms high in the galactic atmosphere, creating highly energetic charged showers which propagate through the atmosphere Hinton (2004). Unfortunately, due to the necessity for incident γ-rays to make bright Cherenkov radiation from energetic showers in the upper atmosphere, the sensitivity of ACT telescopes degrades quickly below energies of approxi-

mately 100 GeV, making them insensitive to dark matter annihilation from relatively light particles.

Since the H.E.S.S. telescope is located in the southern hemisphere, it is in an optimal position for long-duration observations of the GC region. These observations have placed strong constraints on the annihilation cross-section of relatively high-mass (TeV scale) dark matter models (Aharonian et al., 2006f; Abramowski et al., 2011; Aharonian et al., 2006e). While these searches have not, thus far, ruled out the canonical thermal annihilation cross-section for heavy dark matter particles, the parameter space of models with enhanced annihilation cross-sections has been significantly eroded. This has been a critical development, as these observations have ruled out models of dark matter annihilation which have been proposed to fit a recently observed excess of high energy cosmic-rays at the solar position (Adriani et al., 2009a; Abazajian & Harding, 2012).

The Fermi Large Area Telescope (Fermi-LAT) is a pair-conversion, space-based γ-ray telescope, with an effective energy range from approximately 100 MeV to 300 GeV Atwood et al. (2009). Compared with previous missions such as EGRET Thompson et al. (1993), the Fermi-LAT has a vastly superior effective area (~ 1 m^2), energy resolution ($\sim 10\%$) and angular resolution ($\sim 1°$ at 1 GeV, and $\sim 0.1°$ above 10 GeV). Since the Fermi-LAT is based in space, it can detect significantly lower-energy γ-rays than ACTs, allowing the telescope to probe the vast majority of the theoretically motivated WIMP mass range.

Additionally, radio telescopes have an important role in searches for dark matter annihilation. Efforts to employ radio telescopes in searches for dark matter benefit from

the vastly superior angular resolution of radio instruments (e.g. VLA, 0.1") compared to γ-ray observatories. These give low energy missions a greatly superior ability to distinguish diffuse emission from dark matter annihilation from point-source (or diffuse) astrophysical backgrounds. However, as noted above, the majority of the radio signal from dark matter annihilation proceeds from the synchrotron radiation of energetic electrons produced in dark matter searches. This means that the source of the synchrotron signal does not correlate directly with the site of the dark matter annihilation. Many searches attempt to simplify this assumption by evaluating regions where the synchrotron radiation from energetic electrons should be produced relatively quickly, validating the assumption that the dark matter density should serve as a reasonable template for the synchrotron morphology. Additionally, radio telescopes can focus on using their superior angular resolution to place limits on astrophysical emission mechanisms, such as pulsars which may greatly contribute to the astrophysical γ-ray background.

1.6 Outline

In the remainder of this dissertation, I will focus on several previously published efforts to compare our models of the dark matter induced photon flux from the GC with observations. Focusing primarily on γ-ray observations, in Chapter 2, I will describe an interesting observation of an excess in spherically symmetric, diffuse γ-ray emission from the region surrounding the GC. This signal has an energy spectrum and morphology well-modeled by light dark matter models, and is difficult to accurately produce with any known astrophysical process. In Chapters 3 and 4 I will discuss models for the production of γ-rays

from the black hole at the center of our galaxy. We find that while protons produced by the central source provide an excellent observation for the spectrum and morphology of the point-source observed in the GC, they are unable to reproduce the extended excess observed in Chapter 2. In Chapter 5, I will discuss a radio study of the dark matter annihilation in the filamentary arcs near the galactic center. We find that dark matter annihilating within these filaments explains the spectral signature observed in numerous radio filaments, and additionally explains the luminosity distribution of the class of filaments as a function of their galactic radius. Finally, in Chapter 6, I will note recent follow-up studies by validating some of the conclusions in this work, and will look towards future studies which could further elucidate the nature (dark matter or not) of photon emission from the GC region.
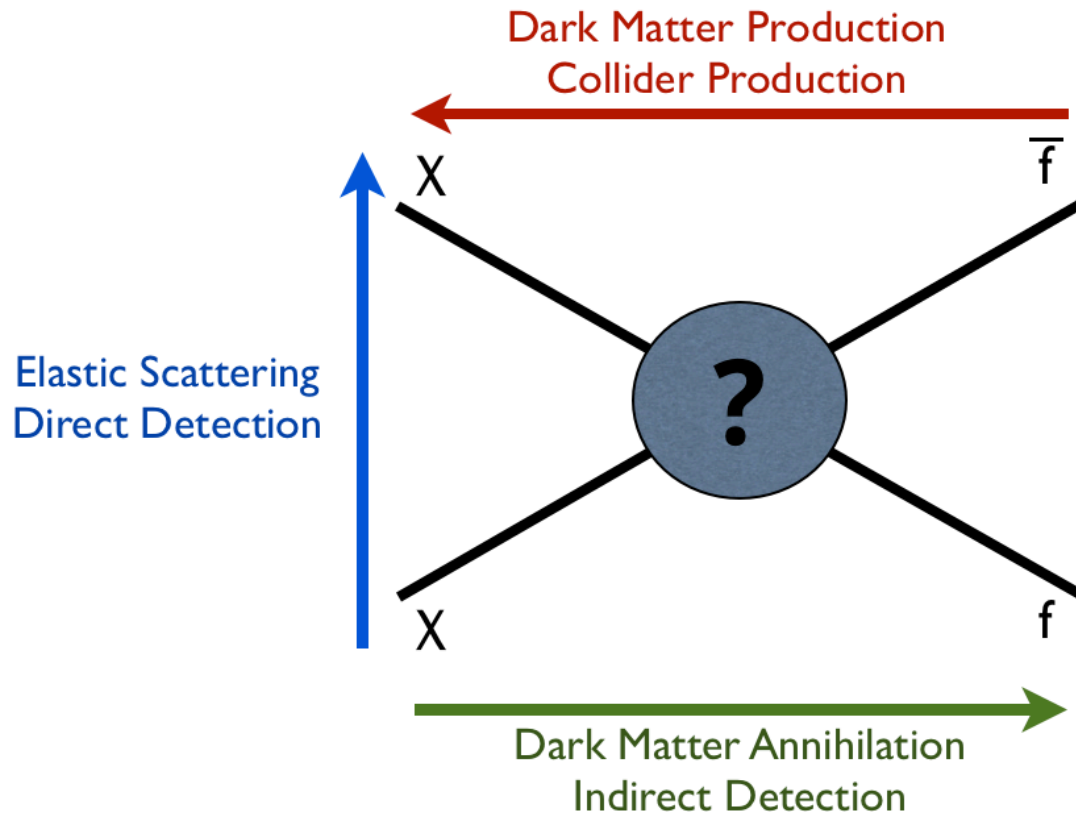
Figure 1.1 A Feynman Diagram depicting the three methods for the detection of dark matter. Reading the diagram with time moving from the left to the right shows the annihilation of two dark matter particles (through some, currently unknown, interaction) into standard model particles. Reading the diagram with time moving from the right to the left shows the collider production of dark matter from the interaction of two energetic standard model particles (e.g. quark interactions from the LHC or Tevatron). Finally, reading the diagram with time moving from the bottom to the top shows the elastic scattering of a dark matter particle off of a standard model particle, which is detectable by direct detection experiments.

Chapter 2

On the Origin of Gamma Rays from the Galactic Center

Since its launch in June of 2008, the Fermi Gamma-Ray Space Telescope (FGST) has been producing the most detailed and highest resolution observations to date of the gamma-ray sky between 50 MeV and 100 GeV. Among the objectives of this experiment are to increase our understanding of how astrophysical objects such as black holes and pulsars accelerate cosmic rays, and to help identify the substance or substances that compose the dark matter of our universe. For each of these areas of inquiry, the region surrounding the center of the Milky Way represents a particularly interesting and promising target of study. On the one hand, the Galactic Center is an extraordinarily rich and complex region, containing our galaxy's supermassive black hole, as well as supernova remnants, massive X-ray binary systems, massive O and B type stars, and two young and massive star clusters (Arches and Quintuplet) Wang et al. (2002); Yusef-Zadeh et al. (2000); LaRosa

et al. (2000a); Hooper et al. (2004a).

In this chapter, we follow previous work Hooper & Goodenough (2011a) and perform a detailed study of the spectral and morphological features of the gamma rays from the Galactic Center region, with the intention of identifying or constraining the origins of these particles. In particular, we produce gamma-ray maps which reveal the presence of both a bright, approximately point-like, gamma-ray source at the Galactic Center, along with a more spatially extended emission component. The spectrum of this extended source peaks strongly between several hundred MeV and ∼10 GeV. We find good agreement between our results and those reported by other groups Hooper & Goodenough (2011a); Boyarsky et al. (2011); Chernyakova et al. (2011).

In discussing the possible origins of this extended emission, we find again that the observed spectrum and morphology are consistent with that predicted from annihilating dark matter particles with a mass of 7-12 GeV annihilating dominantly to leptons Hooper & Goodenough (2011a) or a mass of 25-45 GeV annihilating dominantly to hadronic final states Goodenough & Hooper (2009). In either case, the normalization of the gamma-ray flux requires an annihilation cross section that is consistent, within astrophysical uncertainties, with the value predicted for a simple thermal relic ($\sigma v \sim 3 \times 10^{-26}$ cm^3/s). We also discuss the possibility that the extended gamma-ray emission is produced through the collisions of energetic protons which are accelerated by the supermassive black hole with gas Chernyakova et al. (2011). While we consider this to be the leading astrophysical explanation for the gamma-ray emission observed by the FGST, it is somewhat difficult to assess this hypothesis given how little is known or can be reliably predicted about the spectrum

or flux of protons accelerated by the central black hole, and how little is known about the history of this object (such as periods of flaring and relative inactivity) and the properties of the surrounding interstellar medium.

The remainder of this article is structured as follows. In Sec. 2.1, we describe our analysis of the Fermi data and present gamma-ray maps of the Inner Galaxy and the corresponding spectrum of this emission. In Sec. 2.2 we further describe the properties of this emission and compare our results to those found by other groups. In Sec. 2.3 we discuss several possible origins of this emission, including energetic protons from the central supermassive black hole, dark matter annihilations, and a population of gamma-ray pulsars. In Sec. 2.4, we derive constraints on the dark matter annihilation cross section which are at least as stringent as those based on other observations, such as those of dwarf spheroidals, galaxy clusters, the cosmological diffuse background, and nearby subhalos. In Sec. 2.5, we discuss our results within the larger context of dark matter searches and summarize our conclusions.

2.1   Analysis Procedure

We begin our analysis by generating contour maps of the region surrounding the Galactic Center which describe the distribution of gamma rays observed by the Fermi-LAT (Large Area Telescope) over the three years between August 4, 2008 and August 3, 2011. These maps were derived using only front-converting events (which have a superior point-spread function compared to back-converting events) from the Pass 7 ultraclean class. As recommended by the FGST collaboration, we include only events with zenith angles

smaller than 100 degrees, and do not include events recorded while the Fermi satellite was transitioning through the South Atlantic Anomaly or while the instrument was not in survey mode (e.g. during target of opportunity observations of flaring sources). Each of the maps has been smoothed out at a scale of 0.5 degrees (the contour maps thus represent the flux observed within a 0.5 degree radius of a given direction in the sky). These raw maps are shown in the left frames of Fig. 2.1, for five different energy ranges between 100 MeV and 100 GeV.

In each map, ten contours are shown, distributed linearly between 2.64×10^{-8} and $2.64 \times 10^{-7} \mathrm{cm}^{-2} \mathrm{s}^{-1}$ sq deg^{-1} (100-300 MeV), 2.45×10^{-8} and $2.45 \times 10^{-7} \mathrm{cm}^{-2} \mathrm{s}^{-1}$ sq deg^{-1} (300-1000 MeV), 1.07×10^{-8} and $1.07 \times 10^{-7} \mathrm{cm}^{-2} \mathrm{s}^{-1}$ sq deg^{-1} (1-3 GeV), 2.66×10^{-9} and $2.66 \times 10^{-8} \mathrm{cm}^{-2} \mathrm{s}^{-1}$ sq deg^{-1} (3-10 GeV), and 3.77×10^{-10} and $3.77 \times 10^{-9} \mathrm{cm}^{-2} \mathrm{s}^{-1}$ sq deg^{-1} (10-100 GeV). Note that the $2.64 \times 10^{-8} \mathrm{cm}^{-2} \mathrm{s}^{-1}$ sq deg^{-1} contour appears out of the field in the upper-left and upper-middle frames.

The blue points shown in the maps represent the locations of sources contained in the Fermi Second Source Catalog (2FGL) Nolan et al. (2012), and the size of each point is proportional to the reported intensity of the source in the energy range shown. To account for these sources, we have generated a template map of their emission (assuming the central values for their intensity and locations as reported in the 2FGL), and taking into account the point-spread function of the Fermi-LAT (as determined by the Fermi Tool gtpsf). In the center frames of Fig. 2.1, we show the maps as they appear after subtracting this source template. Note that we have not removed the central bright source, as its emission is difficult to disentangle from dark matter annihilation products originating from the inner

region of a cusped halo profile. We will return to this issue later in the article.

After subtracting these known sources, the dominant remaining component is the diffuse emission associated with the disk of our galaxy. This emission is dominated by cosmic ray processes taking place throughout the disk of the Milky Way, which one must look through in order to observe the Galactic Center. By studying the morphology of this emission over the regions of $5° < |l| < 10°$, we find only a modest degree of variation with galactic longitude. In Fig. 2.2, we show as solid lines the observed gamma-ray flux as a function of galactic latitude, averaged over the range of $7° < |l| < 10°$ (in order to avoid any contamination with emission from the inner most degrees, we do not here make use of the data within $7°$).

The gamma-ray emission from the disk of our galaxy is dominated by the decays of neutral pions produced in cosmic ray interactions with gas, although inverse compton and bremsstrahlung components also contribute. To model the morphology of the pion decay component, we adopt the following distribution of gas Kalberla & Kerp (2009); Nakanishi & Sofue (2003):

$$\rho_{\text{gas}} \quad \propto \quad e^{-|z|/z_{\text{sc}}(R)}, \qquad\qquad R < 7\,\text{kpc}, \qquad\qquad (2.1)$$

$$\rho_{\text{gas}} \quad \propto \quad e^{-|z|/z_{\text{sc}}(R)}\, e^{-R/R_{\text{sc}}}, \quad R > 7\,\text{kpc},$$

where z and R describe the location relative to the Galactic Center in cylindrical coordinates. We set $R_{\text{sc}} = 3.15$ kpc (as fit to the data shown in Fig. 4 of Ref. Kalberla & Kerp (2009)) and $z_{\text{sc}}(R) = 0.1 + 0.00208 \times (R/\text{kpc})^2$ kpc (as fit to Fig. 4 of Ref. Nakanishi & Sofue (2003)), in good agreement with observations of 21-cm surveys, which trace the density of neutral hydrogen. To estimate the flux of pion decay gamma rays, we integrate this

22

distribution over the line-of-sight (and again smooth over a radius of 0.5 degrees). After accounting for the Fermi-LAT point-spread function, we find that this gas distribution leads to the morphology described by the dashed lines in Fig. 2.2. This is in good agreement with the observed morphology of the diffuse emission. We also note that the spectral shape implied by the relative fluxes in these five energy bins is consistent with that predicted for a combination of pion decay and inverse compton scattering processes, as previously found in Ref. Hooper & Goodenough (2011a). By subtracting this disk template from the gamma-ray maps, we are able to remove the overwhelming majority of the diffuse astrophysical background from our maps. We emphasize that in performing this subtraction, we are not extrapolating any physical features of the inner galaxy, but are merely extrapolating the line-of-sight gas densities along the disk from directions slightly away from the Galactic Center to those more aligned with the Galactice Center.

In the right frames of Fig. 2.1, we show the resulting maps after subtracting both the known sources template (again, not including the bright central source) and the line-of-sight gas template. In each energy range, the majority of the background has been accurately removed by this simple subtraction. While this subtraction procedure does not perfectly remove all likely astrophysical backgrounds, the residuals outside of the inner $\sim 2°$ are very modest, typically on order of 10% or less of the residual flux in the innermost region of the Galaxy. We include the observed spatial variations of the residuals as a systematic error, which we propagate throughout this study.

The residuals in this innermost region include a roughly spherically symmetric component centered around the Galactic Center, along with a sub-dominant component

that is somewhat extended along the disk. Due to its similar angular extent, we consider it likely that this component is associated with emission from proton-proton collisions taking place in the Galactic Ridge, as observed at higher energies by HESS Aharonian et al. (2006a). The remaining spherically symmetric component could plausibly originate from dark matter annihilations, processes associated with the Milky Way's supermassive black hole, gamma-ray pulsars, or a combination of these and other sources. We will return to these issues in Secs. 2.2 and 2.3.

In Fig. 2.3, we show the spectrum of the emission from the inner 5 degrees surrounding the Galactic Center, after removing the known sources and disk emission templates. The spectrum is clearly brightest between 300 MeV and 10 GeV, and drops by nearly an order of magnitude above ∼10 GeV. Note that the spectral shape of this residual is very similar to that (preliminarily) reported in conference presentations by the Fermi Collaboration Vitale et al. (2009a). In the following sections, we will explore the characteristics of this residual emission and discuss its possible origins.

2.2 Properties of the Inner Emission

In an effort to constrain the origin (or origins) of the gamma rays from the inner region of our galaxy, we discuss in this section the spectral and morphological characteristics of the observed emission Dodelson et al. (2008); Zaharijas & Hooper (2006); Hooper & Dingus (2004). We begin by noting that the morphology of the observed residual is not consistent with that of a single point source. In particular, we find that above 300 MeV, less than half of the residual emission shown in the right frames of Fig. 2.1 can be accounted for

by a single, centrally-located point source. This conclusion is also supported by the independent analyses by Boyarsky *et al.* Boyarsky et al. (2011), Chernyakova *et al.* Chernyakova et al. (2011), and Hooper and Goodenough Hooper & Goodenough (2011a), which each found a spectrum of point-like emission from the Galactic Center which is considerably less intense than the total residual emission shown in Fig. 2.3. In Fig. 2.4, we show the spectra of point-like emission from the Galactic Center, as reported in each of these three prior studies. We note that the intensity and spectral features of the Galactic Center point source found by these three groups are very similar, despite the very different analysis techniques employed.

In Fig. 2.5, we compare this spectrum of point-like emission (as reported by Boyarsky *et al.* Boyarsky et al. (2011)) to the spectrum of residual emission found in our analysis.[1] Between 100-300 MeV, there is good agreement, indicating that most or even all of the residual gamma rays in this energy range could originate from a single point source. At higher energies, however, the residual emission consistently exceeds the flux attributable to point-like emission; by a factor of $\sim$2-3 between 0.3 and 3 GeV, and by a factor of $\sim$5 above 3 GeV. When Boyarsky *et al.* included a spatially extended component in their model (with a morphology corresponding to that predicted for annihilating dark matter with a distribution given by $\rho_{\rm DM} \propto r^{-1.34}$), they found that the fit improved considerably (reducing the log-likelihood by 25 with the addition of only one new parameter) Boyarsky et al. (2011). The spectrum of this spatially extended component is also shown in Fig. 2.5. The spectrum of the residual emission found in our analysis is in very good agreement with

---

[1]HESS Aharonian et al. (2004a); Braun et al. (2008); Aharonian et al. (2006b) and other ground based telescopes Kosack et al. (2004); Albert et al. (2006) have also observed point-like emission from the Galactic Center at energies above $\sim$200 GeV. This very high energy gamma-ray source may be associated with the point-like emission observed at lower energies, as shown in Fig. 2.4.

the sum of point-like and extended components as reported by Boyarsky *et al.* From these comparisons, we conclude that in addition to the presence of point-like emission from the Galactic Center, a component of extended emission is also prominently present at energies greater than ∼300 MeV.[2]

2.3   Possible Origins of the Observed Emission

A number of proposals have been put forth to explain the bright gamma-ray emission observed from the Galactic Center by the FGST. These possibilities include the central supermassive black hole Chernyakova et al. (2011); Hooper & Goodenough (2011a), a population of unresolved millisecond pulsars Abazajian (2011a), and dark matter annihilations Hooper & Goodenough (2011a); Goodenough & Hooper (2009). In this section, we discuss the morphological and spectral characteristics of the gamma-ray emission expected from each of these potential sources and compare this to the emission observed by the FGST.

2.3.1   Cosmic ray Acceleration by the Supermassive Black Hole

To begin, we reiterate that the morphology of the observed emission is not entirely point-like in nature, but instead is somewhat spatially extended. This allows us to rule out the possibility that gamma rays directly emitted by the Milky Way's central black hole are responsible for the observed emission.[3] If, however, the observed gamma-ray spectrum

---

[2]The spectrum of our residual as presented in Figs. 2.3 and 2.5 denotes the residual within a 5 degree radius around the Galactic Center, whereas the spectrum of extended emission reported in Ref. Boyarsky et al. (2011) is taken from a similar, but not identical, inner $10° \times 10°$ region. Given the highly concentrated nature of the morphology being considered, however, this difference is negligible.

[3]Further supporting this conclusion is the fact that the central emission observed by Fermi shows no variability on month timescales Chernyakova et al. (2011), as would be expected based on the variability

originates from cosmic rays that have been accelerated by the black hole, then a spatially extended distribution of gamma rays could result.

For example, it was previously proposed that the TeV-scale gamma rays observed from the Galactic Center could originate from the inverse Compton scattering of energetic electrons accelerated by the black hole Atoyan & Dermer (2004); Hinton & Aharonian (2007). This scenario, however, predicts considerably less GeV-scale emission than is observed by Fermi, and thus cannot account for the residual emission discussed here Chernyakova et al. (2011). Alternatively, the black hole may accelerate cosmic ray protons which then diffuse throughout the surrounding interstellar medium, producing pions and thus gamma rays through interactions with gas Chernyakova et al. (2011); Aharonian & Neronov (2005a); Aharonian (2005). The spectrum and spatial distribution of the gamma-ray emission resulting from this process depends not only on the spectrum of protons injected from the black hole, but also on the diffusion coefficient and distribution of gas in the surrounding medium, as well as on the emission history of the black hole (occurrences of flares and periods of relative dormancy). As none of these inputs are currently very well constrained, it is difficult to make reliable predictions for the resulting gamma-ray spectrum and distribution. That being said, it appears plausible that a reasonable astrophysical scenario could potentially explain much of the observed emission.

Perhaps the greatest challenge in accounting for the observed emission with energetic protons accelerated by the central black hole is the very rapid increase in the flux of spatially extended emission observed between approximately 200 and 700 MeV (see blue er-

---

of this source in X-ray and infrared wavelengths Ghez et al. (2004); Bélanger et al. (2004); Baganoff et al. (2001). The emission from a $\sim$30 parsec source region would have any variability suppressed on timescales shorter than $R/c \sim 100$ years.

ror bars in Fig. 2.5). Even for a mono-energetic spectrum of protons, the resuling spectrum of gamma rays from pion decay does not rise rapidly enough to account for this feature. Perhaps this could be reconciled, however, if a sizeable fraction of the apparently point-like emission in the 100-300 MeV bin is in fact somewhat extended and arises from cosmic ray interactions.

Lastly, we also note that a sizable fraction of the high energy emission observed by the FGST is likely to be associated with the HESS galactic ridge. This ridge emission, as measured by HESS, possesses a power-law-like spectrum with a spectral index of $2.29 \pm 0.07_{stat} \pm 0.20_{sys}$ over the energy range of approximately 0.2 to 10 TeV. Due to the spatial correlation of this emission with the locations of molecular clouds in the central 200 parsecs of the Milky Way, the origin of the ridge emission is conventionally taken to be the decays of neutral pions produced in the interactions of cosmic ray protons or nuclei with the surrounding molecular gas. In order to generate a gamma-ray spectrum with this spectral index, the responsible protons are required to have a spectral index of approximately 1.9 ± 0.2 Hooper & Goodenough (2011a). Based on an extrapolation of this spectral shape, we estimate that on the order of 30% of the 10-100 GeV residual is associated with the ridge. At energies below $\sim$10 GeV, however, the ridge emission constitutes a much smaller fraction of the observed residual, unless the spectrum of cosmic ray protons in the region is significantly enhanced below $\sim$50 GeV relative to the power-law behavior we have assumed.

2.3.2 Annihilating Dark Matter

It has long been appreciated that if dark matter particles annihilate in pairs (as predicted in most models of weakly interacting massive particles), the resulting gamma-ray

signal would be brightest from the direction of the Galactic Center Bergström et al. (1998); Berezinsky et al. (1994, 1992). The energy and angular dependent flux of such gamma rays is given by

$$\Phi_\gamma(E_\gamma, \psi) = \frac{dN_\gamma}{dE_\gamma} \frac{\sigma v}{8\pi m_{\mathrm{DM}}^2} \int_{\mathrm{los}} \rho^2(r) dl, \tag{2.2}$$

where σv is the dark matter annihilation cross section multiplied by the relative velocity of the two dark matter particles (averaged over the velocity distribution), m_{DM} is the mass of the dark matter particle, ψ is the angle observed relative to the direction of the Galactic Center, $\rho(r)$ is the dark matter density as a function of distance to the Galactic Center, and the integral is performed over the line-of-sight. dN_γ/dE_γ is the gamma-ray spectrum generated per annihilation, which depends on the mass and dominant annihilation channels of the dark matter particle (we use PYTHIA Sjöstrand et al. (2001a) to calculate dN_γ/dE_γ for various dark matter scenarios in this study).

Modern numerical simulations of the evolution of cold dark matter predict the formation of halos with a nearly universal density profile Navarro et al. (2010). Within the inner volumes of such halos, the density of dark matter varies as $\rho_{\mathrm{DM}} \propto r^{-\gamma}$, where r is the distance to the halo's center. The frequently used Navarro Frenk and White (NFW) profile, for example, features an inner slope of $\gamma = 1.0$ Navarro et al. (1996a, 1997). The results of the Via Lactea II simulation favor a somewhat steeper inner slope ($\gamma \approx 1.2$) Diemand et al. (2008a, 2005), while the Aquarius Project finds a somewhat less steep value which varies with r Navarro et al. (2004); Springel et al. (2008).

When considering the dark matter distribution in the central kiloparsecs of the Milky Way, it is important to include the effects of stars and gas, which are not taken

into account by dark matter-only simulations such as Via Lactea II and Aquarius, but which dominate the gravitational potential of the Inner Galaxy. Generally speaking, as a result of dissipating baryons, dark matter density profiles are expected to be adiabatically contracted, resulting in the steepening of their inner profiles Blumenthal et al. (1986a); Ryden & Gunn (1987a). The degree to which this effect is manifest depends on the fraction of the baryons that dissipate slowly by radiative cooling.

As hydrodynamical simulations which model the process of galaxy formation have improved, efforts to predict the effects of baryons have begun to converge. In particular, several groups (using different codes) have consistently found that Milky Way sized halos are adiabatically contracted, increasing the density of dark matter in their inner volumes relative to that predicted by dark matter-only simulations (see Ref. Gnedin et al. (2011a) and references therein). These simulations, which include the effects of gas cooling, star formation, and stellar feedback, predict a degree of adiabatic contraction which steepens the inner slopes of dark matter density profiles from $\gamma \approx 1.0$ to $\gamma \approx 1.2 - 1.5$ within the inner ~ 10 kpc of Milky Way-like galaxies Gnedin et al. (2011a, 2004a). The resolution of such simulations is currently limited to scales larger than ~ 100 parsecs Levine et al. (2008).

With this information in mind, we can compare the expected spatial distribution of dark matter to the observed angular distribution of gamma rays from around the Galactic Center. Making this comparison, we find that the majority of the residual emission observed between 300 MeV and 10 GeV can be described by annihilating dark matter with a distribution given by $\rho(r) \propto r^{\gamma}$, with $\gamma \approx 1.25 - 1.40$.[4] In contrast, an NFW-like profile

---

[4] Below 300 MeV, the observed emission is dominated by point-like emission, and the flux of the emission drops off significantly above 10 GeV, leading us to focus on this energy range.

with $\gamma = 1.0$ would predict a considerably broader distribution of gamma rays than is found in our residual maps. More quantitatively speaking, for $\gamma = 1.0$ we find that for energies of 300-1000 MeV, 1-3 GeV, and 3-10 GeV, respectively, no more than 22%, 18% and 27% of the flux found in the innermost half degree around the Galactic Center can arise from dark matter annihilations without also exceeding the flux observed at distances beyond one degree. In contrast, if we select an inner slope of $\gamma = 1.3$, we find that up to 72%, 74% and 100% of the innermost emission could originate from dark matter annihilations. The remainder of the residual could easily originate from the central point source with the spectrum presented in Fig. 2.4.

If a sizable fraction of the residual emission does originate from annihilating dark matter, then we can use the spectrum of this emission to inform us as to the mass and dominant annihilation channels of the dark matter particles. In particular, the rapid decrease in the flux above $\sim$10 GeV suggests that the spectrum is being dominated by $\sim$30 GeV dark matter particles annihilating to quarks, or by $\sim$10 GeV particles annihilating to leptons (among annihilations to leptons, those to taus produce far more gamma rays than those to either muons or electrons). In Fig. 2.6, we show the range of dark matter masses and annihilation cross sections for which dark matter annihilations can account for the majority of the observed residual emission (without exceeding the observed residual) in each of the three energy bins between 300 MeV and 10 GeV, for three choices of the annihilation channels. Interestingly, we note that the normalization of the signal requires us to consider annihilation cross sections that are within a factor of a few of the value predicted for a simple thermal relic ($\sigma v = 3 \times 10^{-26}$ cm^3/s). The precise value of the required annihilation

31

cross section depends on the quantity of dark matter present, and is thus subject to the related uncertainties. In Fig. 2.6 and throughout the remainder of this paper, we have normalized the dark matter distribution such that the total mass of dark matter within the solar circle is 3.76×10^{67} GeV, which is the value corresponding to the case of $\gamma = 1.0$ and a local density of 0.4 GeV/cm^3. This value is supported by a combination of microlensing and dynamical constraints, although uncertainties exists Iocco et al. (2011); Catena & Ullio (2010a). With these uncertainties in mind, one should consider all annihilation cross sections shown in Fig. 2.6 and elsewhere in this paper to be accurate only to within a factor of a few.

Of course, it is also expected that astrophysical sources will contribute to the Galactic Center's gamma-ray spectrum between 300 MeV and 10 GeV. In Fig. 2.7, we show three examples in which emission from a central point source (as shown in Fig. 2.4), along with emission from the Galactic Ridge (as extrapolated from the higher energy HESS emission, assuming a spectral shape that results from a power-law spectrum of protons) combine with a contribution from dark matter to generate the observed residual emission. Note that the lowest energy emission is largely generated by the central point source (as suggested by the observed morphology) while the highest energy bin is dominated by emission from the Galactic Ridge. Only the 300 MeV-10 GeV range is dominated by dark matter annihilation products.

2.3.3 Millisecond Pulsars

A population of gamma-ray point sources surrounding the Galactic Center could also potentially contribute to the observed residual emission. Millisecond pulsars, which

are observed to produce spectra that fall off rapidly above a few GeV, represent such a possibility[5] Hooper & Goodenough (2011a); Abazajian (2011a).

Observations of resolved millisecond pulsars by FGST have found an average spectrum well described by $dN_\gamma/dE_\gamma \propto E_\gamma^{-1.5} \exp(-E_\gamma/2.8\,\text{GeV})$ Abdo et al. (2009b); Malyshev et al. (2010). Similarly, the 46 gamma-ray pulsars (millisecond and otherwise) in the FGST's first pulsar catalog have a distribution of spectral indices which peaks strongly at $\Gamma = 1.38$, with 44 out of 46 of the observed pulsars possessing (central values of their) spectral indices greater than 1.0 Abdo et al. (2010b) (see Fig. 2.8). In contrast, to produce a sizable fraction of the spatially extended residual emission between 300 MeV and 10 GeV without exceeding the emission observed below 300 MeV, the average pulsar in the Galactic Center population would be required to possess a spectral index harder than $\Gamma \approx 1.0$. And although we agree with the author of Ref. Abazajian (2011a) that a small number of pulsars (including J1958+2846, J2032+4127 and J2043+2740) have been observed with such hard spectral indices, we do not believe that the existing data supports the conclusion that a large population of pulsars (as would be required to generate the observed emission) would produce an average gamma-ray flux with a spectral shape able to account for the observed emission from the Galactic Center.[6] That being said, if the population of pulsars present in the central stellar cluster were to differ significantly from the sample represented by the Fermi pulsar catalog, a different conclusion could potentially be reached.

---

[5]While young, single pulsars are known to have a similar emission spectrum to the MSP population, it is difficult for these sources to explain the morphology of the observed excess. The young pulsar distribution is expected to be similar to the morphology of young, massive stars, which is known to fall off as approximately $r^{-1.4}$ away from the GC. Pulsars may be slightly more dispersed due to the large kick velocities they obtain during their supernova explosions. This is significantly less peaked towards the GC compared to the $r^{-2.6}$ distribution observed for the extended GC excess

[6]The error bars on the spectral indices of these three hardest pulsars are also quite large, $\Gamma = 0.77 \pm 0.31$, 0.68 ± 0.46, and 1.07 ± 0.66 Abdo et al. (2010b).

An opportunity to measure the emission from large populations of gamma-ray pulsars exists in the form of globular clusters, whose gamma-ray emission is generally attributed to pulsars contained within their volumes. Unfortunately, the gamma-ray spectra of these objects have not been well measured. In particular, the eight globular clusters with spectra reported by Fermi have an average spectral index very close to that of pulsars ($\Gamma \approx 1.38$), but with very large individual error bars which extend from roughly 0 to 2.5 (these values, including 1σ statistical and systematic errors are shown in Fig. 2.9). Perhaps with more data, we will learn from these systems whether the spectral indices of large pulsar populations can be hard enough to accommodate the emission observed from the Galactic Center.

Lastly, we note that it is somewhat difficult to accommodate the very spatially concentrated morphology of the observed gamma-ray emission with pulsars. As originally pointed out in Ref. Hooper & Goodenough (2011a), to match the observed angular distribution of this signal, the number density of pulsars would have to fall off with the distance to the Galactic Center at least as rapidly as $r^{-2.5}$. In contrast, within the innermost parsec of the Galactic Center, the stellar density has been observed to fall off only about half as rapidly, $r^{-1.25}$ Schödel et al. (2009). Furthermore, even modest pulsar kicks of ~ 100 km/s would allow a pulsar 10 pc from the Galactic Center to escape the region, consequently broadening the angular width of the signal. Annihilating dark matter, in contrast, produces a flux of gamma rays that scales with its density *squared*, and thus can much more easily account for the high concentration of the observed signal.

34

2.4 Constraints On The Dark Matter Annihilation Cross Section

In this section, instead of attempting to determine the origin of the gamma rays from the Galactic Center region, we use the observed spectrum and flux to place limits on the dark matter annihilation cross section. In doing this, we do not assume anything about the source or sources responsible for the observed emission, but instead only require that dark matter annihilation products do not exceed the observed emission (after subtracting the known sources and line-of-sight gas templates, as described in Sec. 2.1). Despite using this very simple and conservative approach, we derive constraints that are competitive with or stronger than those placed by other indirect search strategies, including those from observations of dwarf spheroidals Ackermann et al. (2011); Geringer-Sameth & Koushiappas (2011), galaxy clusters Ackermann et al. (2010); Dugger et al. (2010), the cosmological diffuse background Abazajian et al. (2010); Abdo et al. (2010c), and nearby subhalos Buckley & Hooper (2010).

In Fig. 2.10, we show the 95% confidence level upper limits on the dark matter annihilation cross section for several choice of the final state, and for three values of the halo profile's inner slope. Based on the results of hydrodynamical simulations Gnedin et al. (2011a, 2004a), we consider the $\gamma = 1.2$ to represent the minimal degree of baryonic contraction, where as the $\gamma = 1.3$ and 1.4 cases should be taken as more central estimates.

The constraints we have derived from the Galactic Center region are indeed quite stringent. Even in the case of only a very modest degree of baryonic contraction ($\gamma = 1.2$), we find that dark matter particles with the canonical annihilation cross section of

35

$\sigma v = 3 \times 10^{-26}$ cm^3/s and which proceed to hadronic final states are predicted to exceed the observed gamma-ray flux from the Galactic Center unless they are more massive than approximately 300 GeV. In comparison, the Fermi collaboration's combined analysis of 10 dwarf spheroidals only excludes such dark matter particles with masses below approximately 30 GeV Ackermann et al. (2011); Geringer-Sameth & Koushiappas (2011).[7]

In Fig. 2.11, we also show the constraints which result if the effects of baryons on the dark matter distribution are neglected (using a uncontracted NFW profile). Even in this case, we find limits which are approximately as stringent as those derived from dwarf galaxies.

2.5   Discussion and Summary

In this chapter, we have used the first three years of data taken by the Fermi Gamma-Ray Space Telescope (FGST) to study the spectrum and spatial morphology of the gamma-ray emission from the region surrounding the Galactic Center. In doing so, we have identified a spatially extended component of gamma-ray emission which peaks at energies between approximately 300 MeV and 10 GeV. The origin of these gamma rays is currently uncertain, although they could potentially be the annihilation products of dark matter particles, or the products of collisions of high energy protons accelerated by the Milky Way's supermassive black hole with gas.

If this extended source of gamma rays is interpreted as dark matter annihilation products, the spectrum of this emission favors dark matter particles with a mass in the range

---

[7]Unlike the central regions of Milky Way-like halos, the dark matter density profiles of dwarf spheroidal galaxies are not generally expected to be contracted by baryons Governato et al. (2010); Oh et al. (2011). The uncontracted NFW profile adopted in the Fermi Collaboration dwarf spheroidal analysis is thus appropriate.

of 7-12 GeV (if annihilating dominantly to leptons) or 25-45 GeV (if annihilating dominantly to hadronic final states). The former of these mass ranges is of particular interest in light of the observations reported by the direct detection experiments DAMA/LIBRA Bernabei et al. (2010a), CoGeNT Aalseth et al. (2011c,a), and CRESST Angloher et al. (2012), which each report signals consistent with an approximately 10 GeV dark matter particle (see also, however, constraints from the CDMS Ahmed et al. (2011); Akerib et al. (2010) and XENON Aprile et al. (2011); Angle et al. (2011) collaborations, and related discussions Collar (2011a, 2010, 2011b)). Further motivating the dark matter interpretation of the Galactic Center gamma rays is the fact that the annihilation cross section required to normalize the annihilation rate to the observed flux is approximately equal to the value required to generate the observed cosmological abundance in the early universe ($\sigma v \sim 3 \times 10^{-26}$ cm^3/s). In other words, in lieu of resonances, coannihilations, P-wave suppression, or other complicating factors, a particle species that will freeze-out in the early universe with a density equal to the measured dark matter abundance is also predicted to annihilate today at a rate that is similar to that needed to produce the observed gamma rays from the Galactic Center.

Additionally, we point out that if dark matter particles are annihilating in the Inner Galaxy at the rate required to produce the observed gamma-ray flux, then the resulting energetic electrons and positrons will diffuse outward, potentially producing observable quantities of synchrotron emission. In particular, focusing on the case of 7-12 GeV dark matter particles annihilating dominantly to leptons, the halo profile and cross section required to produce the morphology and normalization of the observed gamma-ray flux is also predicted to lead to the production of a diffuse haze of synchrotron emission very similar to

that observed by WMAP Hooper et al. (2007); Finkbeiner (2004) (see Fig. 3 of Ref. Hooper & Linden (2011a) for a direct comparison). It also appears that the excess radio emission observed at higher galactic longitudes by the ARCADE 2 experiment Fixsen et al. (2011); Seiffert et al. (2011) possesses a spectral shape and overall intensity consistent with originating from dark matter with the same mass, cross section, dominant channels, and distribution Fornengo et al. (2011); Regis (2011). Lastly, we mention that 7-12 GeV dark matter particles with the distribution and annihilation cross section favored here would be capable of depositing the required energetic electrons into the Milky Way's non-thermal radio filaments Linden et al. (2011), providing an explanation for their peculiar spectral features.

It is noteworthy that the different explanations proposed for the observed gamma-ray emission from the Galactic Center predict different accompanying spectra of cosmic ray electrons, potentially providing us with a way to discriminate between these different scenarios. Of the sources proposed for the observed gamma-ray emission, only dark matter annihilations are predicted to produce comparable fluxes of gamma rays and electrons, with spectra that peak at similar energies. Pulsars, in contrast, produce gamma-ray spectra which peak at $\sim$1-3 GeV and electron spectra which peak at several hundred GeV Zhang & Cheng (2001). Perhaps future observations of the Inner Galaxy at radio and microwave frequencies will be able to make use of this comparison to shed light on the origin of the gamma-ray emission from the center of our galaxy.

Lastly, we have also presented conservative limits on the dark matter's annihilation cross section which are at least as stringent as those derived from other observations, such

as those of dwarf spheroidal galaxies.
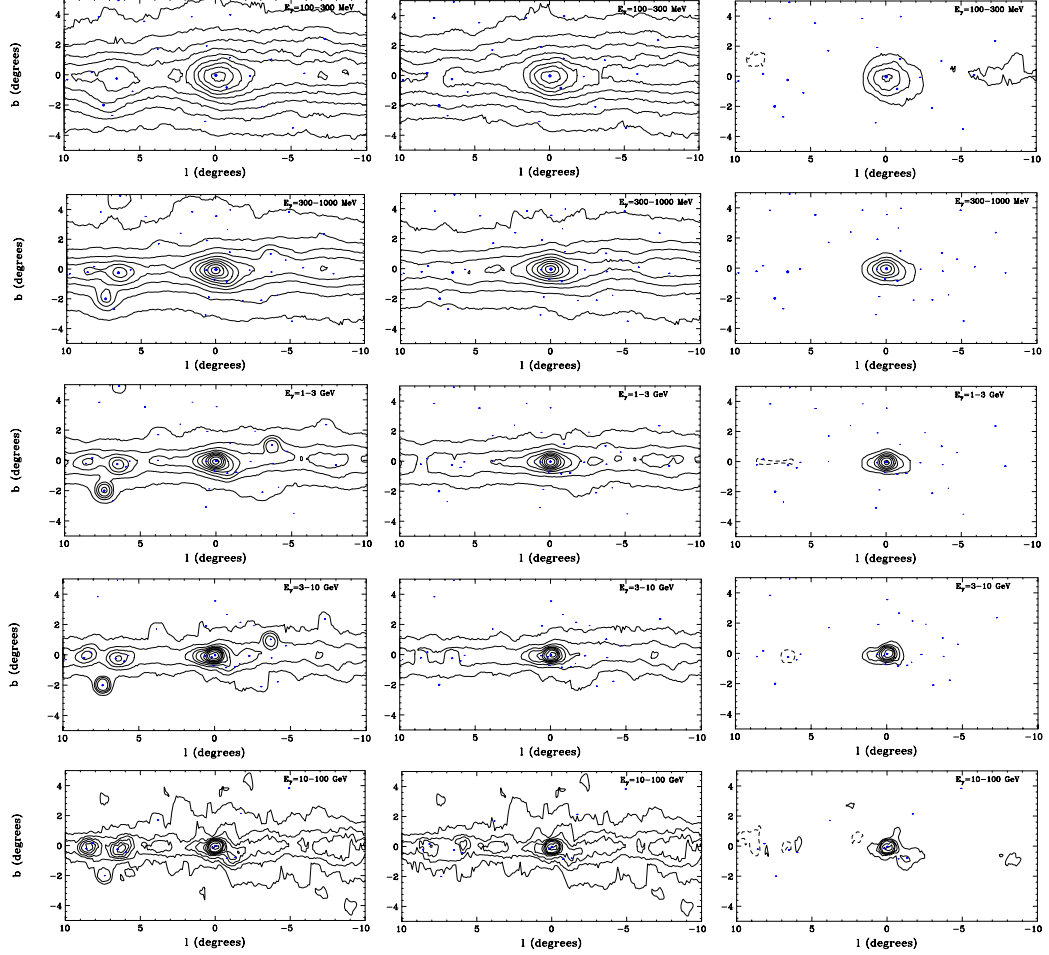
Figure 2.1 Contour maps of the gamma-ray flux from the region surrounding the Galactic Center, as observed by the Fermi Gamma-Ray Space Telescope. The left frames show the raw maps, while the center and right frames show the maps after subtracting known sources (not including the central source), and known sources plus emission from cosmic ray interactions with gas in the Galactic Disk, respectively. All maps have been smoothed over a scale of 0.5 degrees. See text for more details.

40
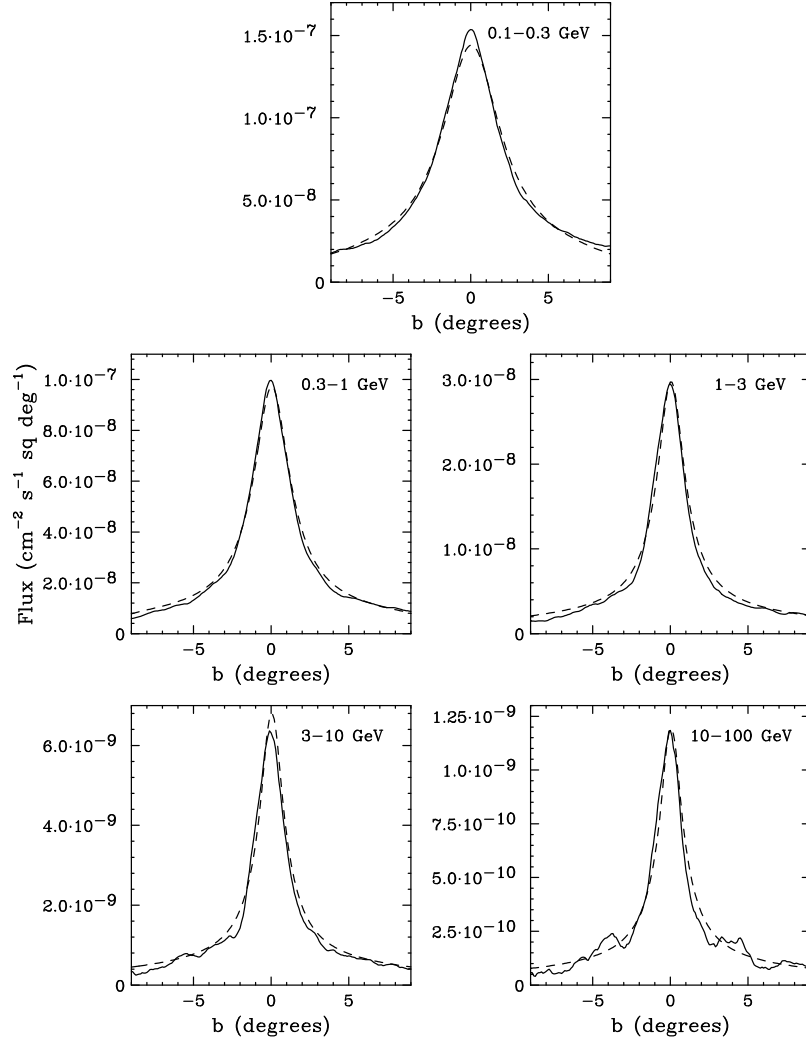
Figure 2.2 The observed gamma-ray flux (after subtracting known sources) averaged over $7° < |l| < 10°$ as a function of galactic latitude (solid), compared to that predicted from the line-of-sight gas density (dashes). See text for details.
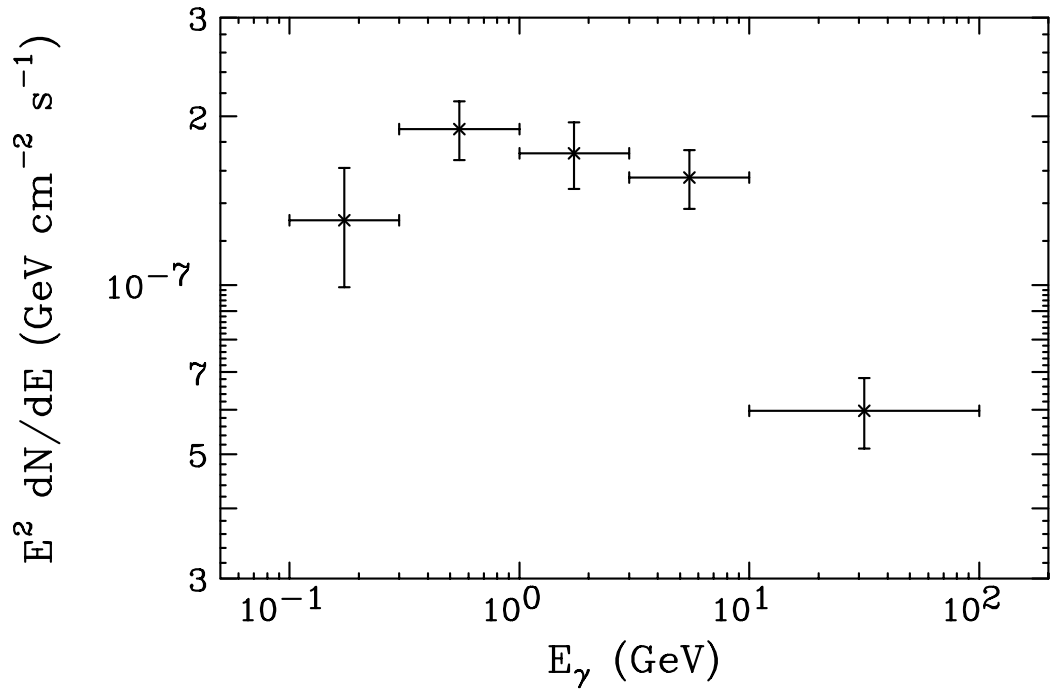
Figure 2.3 The spectrum of the residual emission from the inner 5 degrees surrounding the

Galactic Center, after subtracting the known sources and line-of-sight gas templates.
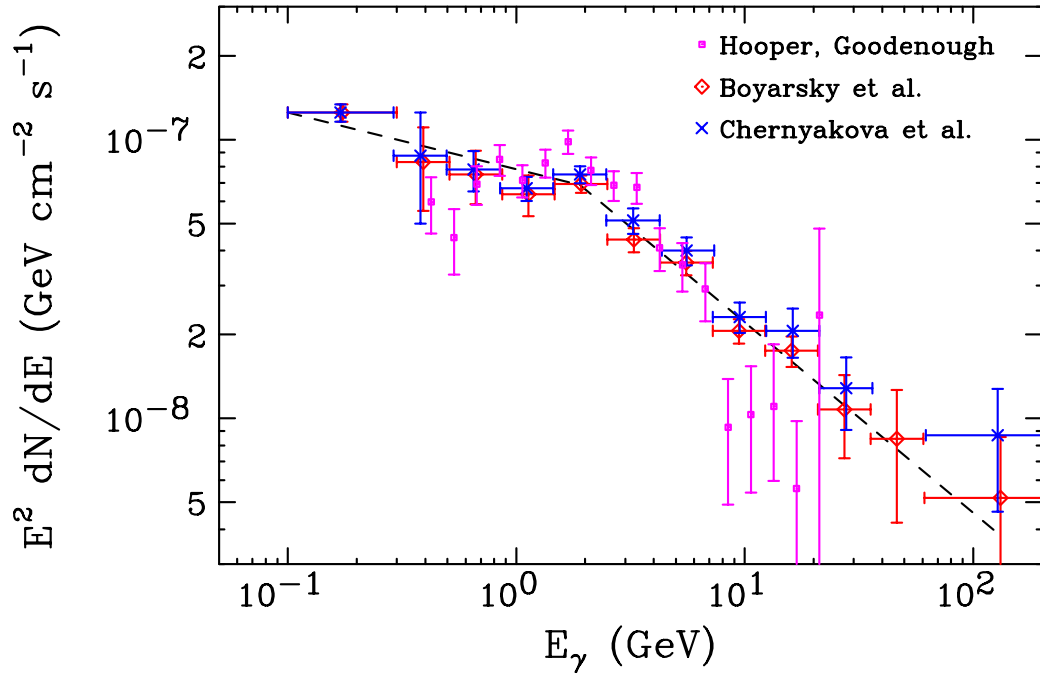
Figure 2.4 Fits for the spectrum of the central emission, assuming a point-like source morphology, from the previous work of three different groups Hooper & Goodenough (2011a); Boyarsky et al. (2011); Chernyakova et al. (2011). Despite the different analysis approaches taken, these fits are all in reasonable agreement. The dashed line is the broken power-law fit to this spectrum as presented in Ref. Chernyakova et al. (2011).
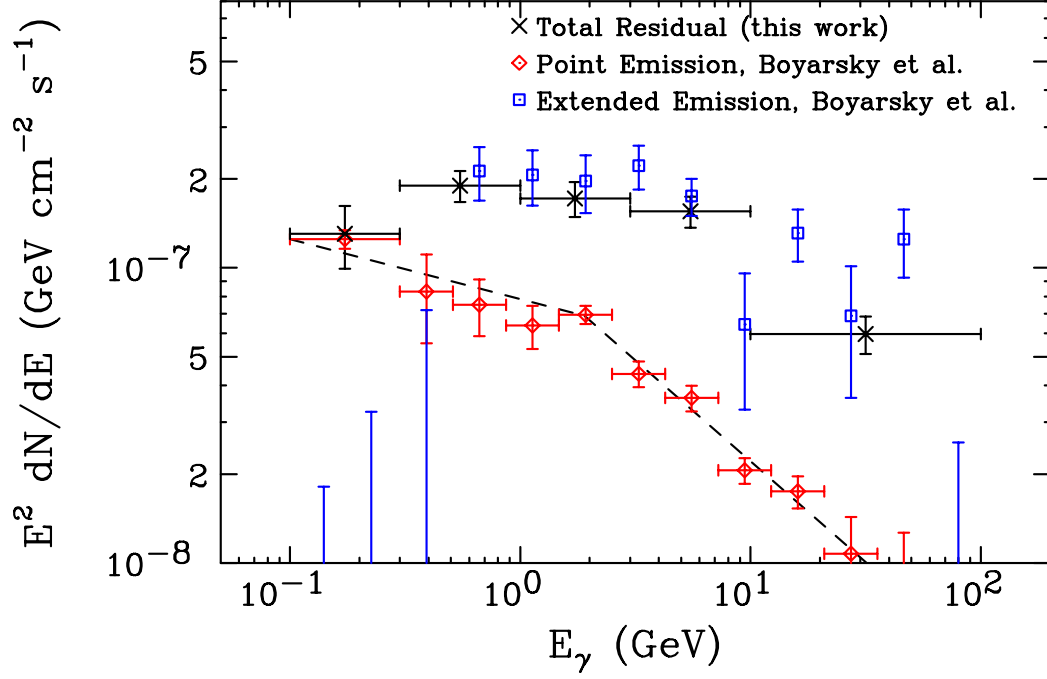
Figure 2.5 A comparison of the total residual emission found in this study (black) with the spectra of point-like emission (red) and extended emission (blue) (as in the case of annihilating dark matter with $\rho_{\text{DM}} \propto r^{-1.34}$) as presented in Ref. Boyarsky et al. (2011). This comparison supports our finding that this residual emission below ~ 300 MeV is consistent with a point-like source origin, while much of the emission at higher energies is indeed spatially extended.
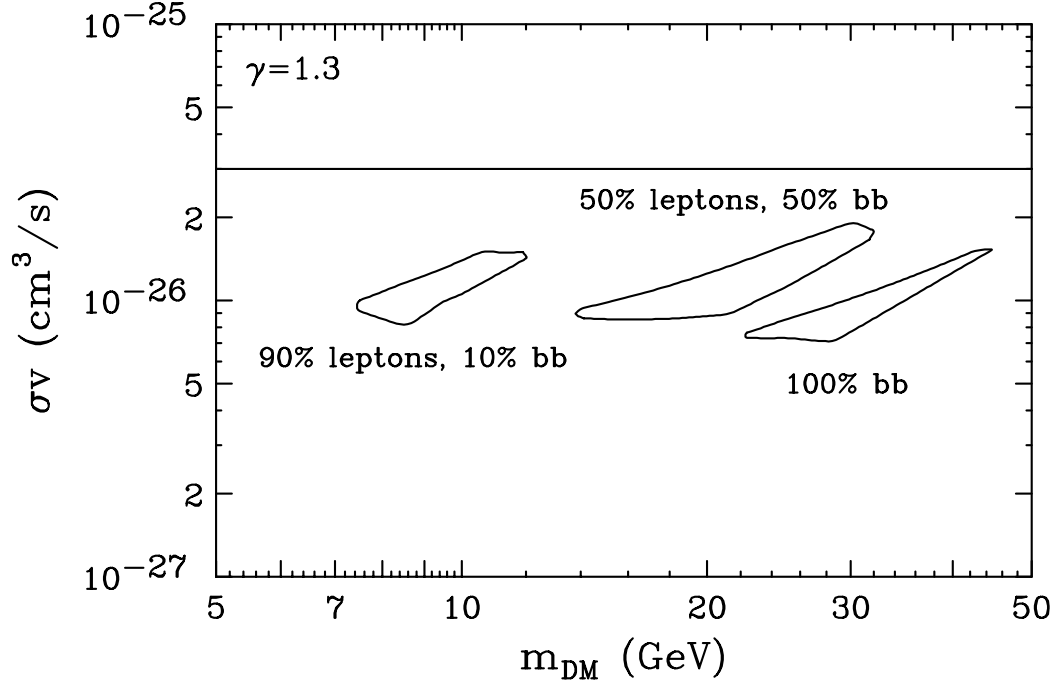
Figure 2.6 The range of dark matter masses and annihilation cross sections for which dark matter annihilations can account for the majority of the observed residual emission between 300 MeV and 10 GeV, for three choices of annihilation channels ("leptons" denotes equal fractions to e^+e^-, $\mu^+\mu^-$ and $\tau^+\tau^-$). Also shown for comparison is the annihilation cross section predicted for a simple thermal relic ($\sigma v = 3 \times 10^{-26}$ cm^3/s). Note that there is a factor of a few uncertainty in the annihilation cross section, corresponding to the overall dark matter density and distribution. See text for details.
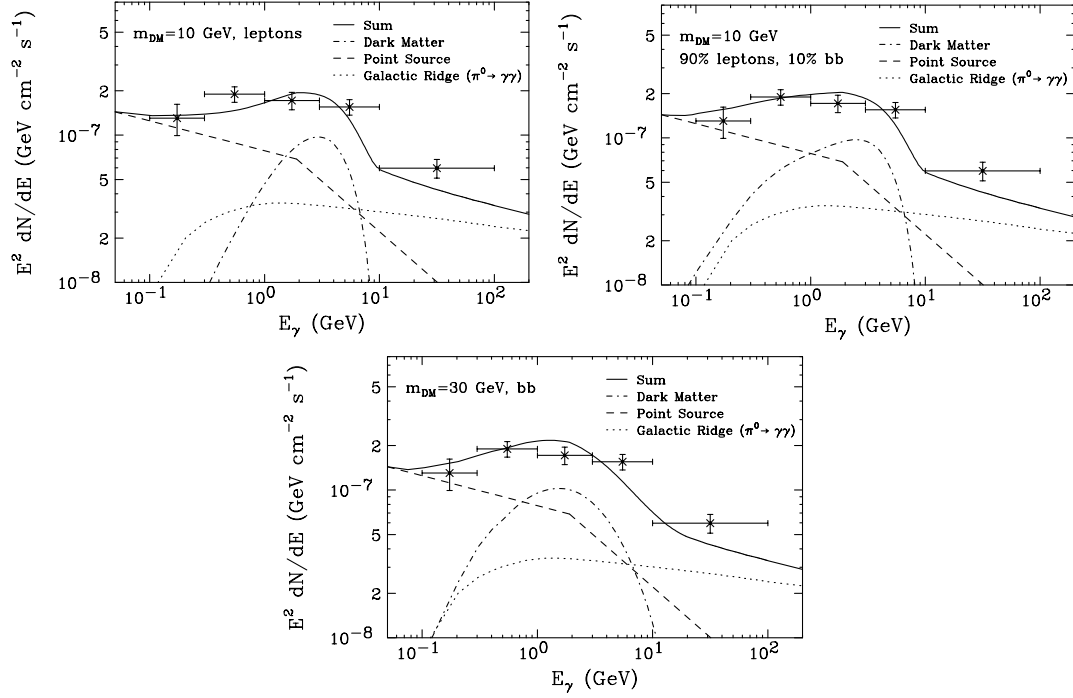
Figure 2.7 Examples illustrating how dark matter annihilations and astrophysical sources could combine to make up the observed residual emission surrounding the Galactic Center. In the upper left frame, we show results for a 10 GeV dark matter particle with an annihilation cross section of $\sigma v = 7 \times 10^{-27}$ cm^3/s and which annihilates only to leptons (e^+e^-, $\mu^+\mu^-$ and $\tau^+\tau^-$, 1/3 of the time to each). In the upper right frame, we show the same case, but with 10% of the annihilations proceeding to $b\bar{b}$. In the lower frame, we show results for a 30 GeV dark matter particle annihilating to $b\bar{b}$ with an annihilation cross section of $\sigma v = 6 \times 10^{-27}$ cm^3/s. In each case, the annihilation rate is normalized to a halo profile with $\gamma = 1.3$. The point source spectrum is taken as the broken power-law shown in Fig. 2.4, and the Galactic Ridge emission has been extrapolated from the higher energy spectrum reported by HESS Aharonian et al. (2006a), assuming a pion decay origin and a power-law proton spectrum. See text for details.
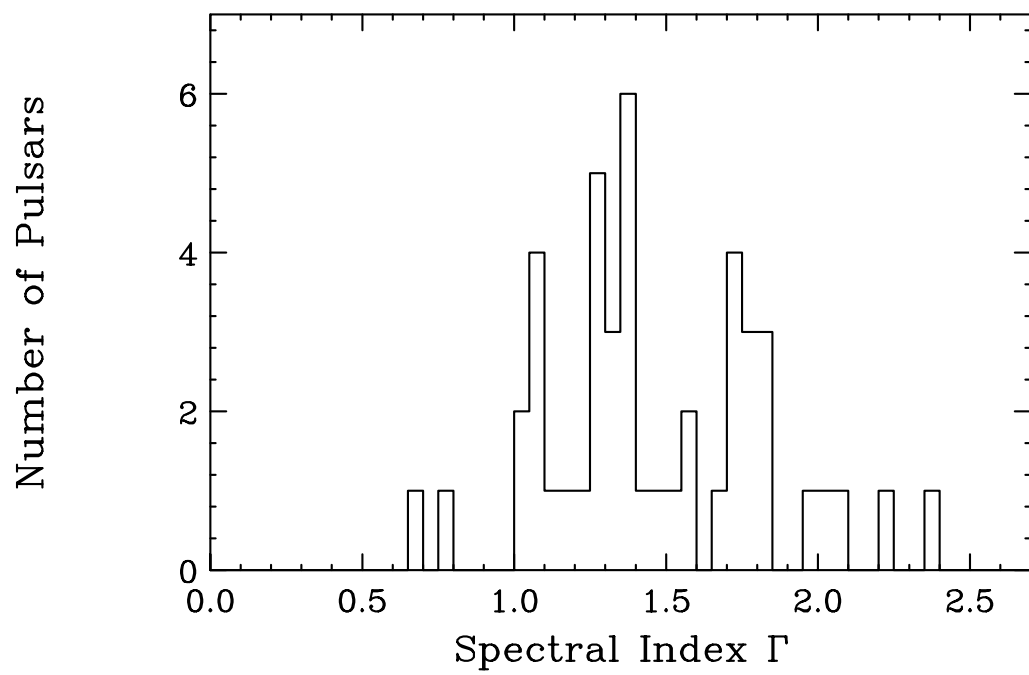
Figure 2.8 A histogram showing the distribution of spectral indices, Γ, of pulsars in the Fermi Pulsar Catalog.
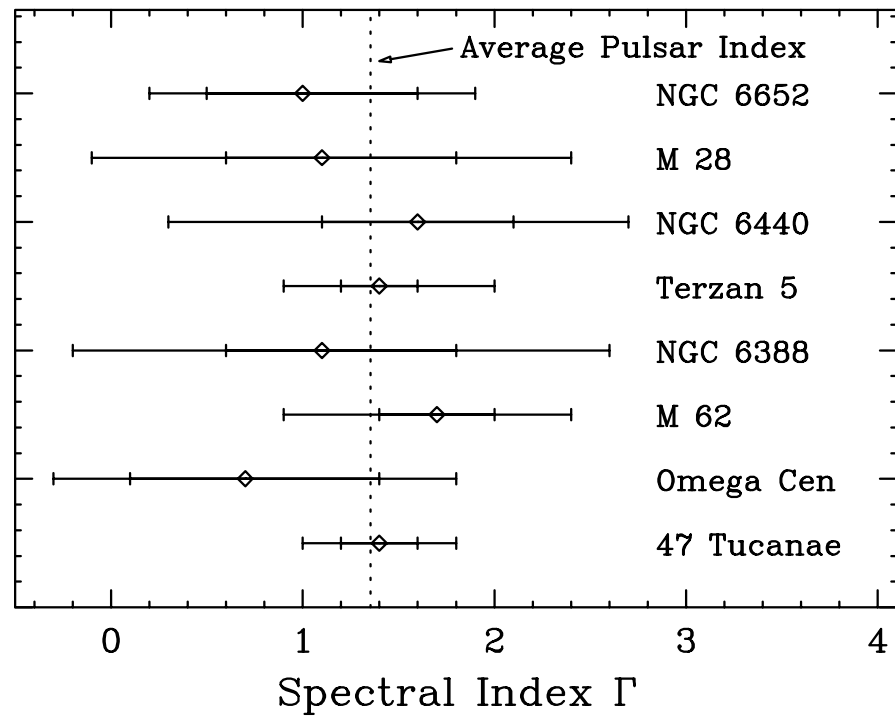
Figure 2.9 The spectral indices (with statistical and systematic error bars) of the eight globular clusters observed by the Fermi Gamma-Ray Space Telescope Abdo et al. (????).
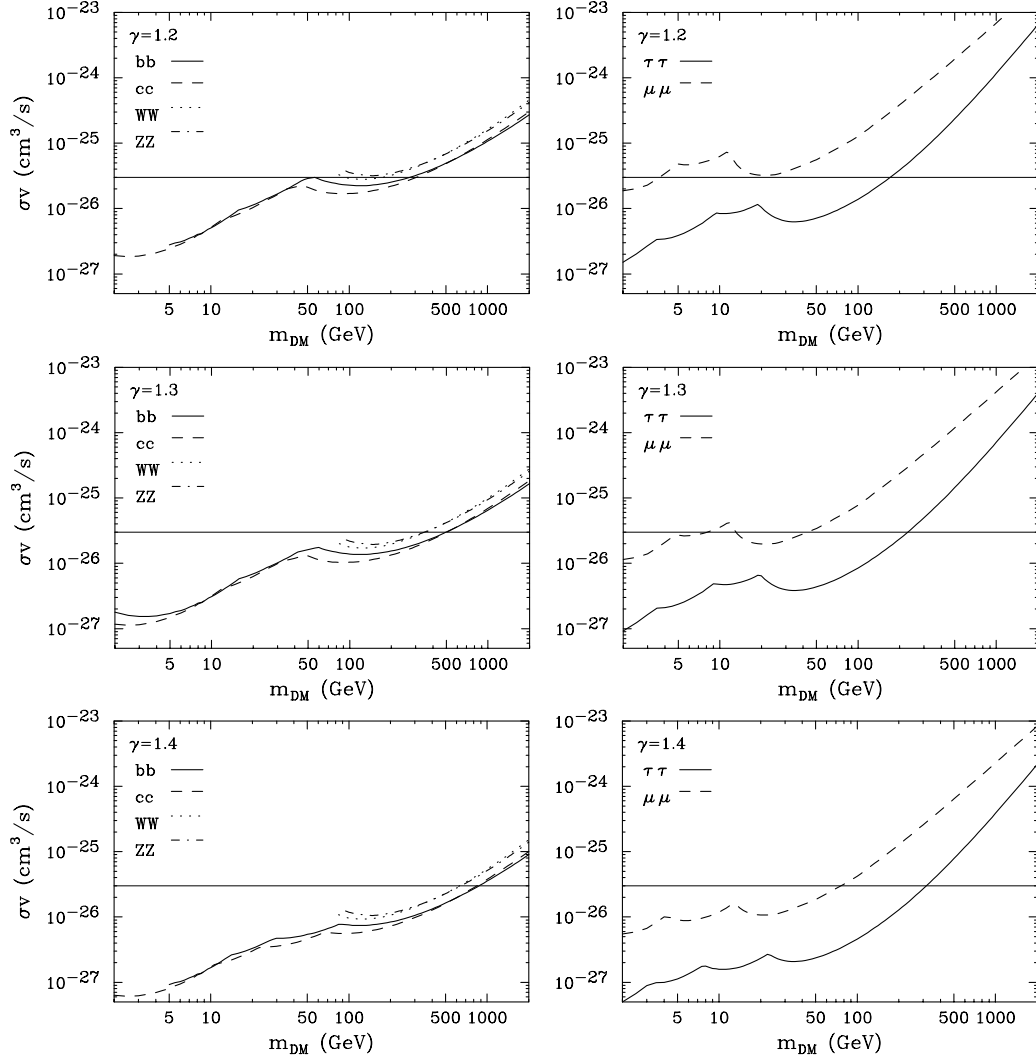
Figure 2.10 Upper limits on the dark matter annihilation cross section for several choices of the final state and for three values of the halo profile's inner slope, γ. Also shown for comparison is the annihilation cross section predicted for a simple thermal relic ($\sigma v = 3 \times 10^{-26}$ cm^3/s). Uncertainties in the overall dark matter density have not been included, but based on the errors presented in Ref. Iocco et al. (2011), we expect that this would only weaken our limits by about 30-50%. See text for more details.
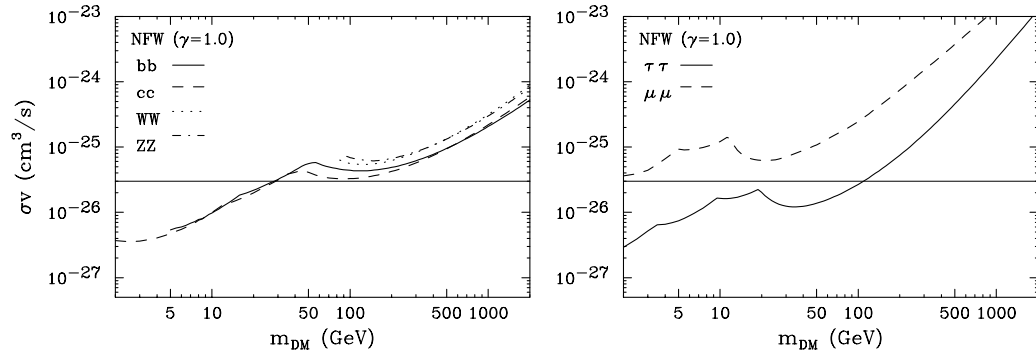
Figure 2.11 Upper limits on the dark matter annihilation cross section for several choice of the final state, neglecting the effects of baryons (using an uncontracted NFW halo profile). Also shown for comparison is the annihilation cross section predicted for a simple thermal relic ($\sigma v = 3 \times 10^{-26}$ cm^3/s). Uncertainties in the overall dark matter density have not been included, but based on the errors presented in Ref. Iocco et al. (2011); Catena & Ullio (2010a), we expect that this would only weaken our limits by about 30-50%. See text for more details.

Chapter 3

The Morphology of Hadronic Emission Models for the Gamma-Ray Source at the Galactic Center

Since COS-B and EGRET first observed a bright γ-ray source spatially coincident with the Galactic center (GC) Blitz et al. (1985); Mayer-Hasselwander et al. (1998), subsequent observations by the Large Area Telescope onboard the Fermi space observatory (Fermi-LAT) and by ground-based (imaging Atmospheric Cherenkov Telescope, ACT) γ-ray telescopes have repeatedly observed the GC region at energies spanning 100 MeV to 100 TeV. Unlike both radio and X-Ray observations of the GC, no variability has been observed in the high-energy regime, potentially indicating that the γ-ray emission mechanism

differs substantially from the low energy regime Chernyakova et al. (2011); Aharonian et al. (2009a). This distinction is especially stark in light of the order of magnitude increase in X-ray activity from the region observed in 2005, which was undetected in γ-ray data Aharonian et al. (2008a). This might be explained by models which generate the low-frequency (X-ray, IR, radio) emission very close to the central black hole (BH), while γ rays are produced farther away from the BH by high-energy protons inelastically scattering off of the interstellar medium, a framework originally posited by Aharonian & Neronov (2005b), and later by Liu et al. (2006a,c).

The strongest limits on the morphology of the gamma-ray source HESS J1745-290 are provided by Acero et al. (2010b) which used optical cameras mounted on each H.E.S.S. dish to calibrate the high-energy array, reducing the systematic error in the spatial pointing of the telescope. Using this technique, Acero et al. (2010b) found the source HESS J1745-290 to be spatially coincident with the radio source Sgr A*, within a total error radius of only 13", excluding the supernova remnant Sgr A East as the dominant source of γ-ray emission. However, the pulsar wind nebula G359.95-0.04 cannot be ruled out as a possible source of the high energy emission, and it may play a secondary or even a dominant role in the γ-ray emission observed from the galactic center. We note, however, that this possibility would not affect the analysis and conclusions presented here if the gamma-ray emission from the PSR was produced via the injection of high-energy protons into the galactic medium. HESS J1745-290 is found to be consistent with a point source to within approximately 1.2' at the 95% confidence level[1]. While this point source resides within a diffuse γ-ray background which is itself centered around Sgr A*, the total residual flux from the inner

---

[1]This corresponds to 2.96 pc under the assumption of a solar position 8.5 kpc from the GC.

0.1° is constrained to be less than 15% of the point-source flux Aharonian et al. (2006b). Work by Aharonian et al. (2009a) further constrained this diffuse emission to be relatively independent of the GC distance - indicating it may stem from cosmic-ray background events rather than a diffuse signal corresponding to the GC.

The LAT has also observed a point source, 1FGL J1745.6-2900c, spatially coincident with the GC region Abdo et al. (2010a), although a conclusive identification with Sgr A* was impossible due to the relatively low angular resolution of the instrument ($\sim 0.2°$ at 10 GeV). There are indications, however, that the GC signal observed by the Fermi-LAT is difficult to model as a simple point source. While independent point-source analyses by both Boyarsky et al. (2011) and Chernyakova et al. (2011) produced best-fit models assuming a point-source emission, the analysis of Hooper & Goodenough (2011a) found that the γ-ray emission extends spherically out to approximately 50 pc from the position of Sgr A*, falling off with a power-law of approximately $r^{-2.6}$. Hooper & Linden (2011c) pointed out two potential issues with GC point-source models at Fermi energies. First, a point-source best fit systematically over-estimates the source flux in the presence of an appreciable diffuse background. Secondly, even after accounting for surrounding point-sources and Galactic plane emission, the excess emission observed in the GC and not associated to the (best-fitted) point source, exceeds the point source luminosity by approximately a factor of three - in stark contrast to H.E.S.S observations at TeV energies. This second finding is consistent with the observation by Boyarsky et al. (2011) that the log-likelihood of the fit increased by 25 with the addition of a spherical symmetric parameter describing the spatial extension.

In addition to these morphological inconsistencies, the origin of the GC source spectrum at high-energy γ-ray frequencies is puzzling. A relatively hard spectrum in the 0.1-1 GeV range significantly softens in the 1-100 GeV region, then hardens again at TeV energies, before cutting off above 10 TeV. Leptonic models have been proposed to explain both the TeV emission Atoyan & Dermer (2004); Hinton & Aharonian (2007) and the GeV emission Kusunose & Takahara (2012). However, no theoretically compelling scenarios have been proposed to explain the entire gamma-ray spectrum a single leptonic source population.

Ballantyne et al. Ballantyne et al. (2007a) examined the possibility that the TeV signal observed by HESS could be explained by a significant emission of hard protons from Sgr A*, producing the gamma-ray emission through interactions with gas in the galactic center region, similar to the earlier models of Aharonian & Neronov (2005b). In order to examine the possibility that this emission be confined to the region near Sgr A*, they employed models for the morphology of Hydrogen gas in the GC from Rockefeller et al. (2004), which include a large "ring" of overdense gas surrounding the GC at distances from 1-3 pc. This dense structure, aptly named the circumnuclear ring (hereafter CNR), has long been observed by far-infrared instruments as a torus-shaped structure inclined $20°$ with respect to the Galactic plane and surrounding a relative underdensity of gas within the inner pc around the GC Becklin et al. (1982a). Ballantyne et al. (2007a) then calculated the diffusion of charged protons within tangled magnetic fields with strength proportional to the local Hydrogen density. Using these models, they calculated the expected interaction probability between high energy protons and the CNR as a function of energy, finding approximately 73% of protons emitted from the GC to encounter the CNR for protons with

energies between 1-2.5 TeV. However they found this interaction probability to fall quickly with increasing proton energy due to the increasing gyroradius of high energy protons - only 47% and 5% of protons are found to encounter the CNR at energies of 10 and 100 TeV respectively. Due to the extreme overdensity of hydrogen gas in the CNR, Ballantyne et al. (2007a) assumed that protons encountering the CNR would lose energy quickly through pion collisions, while protons which avoid the ring would lose energy at larger radii, producing an extended gamma-ray emission at higher energy.

Recently Chernyakova et al. (2011) further examined the hadronic scenario, additionally positing that the whole GeV-TeV γ-ray emission may be explained by the injection of high energy protons at the GC. This interpretation has several natural advantages in explaining the entire γ-ray spectrum, including: (1) the hard spectrum below 1 GeV is naturally explained by the inability of protons with kinetic energy below $\sim$300 MeV to produce π^0 in p-p collisions, (2) the bump in low energy γ-ray emission is produced by diffusively trapped protons which lose significant energy while propagating through the GC region, (3) the flat spectrum at TeV energies is explained by protons which propagate rectilinearly through the GC region, without losing significant energy in p-p collisions, which provides a convincing match to the $\sim$E^{-2} γ-ray spectrum by using the E^{-2} proton injection spectrum derived from first-order Fermi acceleration, and (4) the turnover between the GeV and TeV emission is naturally explained as the transition between diffusive and rectilinear motion - creating a soft spectrum between these two energy regimes. Chernyakova et al. (2011) also consider the possibility that two distinct proton populations are responsible for the low- and the high-energy γ-ray emission.

In the present study we focus on the *morphology* of the GC γ-ray source. Specifically, we introduce a detailed model of the interstellar gas distribution near the GC, and demonstrate that the γ-ray morphology from hadronic emission is determined primarily by the distribution of target gas rather than by the parameters describing the diffusion of high-energy protons. We find that in any scenario for cosmic ray diffusion, the bulk of the high-energy emission falls within the point-spread function of all current γ-ray telescopes. However, we note that this will not be the case for the proposed Cherenkov Telescope Array (CTA), which will have the angular resolution required to observe a morphology in the γ-ray source which shadows the observed gas density CTA Collaboration (2011). The outline of this study is as follows: Sec. 3.1 describes the model we employ for the GC gas density; Sec. 3.2 gives qualitative arguments to describe cosmic ray proton propagation in the GC region, while in Sec. 3.3 and 4.2 we present our results for the proton population and for the γ-ray emission in hadronic models for the GeV-TeV emission.

3.1 Gas Density near the Galactic Center

Detailed knowledge of the gas density is critical to accurately describing hadronic γ-ray emission from the GC region. Here we employ the model of Ferriere (2012), valid for the inner $\sim$10 pc around the GC. This model not only includes a diffuse halo, but also contributions from the CNR, Sgr A East, M-0.13-0.08 and M-0.02-0.07 as well as bridges and streamers connecting them. We make several necessary simplifications to the model before utilizing it within our numerical code. First, we create a spherical model by calculating the average gas density at each radius r. In doing this, we take a central value for the position of

M-0.13-0.08 and make geometric approximations for the position of the various streamers, keeping the total volume consistent with Ferriere (2012). We note that this will have the effect of artificially making the γ-ray emission spherically symmetric. However, in the limit that both the proton diffusion is spherically symmetric, and the probability of multiple interactions between a single cosmic ray proton and the interstellar medium is low, the total emission from within a given radial bin is conserved when the gas density is smeared. We will discuss these assumptions in detail later, and we will show that they are valid for the majority of the parameter space discussed. Secondly, we ignore the thermal distribution of gas, which is valid in the limit where we only consider collisions with highly-relativistic protons.

To extend our simulations beyond 10 pc from the GC in order to capture the region relevant for the Fermi-LAT PSF, we adopt the model of Eqs. 18 and 19 of Ferrière et al. (2007) and impose again spherical symmetry. With these assumptions, we obtain gas densities which are lower than those in Ferriere (2012) by an order of magnitude at a radius of 10 pc. Since the models of Ferriere (2012) are only suffering incompleteness at radii greater than 10 pc (due to unmodeled sources), we assume the gas density at a given radius to be the larger of the values quoted by Ferrière et al. (2007) or Ferriere (2012). This causes us to switch between models at a radius of 19.2 pc. In Figure 3.1 we show the resulting density of hydrogen gas in our simulation as a function of the radius from the GC. We note that the morphology is dominated by the CNR, which provides a large boost to the gas density between 1-3 pc.

Parameter	Value from Cherenkova	Value Adopted Here
Radial Size of Simulation Region	3 pc	50 pc
Duration of Proton Emission	$300 - 10^4$ yr	10^{10} yr
Proton Injection Spectrum	$-1.9 - -2.0$	-1.9
^{1}H Density during proton diffusion	1000 cm^{-3}	1000 cm^{-3}
^{1}H Density for γ-ray calculation	1000 cm^{-3}	See Figure 1

Table 3.1 List of all input parameters which differ between the assumptions of Chernyakova et al. (2011) and the present work.

3.2 A Qualitative Model

In order to understand the morphology of the hadronic emission, we consider propagation in four limiting regimes, controlled by two parameters. Protons may propagate either rectilinearly or diffusively through the GC region, and they may either undergo many, or much less than one, collision with the surrounding gas. While intermediate cases are possible, we find these four limiting cases to confine the expected proton morphology.

We first investigate the propagation of protons in the rectilinear regime. This can be thought of as diffusion with a mean-free-path exceeding the confinement region of the simulation, yielding a diffusion constant $D = l_{sim}^2/(6\tau)$, where l_{sim} is the region we are considering, and τ is the propagation time out of the region. For our 50 pc simulation and assuming relativistic propagation velocities, this corresponds to a minimum D > 7.7 x 10^{29} cm^{2}s^{-1} for particles to propagate rectilinearly out of the simulation zone. We can calculate the probability of a proton-proton interaction between the cosmic ray and a target gas molecule as

$$P_{pp} = \sigma_{pp}(E) \int_{\vec{r}(0)}^{\vec{r}(t)} \rho_H(\vec{r}(t'))dt' \tag{3.1}$$

58

where $\sigma_{pp}(E)$ is the cross-section between a proton with Energy E and a cold target proton, ρ_H is the gas density as a function of position, and $\vec{r}(t)$ is the radial position as a function of time from the injection of the cosmic ray until it leaves the diffusion zone. In the case of spherical symmetry and rectilinear propagation out of the center of the diffusion zone, we set r(t') = ct', r(0) = 0, and r(t) = r_{max}, and then using the gas density shown in Figure 3.1, infer an interaction probability of $\sim$2.5% between a given proton and the target gas before the proton escapes the 50 pc region. In this case, relativistic protons lose little energy as they propagate through the region, and the proton spectrum mirrors the injected spectrum. Since the number of protons in a spherical shell δr is constant for rectilinear propagation, the resulting γ-ray morphology mirrors the gas distribution shown in Figure 3.1. In this scenario 87% of the total γ-ray emission is concentrated within the inner 3 pc surrounding the GC. If, as expected, this scenario describes the propagation of the $\sim$10 TeV protons responsible for the TeV γ-ray signal, then this ratio stands in excellent agreement with HESS observations indicating at least 85% of γ-ray TeV emission to be contained in the inner 3 pc. We note that so long as we assume rectilinear propagation, this conclusion still holds in the case of a true 3D model of the gas density, and the final emission morphology is calculable by convolving the $\rho(r) \sim r^{-2}$ density of protons with the observed gas density (e.g., Ferriere (2012)) and integrating over the line of sight.

We note that for the gas densities and distance scales modeled here, the second possible regime, where the diffusion is rectilinear but protons undergo more than one collision with the target gas is insignificant, since the probability of having even one collision is only $\sim$2.5%. Thus we exclude the second regime.

A third regime exists when protons propagate diffusively through the region, but interact with the Galactic gas fewer than once. In this case, we can assume that the energy spectrum of protons remains constant with radius, and calculate the density of protons to fall off as $\rho(r) \sim r^{-1}$, causing the number of protons within a radial bin to increase linearly with radius. In this case, we can directly calculate the morphology of the resulting γ-ray emission by using the gas density shown in Figure 3.1, but weighting the gas density by the number of protons in each radial bin, which varies linearly with r. Weighted in this manner, we calculate the average n_H density as 410 cm^{-3}, and find the minimum diffusion constant for which less than 0.1 interaction occurs to be 2.4 x 10^{27} cm^{3}s^{-1}. In this limit, the expected γ-ray morphology results from convolving the gas density in Figure 3.1 with a proton spectrum which is constant in radius and has an overall density $\rho(r) \sim r^{-1}$: the γ-ray morphology is therefore still dominated by the CNR, mirroring what was found in first regime.

Lastly, we evaluate the regime where diffusive cosmic rays are expected to interact multiple times with interstellar gas before diffusing out of the GC region. In this case, the final cosmic ray energy spectrum is not radius independent, and cannot be easily computed. Furthermore, we note that in this regime, the non-spherically symmetric nature of the gas becomes important in determining the steady-state cosmic-ray density, as interactions which occur while protons move through particularly high-density regions may have an effect on the surrounding proton distribution. However, we note that, so long as the injection proton energy spectrum is sufficiently steep that partially cooled high energy protons are sub-dominant to the injected low energy population, this cosmic ray density is unambiguously

constrained to fall off faster with increasing radius than in the one-interaction regime above. In order to provide more quantitative calculations, we defer to a numerical model for the propagation of high energy particles throughout the GC region.

We note that the r^{-1} dependence of cosmic-rays propagating diffusively out of the galactic center, closely mirrors the brightness profile of gamma-ray emission calculated by Chernyakova et al. (2011) (Figure 7) for cosmic rays of 1-10 GeV. This is expected, as these models use a constant Hydrogen density, creating a one-to-one correspondence between the proton density and the brightness profile. Notice that the diffusion constant at 1-10 GeV employed by Chernyakova et al. (2011) fall between 9.5 x 10^{26} and 7.6 x 10^{27} cm^2s^{-1}, which lands squarely in the regime of diffusion with fewer than one interaction per cosmic ray (using a region with radius 3 pc and a gas density of 1000 cm^{-3}). In the lower energy bin of 0.1-1 GeV, the significantly smaller diffusion constant leads to multiple interactions between high energy protons and the target gas, leading to a more constrained distribution, as predicted in our qualitative model.

3.3   Propagation of High-energy Protons

In order to simulate the propagation of protons from a central source, we adopt the formalism of Aloisio et al. (2009), which seeks to model spherically symmetric diffusion while avoiding the issue of superluminal propagation. We note that this cosmic-ray diffusion model is nearly identical to that employed by Chernyakova et al. (2011) and we refer the reader to that work for relevant details of our simulation parameters. In Table 3.1 we list all differences between our model and that of Chernyakova et al. (2011). Most importantly, we

employ a much larger simulation region with a 50 pc radius, in order to capture the entirety of emission within the Fermi PSF. In order to obtain a steady state diffusion solution over this period, we must assume that the the emission continues for periods longer than the 10^4 yr assumed in Chernyakova et al. (2011). Since we are only concerned with the upper limit for the source extension in this work, we allow the emission to continue for 10^{10} yr, but note that the equation becomes steady state after approximately 10^6 yr.

We adopt a differential proton injection spectrum which follows a power law $\sim$E$^{-1.9}$ with an exponential cutoff at 100 TeV. We normalize this injection spectrum in order to obtain a γ-ray intensity matching the Fermi and HESS fluxes reported by Chernyakova et al. (2011) at a radius of 3 pc, and then extend our simulation from this point out to 50 pc. We find that this translates to an injected proton luminosity of 8.8 x 10^{36} erg s^{-1}.

For simplicity, we utilize an average target density n$_H$ = 1000 cm^{-3} in our calculation of the final proton density (but not for the final γ-ray emission, for which we employ the target gas density given by Figure 3.1). This is an immaterial assumption, so long as we reside in a limit where the average proton undergoes much less than one collision with gas - an assumption which holds throughout the vast majority of our parameter space. We calculate the γ-ray emission from the steady-state proton density distribution employing the formalisms of Kamae et al. (2006). We note that we consider here only contributions from γ-rays produced directly in the p-p collision, and ignore possible γ-ray contributions due to the inverse-Compton scattering (ICS) of photons by leptons produced in the same collisions. This approximation is reasonable both because ICS contributes at significantly lower energies than the direct γ-ray channel (and will thus be subdominant to the larger proton

flux at lower energies), and because the magnetic fields are expected to peak strongly in this region, forcing the ICS to be highly subdominant to synchrotron production Crocker et al. (2010). We note that variations in the diffusion parameters are constrained by the transition between the GeV-TeV spectrum, and yielded no qualitative changes in the findings outlined below.

3.4   Results

In Figure 3.2, we show the spectral energy distribution of the γ-ray signal within cones corresponding to varying radii. We note that more than 50% of the residual emission is found within 3 pc at all energies, and the majority of this emission is created between 1-3 pc from the GC, when the emitted protons interact with the dense CNR. In Figure 3.3, we instead show the differential (top panel) and integrated (bottom) emission as a function of radius at various fixed energies. In the top panel, we show the total emission in radial shells of 1 pc width, while in the bottom panel we show the integrated emission within a given radius.

We note that these features correspond closely to the expectations from Section 3.2. For instance, at energies of 10 TeV the emission is dominated by a proton population of approximately 100 TeV, which propagates rectilinearly in our simulation. We find the γ-ray emission contained within 3 pc and 10 pc to be 87% and 95% respectively, matching the expectations from rectilinear propagation. At energies of 10 GeV, the γ-ray signal is dominated by 100 GeV electrons which propagate diffusively but undergo Poissonian interactions. In this case we calculate the γ-ray emission contained within 3 pc and 10 pc

to be 61% and 78% respectively, closely matching an r^{-1} proton density.

Finally, in Figure 3.3 (bottom) we show with vertical lines the approximate angular resolutions of front converting events from the Fermi-LAT at 10 GeV (28 pc, orange solid), and at 100 GeV (18 pc, gray dotted), HESS (11 pc, gray long-dashed Aharonian et al. (2006f)), the HESS 95% confidence limit on the maximum source extension(3 pc, gray short-dashed, Acero et al. (2010b)) and the anticipated proposed resolution of CTA (CTA Collaboration, 2011, 2.5 pc, light blue dash-dot). We note that the angular resolution for the Fermi-LAT at 1 GeV is approximately 90 pc and is outside the plotted range. For all existing telescopes, the modeled radial dependence could easily be confused with a point source located at the GC. However, similarly to HESS, CTA will be able to place limits on the source extension which are a factor of few smaller than the quoted angular resolution. In this case, CTA will clearly detect structure in the γ-ray signal, including, possibly, bright emission coincident with the CNR. We expect that this signature would provide extremely strong evidence in favor or against the hadronic nature of this emission.

3.5   Discussion and Conclusions

We have shown that hadronic emission stemming from the inner 3 pc of the Galaxy and following a power-law injection spectrum compatible with Fermi acceleration will naturally produce an emission spectrum comparable to that observed by both HESS and the Fermi-LAT. We showed analytically and numerically that the morphology of γ-ray emission is determined primarily by the gas morphology, and the majority of the emission falls below the PSF of all current γ-ray telescopes. While this is in extremely good agreement

with HESS observations reporting 85% of the TeV emission to be confined within 3 pc of the GC Aharonian et al. (2006b), the hadronic model is currently in some tension with Fermi-LAT observations which imply that the GC source may be extended.

Specifically, our models find 71% and 86% of the 1 GeV γ-ray emission to fall within 3 pc and 10 pc from the GC respectively. This result stands, at face value, in some tension with Fermi-LAT observations of the GC Hooper & Linden (2011c). After background subtraction, Hooper & Linden (2011c) find a residual emission which is not well-modeled by a point source convolved with the Fermi-LAT PSF. If modeled as an extended emission from dark matter (but independent of any dark matter properties), they derive a best-fit power-law fall-off to the emission $\sim r^{-2.6}$, which indicates that roughly 32% and 53% of the γ-ray signal should originate within 3 pc and 10 pc of the GC.

It is important to remark that it will be difficult to definitively conclude that hadronic models are ruled out by Fermi observations, as significant background subtraction is necessary in order to determine the residual background signal which should be observed by the Fermi-LAT. This includes a dominant foreground from emission in the galactic plane which lies along the line of sight between the solar position and the galactic plane Hooper & Linden (2011c). This intensity of residual emission can be further complicated by uncertainties in the modeling of point source contributions at the galactic center Boyarsky et al. (2011). Lastly, the γ-ray morphology for hadronic models is neither point-like nor power-law with radius, making it difficult to directly compare these results with previous works. Still, our results indicate that a substantial source extension in Fermi-LAT data is not expected from hadronic emission models.

It may appear that the conclusion above can be circumvented if the hadronic emission from the GC is highly polar, allowing protons to propagate out of the central 3 pc while avoiding the CNR. However, this is difficult to reconcile with TeV observations: with purely polar injection, we find that HESS would clearly observe an extended source above and below the Galactic plane. Our conclusions would also be affected if the GeV emission mechanism were distinct from the TeV emission – either due to different primary proton populations or to multiple low-energy hadronic sources contributing to the GeV but not to the TeV emission.

Notice that a time dependence in the hadronic emission could be engineered to provide an energy-dependent source extension. Further multiwavelength observations will be necessary to constrain this scenario. Another alternative pertains to the possibility that the CNR is not a stable feature of the galactic-center region, but is instead transient in nature. While studies of galactic tracers such as HCN and HCO^+ found extremely high gas masses of approximately 10^6 $M_\odot$, which would be stable against tidal disruption by the supermassive-black hole Christopher et al. (2005); Montero-Castaño et al. (2009), very recent observations using the GREAT telescope to perform a CO excitation analysis Requena-Torres et al. (2012) obtain a best fit which reduces the total mass of the CNR by approximately two orders of magnitude, and thus find the CNR to be susceptible to tidal disruption, implying that the feature could be transient. We note that the density used in this chapter, based on the central value reported by Ferriere (2012) stands at 2 x 10^5 $M_\odot$, in between these extreme values. The implication of a transient CNR in the context of this work is difficult to positively determine, as it would depend sensitively on the effect of the

CNR not only on the gas density, but on the diffusion parameters of the region as well. If the latter effect is neglected, then it is possible that the fall-in of the CNR would lead to enhanced low-energy emission, as protons at this energy have built up without losing significant energy until the CNR moves into regions with higher proton density nearer the GC.

We note that while our work considers a similar model for the gas density near the GC to that of Ballantyne et al. (2007a), we obtain an energy dependence for the gamma-ray morphology which is qualitatively different. Specifically, Ballantyne et al. (2007a) calculates the probability of a cosmic ray proton entering the CNR before it diffuses out of the target region. Since this probability will decrease as the protons mean free path becomes larger, they determine that the gamma-ray morphology should become more diffuse at high energy. However, this implicitly assumes that gamma rays moving through the CNR efficiently lose their energy before leaving the region. However, employing the model for Hydrogen in the CNR determined by Ferriere (2012), and using a model where the propagation of TeV photons is rectilinear on the distance scale inhabited by the CNR, we find that protons escape from the CNR with only negligible energy losses. Additionally, we find that these energy losses remain negligible even through the majority of the diffusive regime.

This creates a significant difference in the necessary proton injection spectra necessary to match the HESS dataset in this work, compared to that of Ballantyne et al. (2007a). In our work the existence of rectilinear proton propagation throughout the HESS regime implies that the injected $E^{-1.9}$ proton produces an almost equivalent $E^{-1.9}$ gamma-ray spectrum. However, in the work of Ballantyne et al. (2007a) the decreasing interaction

probability between high energy protons and the molecular gas requires a much harder injected proton spectrum ($E^{-0.75}$) to account for the observed gamma-ray spectrum. Finally, we note that while the percentage of high energy emission contained within the inner 3 pc in our model is similar to the probability of a 1 TeV proton encountering the CNR as determined by Ballantyne et al. (2007a), this is fairly coincidental: the relative emission in our model depends sensitively on the Hydrogen gas density outside of the inner 3 pc, which is not taken to account in the model of Ballantyne et al. (2007a).

Finally, we note that the greatly improved angular resolution of CTA will provide a much crisper picture than current instruments - potentially leading to the observation of both a central deficit of γ rays in the central pc from the GC, and of a bright ring of emission coincident with the position of the CNR if the GC source is of hadronic nature. This morphology would be difficult to explain with leptonic or dark matter scenarios, which would not be expected to correlate with the local gas density. Thus we believe that future CTA observations will convincingly confirm or rule out the hadronic emission scenario presented here.
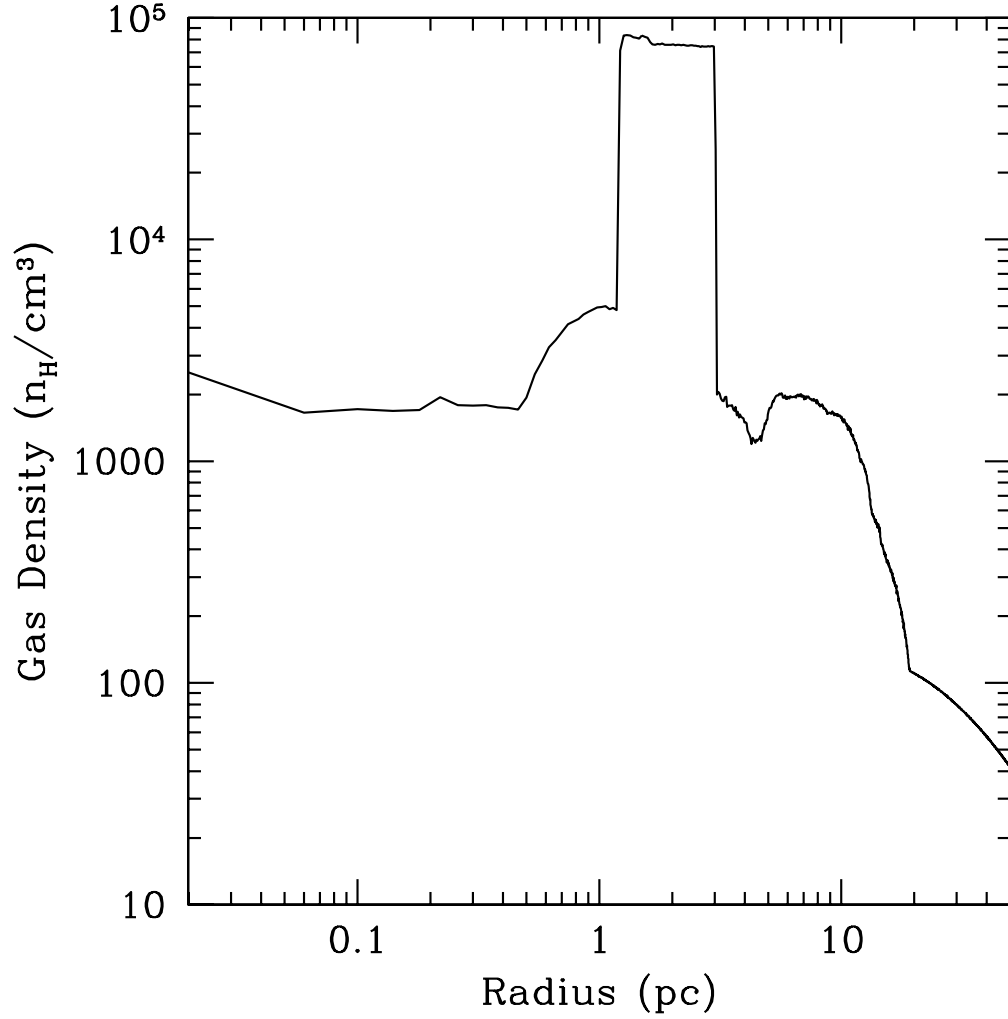
Figure 3.1 Gas density (n_H/cm^3) averaged over solid angle as a function of radius from the GC (pc) obtained from a combination of the work of Ferrière et al. (2007) and Ferriere (2012) (see the text). The major feature in the gas density stems from the circum-nuclear ring (CNR, 1.2 pc to 3.0 pc) which contributes a gas density nearly two orders of magnitude larger than any other structure.
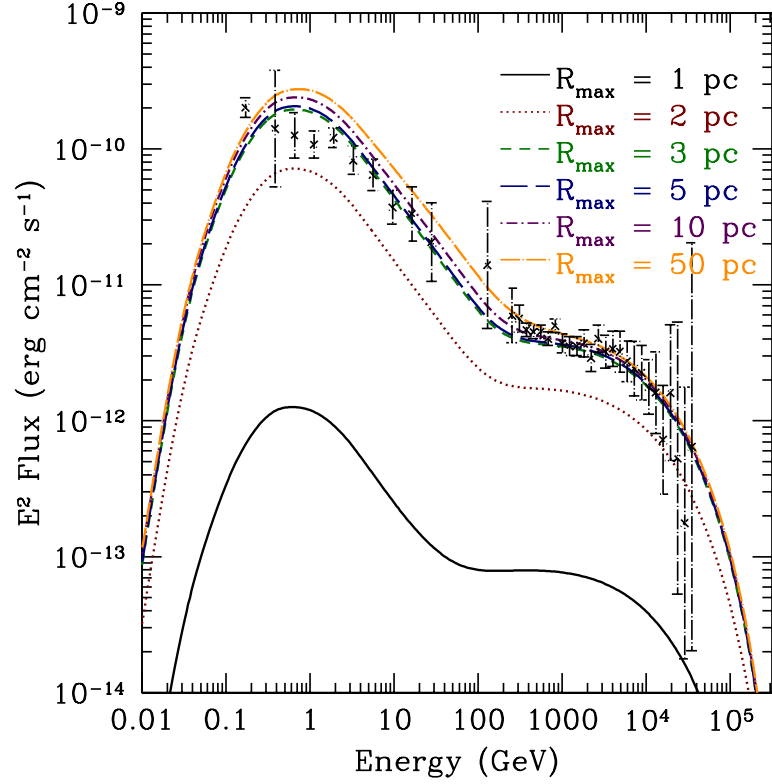
Figure 3.2 Spectral energy distribution of γ-ray emission within radial cones of various size ranging from r < 1 pc to r < 50 pc. We note that the emission falls off very quickly after 3 pc, with almost no additional intensity for additional radial bins beyond this point. The overall intensity is normalized such that the emission within 3 pc matches the Fermi and HESS fluxes as reported by Chernyakova et al. (2011). Due to the higher n_H in our simulation and longer emission period, this corresponds to a lower proton injected luminosity of 7.0 x 10^{35} erg s^{-1} into protons.
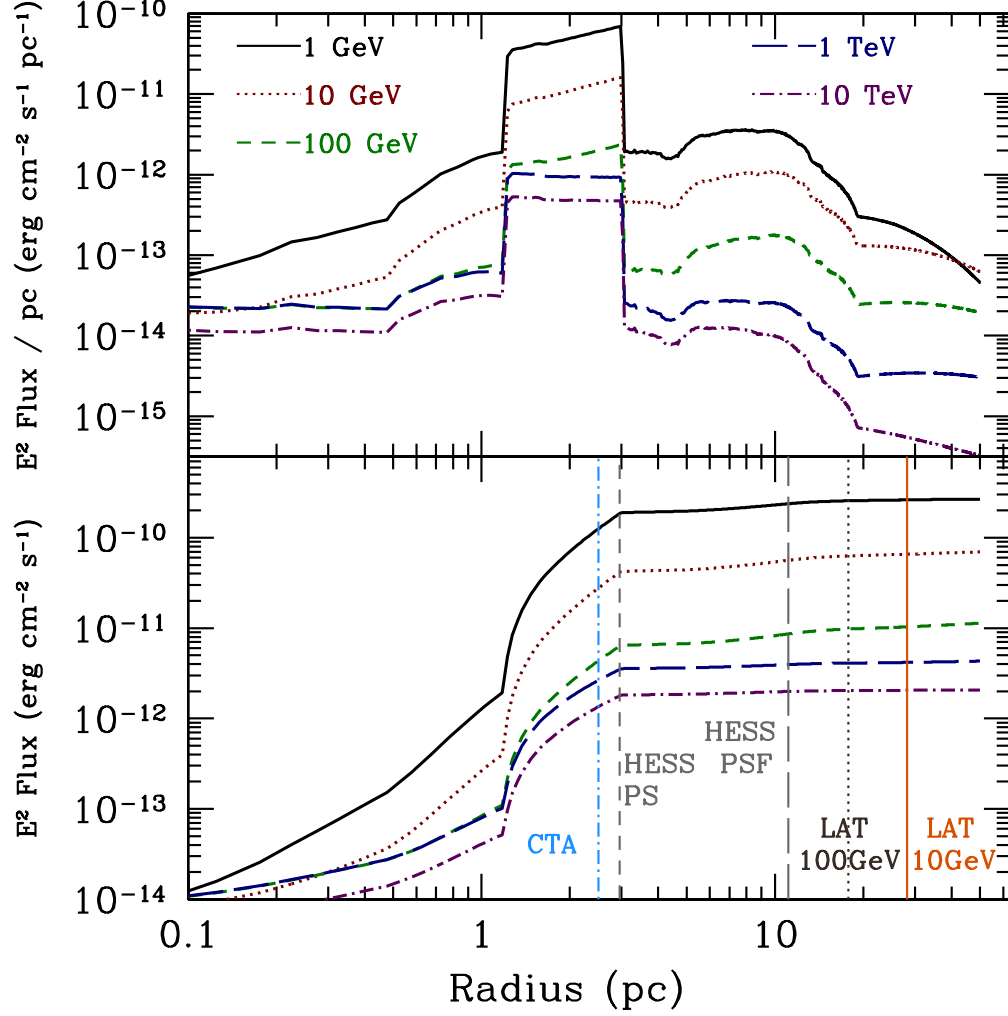
Figure 3.3 Differential (top) and integrated (bottom) radial emission for γ-ray energies of 1 GeV (solid black), 10 GeV (dotted red), 100 GeV (green dashed), 1 TeV (blue long dash) and 10 TeV (purple dot-dashed). In the bottom panel we show vertical lines corresponding to the angular resolution of the Fermi-LAT at 100 GeV (orange solid), Fermi-LAT at 10 GeV (brown dotted), HESS (gray long dashed), CTA (projected, blue dash-dot), as well as the HESS 95% confidence limit on the source extension (HESS PS, gray short dashed).

Chapter 4

Exploring the Nature of the Galactic Center γ-Ray Source with the Cherenkov Telescope Array

Early observations from the High Energy Spectroscopic System (H.E.S.S) opened a new window into γ-ray observations of the Galactic Center (GC) [1] region, including the detection of a bright TeV point source localized to within 1' of the GC. The spectrum of the γ-ray source is fairly hard, following a power-law $\alpha = $ -2.2 +/- 0.09 (stat) +/- 0.15 (sys) with a high-energy cutoff exceeding 10 TeV Aharonian et al. (2004b). Further observations succeeded in localizing the center of the point-source to within 13" of the GC, and found 85% of the total γ-ray emission to be confined within 3 pc (1.2') of the GC Acero et al.

---

[1]Throughout this work, we will employ the term Galactic Center (GC) to refer to both the dynamical center of the Milky Way, as well as to the position of the radio source Sgr A*, which we will consider to be equivalent.

(2010a).

While the observed morphological details strongly suggest that the TeV γ-ray signal stems from a point-source spatially coincident with the black hole at the GC, the steady-state nature of the H.E.S.S. source indicates the emission may be originating farther from the GC. While lower energy X-ray and radio observations have uncovered significant variability from Sgr A* on timescales stretching from minutes to years, no variability has yet been observed in γ-ray observations Aharonian et al. (2009b). Most notably, a simultaneous observation with H.E.S.S. and Chandra found that an X-ray outburst observed in 2007 was not correlated with any change in the γ-ray emission Aharonian et al. (2008b). This implies that the source of the γ-ray emission may be distinct from the source of low-energy photons. Several models have been posited which would naturally explain an intense TeV γ-ray emission which is uncorrelated with the lower-energy regime, including photons from dark matter annihilation Hooper et al. (2004b); Profumo (2005); Aharonian et al. (2006c), as well as π^0-decay resulting from the emission of high energy protons from the central black hole and their subsequent collisions with Galactic gas Aharonian & Neronov (2005c); Liu et al. (2006b,d); Fryer et al. (2007); Ballantyne et al. (2007b).

With the launch of the Fermi-LAT in 2008, the window was opened to observe the GeV γ-ray spectrum with similar angular and energy resolution to that of H.E.S.S. Atwood et al. (2009), unveiling a distinctly different spectral shape from the very high-energy regime. Specifically, an excess of 1-10 GeV γ-rays was uncovered in the GC compared to that expected from an extrapolation of the TeV source spectrum to GeV energies Vitale et al. (2009b); Hooper & Goodenough (2011b); Hooper & Linden (2011c); Hooper et al.

(2012b). Several models have been postulated to explain this excess emission, including the annihilation of light, leptophilic dark matter particles Hooper & Goodenough (2011b); Hooper & Linden (2011c) and emission from millisecond pulsars Abazajian (2011b). Recently, Chernyakova et al. (2011) re-examined an extension of the hadronic scenario described above down to GeV energies and found that the entirety of the GeV-TeV spectrum could be explained by inelastic processes initiated by protons whose spectrum would follow a single power-law. The softening of the γ-ray signal at energies $\sim$10-100 GeV was then enforced by fine-tuning the diffusion constant in order to produce diffusive propagation at GeV energies and rectilinear propagation at TeV energies.

Subsequently, Linden et al. (2012) examined the expected morphology of the hadronic emission model described by Chernyakova et al. (2011), using a realistic model for the morphology of Galactic gas in the inner 10 pc around Sgr A* as determined by Ferrière (2012). They found that the morphology of TeV emission closely matched observations byAharonian et al. (2006c) signaling that 85% of the γ-ray emission from the GC was confined to within $\sim$3 pc of Sgr A*. Additionally, Linden et al. (2012) found that the energy dependence of this morphology is minimal, and thus the majority of GeV emission detectable by the Fermi-LAT should also reside within 3 pc of the central black hole, which may be in tension with an observed extension of the GeV γ-ray source at the GC Hooper & Goodenough (2011b); Hooper & Linden (2011c). We note that disentangling an extended emission in this region is especially problematic, given the poor knowledge of the diffuse Galactic emission Vitale et al. (2009b). Finally, Linden et al. (2012) noted that while the hadronic emission model should appear point-like to all current γ-ray instruments, the up-

coming Cherenkov Telescope Array (CTA), should observe an extended spatial morphology which would distinguish this scenario from other point-source emission mechanism occurring at the position of Sgr A*.

In this *letter*, we closely investigate several models for the TeV γ-ray emission at the GC which may be observed by CTA, including a γ-ray point source at the position of Sgr A*, p-p collisions due to hadronic emission from the position of Sgr A* Chernyakova et al. (2011); Linden et al. (2012), and dark matter Hooper et al. (2004b); Profumo (2005); Aharonian et al. (2006c). Specifically, we show that the improved angular resolution of CTA can differentiate these scenarios with surprising accuracy based on morphology alone, allowing for the construction of a rigorous model for the γ-ray emission from the GC center source. In turn, the resulting morphology observed by CTA will stand as a crucial ingredient in the understanding of high-energy emission from the entire GC region, including possibly the extraction of a dark matter annihilation signal.

4.1 Models

The morphology of the γ-ray emission from π^0 decay is dominated by the distribution of Galactic gas. In order to produce a rigorous model which takes into account the full 3D morphology of the target gas density, we employ the maps of Ferrière (2012) which include not only contributions from a spherical diffuse halo, but also from structures associated with the SNR Sgr A East, from belts of molecular clouds, and most importantly, from the high-density gaseous disk known as the circum-nuclear ring. This ring-shaped cloud of gas is located between 1-3 pc from the GC, inclined $20°$ with respect to the Galactic

plane, and contains gas densities approximately two orders of magnitude larger than in the surrounding GC medium Becklin et al. (1982b); Bradford et al. (2005). In this work, we assume the central position and gas density for each gas structure, and set the volume filling factor of each structure to match those provided in Table 1 of Ferrière (2012). Given the high energy of the injected protons in γ-ray models, we ignore all information on the temperature distribution of Galactic gas, as it is inconsequential for γ-ray production.

In their analysis of the combined GeV and TeV spectrum, recent work by both Chernyakova et al. (2011) and Linden et al. (2012) employed a diffusion constant tuned in order to provide a sharp transition between diffusive propagation in the GeV energy regime and rectilinear transport at TeV energies. This transition, which occurs at diffusion constants of approximately 1.4 x 10^{29} cm^{2}s^{-1} for a diffusion zone of 10 pc, must be finely set in order to correctly explain the extremely soft emission spectrum at energies of approximately 100-500 GeV. Thus, a generic prediction of all scenarios which employ a single proton injection spectrum to correctly match both the GeV and TeV γ-ray emission spectrum, is cosmic ray propagation which is transitioning from the diffusive to the rectilinear regime at TeV energies. In the rectilinear regime, the cosmic-ray density falls as r^{-2}, while in the diffusive regime the cosmic-ray density falls instead as r^{-1}, due to the square dependence of the escape time on the size of the diffusion region.

In either case, we will assume that cosmic ray protons in this energy range tend to interact with gas less than one time before leaving the diffusion region, validating the assumption that the energy spectrum of cosmic ray protons is position independent. For the gas density maps provided by Ferrière (2012) this assumption holds so long as the average

value of the diffusion constant in the inner 10 pc of the galaxy exceeds 1.8×10^{27} cm^2 s^{-1}. Under this restriction, coupled with the assumption that the γ-ray emission from the galactic center is in steady state, our models for the morphology of the γ-ray emission depend only on the radial density of cosmic-ray protons, rather than the exact diffusion scenario which produces the proton morphology.

Throughout this work, we will calculate the expected γ-ray morphology for both the diffusive and rectilinear models of proton-propagation, finding that the qualitative arguments presented throughout this paper do not depend on the exact diffusion model considered. Furthermore, we can consider these two scenarios to bound the distributions expected for relativistic particle motion due to interactions with magneto-hydrodynamic waves, and can also be used as approximations of the expected effect in scenarios involving either non-homogenous diffusion scenarios such as those put forth by Fryer et al. (2007) and Ballantyne et al. (2007b).

Finally, a significant uncertainty in this model pertains to the angular dependence of cosmic-ray injection from the GC point source: while a spherically symmetric distribution was found by Linden et al. (2012) to provide a compelling match to the current H.E.S.S. point source limit on the GC emission, other models are possible. We will comment on the assumption of isotropy in the cosmic ray distribution in Section 4.3. Throughout this work, we restrict our analysis to examining photons in the energy range of 1-10 TeV, which yields several simplifications to the analysis. First, the spectrum in this region is relatively flat, following a best fit spectral index $\Gamma = 2.10 \pm 0.04$ Aharonian et al. (2009b). Secondly, the PSF of both H.E.S.S. and CTA are relatively constant in this region Aharonian et al.

(2006e); CTA Consortium (2011).

The most up-to-date analysis of the GC with H.E.S.S. consisted of 93h of live-time with the instrument operating in "Wobble" mode with a an average distance of $0°.7$ from the position of Sgr A*, and producing events with a mean zenith angle of $23°$ Aharonian et al. (2009b). From (Aharonian et al., 2006d, Fig. 13) we infer an effective area of 2 x 10^9 cm^2, with only negligible variation over the energy range 1-10 TeV. In this region, we adopt a point-spread function which is constant in energy and follows the functional form given in Aharonian et al. (2006d) of a two-component Gaussian where the probability of finding a photon in a radial bin dθ is given by:

$$P(\theta) = A\theta(\exp(-\frac{\theta^2}{2\sigma_1^2}) + A_{\text{rel}}\exp(-\frac{\theta^2}{2\sigma_2^2})) \tag{4.1}$$

with $\sigma_1 = 0.046$, $\sigma_2 = 0.12$, $A_{rel} = 0.15$ and A a normalization constant. However, in this work, these parameters are set specifically to account for the spectral characteristics of the Crab Pulsar and a $60°$ zenith angle. These parameters provide a 68% containment angle of $0.12°$ degrees. In the case of the GC, Aharonian et al. (2006e) yields a 68% containment angle of $0.08°$, and we thus linearly scale down the parameters θ_1 and θ_2 to the values $\theta_1 = 0.031$ and $\theta_2 = 0.08$ in order to obtain the correct 68% containment angle. Finally, H.E.S.S. observations from Aharonian et al. (2009b) find a best fit intensity above 1 TeV of $I_{>1TeV} = (1.99 \pm 0.09)$ x 10^{-12} cm^{-2} s^{-1}. Given the calculated effective area of H.E.S.S, this implies a point source observation of 1332 photons with energy in the range 1-10 TeV.

In order to model the instrumental performance of CTA, we adopt best fitting

parameters following the design specifications set forth in CTA Consortium (2011), noting, however, that the ultimate design specifications for the instrument are presently unknown. Specifically, we adopt an effective area in the 1-10 TeV band of 2×10^{10} cm^2, which exceeds the H.E.S.S. effective area by an order of magnitude, and we adopt an equivalent functional form for the point-spread function as described in Eq. (4.1) for H.E.S.S., but rescale the parameters σ_1 and σ_2 such that the 68% containment radius of the photon signal is 0.03°. This yields $\sigma_1 = 0.0115$ and $\sigma_2 = 0.03$. While CTA contains additional improvements over current Cherenkov telescopes, especially stemming from its significantly lower energy threshold, the poorer angular resolution in the lower energy regime mitigates the effectiveness of CTA to test the morphology of the dense GC region. In this work we evaluate the performance of CTA after both 100 and 500 hours of observation, indicating both a conservative lower bound and a targeted observation time for the GC region. This yields an expected 14323 and 71613 photon counts, respectively.

In order to simulate observations of the GC with both the H.E.S.S. and CTA instruments we employ Monte Carlo techniques to calculate the expected distribution of observed photons. We first calculate the 3D morphology for the true photon direction. In the case of hadronic emission, we calculate this by multiplying the 3D distribution of gas with both the r^{-2} and r^{-1} cosmic-ray densities assumed for rectilinear and diffusive transport of TeV protons. For dark matter models we assume a density distribution $\rho(r) = r^\alpha$ and evaluate scenarios $\alpha=\{1.0, 1.4\}$, as we note that current hydrodynamical simulations indicate the possibility that the inner dark matter density profile is adiabatically contracted (i.e. $\alpha > 1.0$) Blumenthal et al. (1986b); Ryden & Gunn (1987b); Gnedin et al. (2004b,

2011b). These emission profiles are integrated over the line of sight, and then photons are selected from this distribution and smeared with the PSF of each instrument. We run 1000 simulations of all models in order to achieve reasonable statistical accuracy, unless otherwise noted.

4.2   Results

In Figure 4.1 we show γ-ray intensity maps depicting the actual emission morphology (i.e. for a machine with perfect angular resolution) (top row), the emission as observed by a machine with the angular resolution of the HESS telescope (middle row) and the emission as observed by a machine with the angular resolution of CTA (bottom row) in the case of hadronic emission in the regime rectilinear proton propagation (left column), hadronic emission in the regime of diffusive proton propagation (middle column), and point source emission. In models employing the effective area and angular resolution of the H.E.S.S. telescope, the morphological features stemming from the gas density employed in the hadronic emission scenario occur on angular scales significantly smaller than the $\sigma = 0.08°$ angular resolution of the telescope blurring out the angular features which distinguish the hadronic scenario. Since these angular features are themselves centered around the position of Sgr A*, differentiating between the point-source and hadronic models becomes extremely difficult.

Calculating the average cumulative-distribution function over 1000 simulations of both a GC point source and the hadronic emission scenario, we employ a K-S test and find that current H.E.S.S. results would only be able to differentiate between models with a $\chi^2/\text{d.o.f.} = 0.85$, which falls far short of providing a minimum 2σ level of confidence between

the emission profiles. In Figure 4.2 (top left) we provide a binned (at $0.01°$) sample of photons collected by the H.E.S.S. telescope in each scenario. In realistic observations, this result is further complicated by residuals stemming from both the Galactic plane integrated over the line of sight, as well as from contaminating cosmic-ray backgrounds, both of which should appear isotropic in the small region under consideration. While additional H.E.S.S. observations time may slightly improve these statistics, these additional backgrounds make it unlikely that the H.E.S.S. telescope will be capable of differentiating between the point source and hadronic emission scenarios.

In the case of CTA, the improved angular resolution will provide a much sharper view to distinguish between a point source and hadronic models. Furthermore, the greatly increased effective area will (in our simplified model where additional backgrounds are rejected) increase the χ^2 mismatch between models linearly. Using 100 hours of CTA observation, a K-S test provides a fit $\chi^2/\text{dof} = 208$, which provides more than 14σ differentiation between models. We find that the improved angular resolution of CTA will allow for a 3σ rejection of the poorer fitting model with only $\sim$5h of pointed observation! In Figure 4.2 (top right), we again show a binned analysis for this dataset, noting specifically the under-density of photons observed within the inner $0.01°$, which provides an independent, statistically significant indication that would be difficult to explain with an additional diffuse or cosmic-ray background. We note that over the projected lifetime of CTA, nearly 500h of GC observation are expected, which would lead to a 32σ differentiation between models, with a result that is plotted in Figure 4.2 (bottom right). A wealth of information on the nature of the GC source will clearly be available in this case, going well beyond

simply distinguishing between a point-source emission and a hadronic model.

In Figure 4.3 we show the same observations as in Figure 4.2, but under the assumption that high energy protons travel diffusively through the inner galaxy, and thus follow a density distribution $\rho(\text{r}) \propto \text{r}^{-1}$ instead of $\rho(\text{r}) \propto \text{r}^{-2}$. In this case, we find that the statistical differentiation between the Point Source and Hadronic scenarios slightly increases in all cases, due to the more diffuse nature of the energetic protons. However, the qualitative results are unchanged. Specifically, in the case of H.E.S.S observations this improvement is still insufficient to differentiate the two signals, as our K-S test obtains a fit $\chi^2/\text{dof} = 1.49$.

In realistic models, additional emission sources must also be considered, including an isotropic cosmic-ray background, a line of sight background through the Galactic plane[2], and unresolved sources in the region surrounding the GC – all of which will contribute additional uncertainties to the differentiation of the point source and hadronic models. One particularly interesting background could stem from the annihilation of dark matter particles in the GC region. The morphology of the dark matter annihilation is partially constrained to be spherically symmetric with a density distribution which follows a form $\rho(\text{r}) \propto \text{r}^{-\alpha}$. While a standard value, $\alpha = 1.0$ is employed in the standard NFW dark matter model Navarro et al. (1997), the dark matter profile is highly uncertain in the GC region, and the gravitational effect from baryons in the GC may significantly steepen the dark matter distribution Blumenthal et al. (1986b); Ryden & Gunn (1987b); Gnedin et al. (2004b, 2011b). This makes it potentially difficult to differentiate between dark matter models for TeV emission from the GC, and the possible combination of emission from both point source and hadronic sources.

---

[2]We note that this is approximately isotropic for the very small angular regions considered here.

In Figure 4.4 we plot a projection for the cumulative distribution function of photons observed with 500h at CTA as a function of the angular distance from the GC, for models of point source emission, hadronic emission, dark matter annihilation with a density profile $\alpha = 1.0$ and with a density profile $\alpha = 1.4$. We note that the point source model contains the fastest rising CDF possible, with a morphology uniquely determined by the instrumental PSF. Any combination of emission from a point source and the hadronic model must produce a CDF which lies between the individual models, and the relative contribution of each source class can be accurately (to within $\sim 10\%$ errors after 500h of observation) determined by examining the CDF observed by CTA. However, a small contribution from dark matter annihilation following an index $\alpha = 1.0$ along with a dominant contribution from the point-source, may be misinterpreted as emission stemming from important contributions of both the point-source and hadronic models. Moreover, models where the emission is entirely dominated by dark matter which is highly peaked towards the GC (such as $\alpha = 1.4$), may also be misinterpreted as some linear combination of hadronic and point source contributions. This uncertainty is a standard result from an attempt to identify three unknown intensities using only one constraint parameter.

A separate measurement is therefore necessary in order to constrain the relative contributions from all three source classes. An obvious choice is to model the angular distribution of photons around the GC, noting that both the point source and dark matter models are spherically symmetric. In Figure 4.5 we plot the expected azimuthal angular distribution for both the point source and hadronic models, counting the number of photons from a given angle $\phi = \arctan(b/l)$, i.e. the angle formed between the Galactic plane and

the direction joining the GC and the photon location in the sky (see inset). We restrict the counts to photons within 0.05° of the GC, where contributions from the H.E.S.S. point source are believed to be largely dominant. While a (spherically symmetric) point source provides a flat distribution in the incoming photon angle (as expected), contributions from the hadronic scenario deviate significantly, and are primarily aligned with the Galactic plane, due to contributions from both the circum-nuclear ring, as well as a contribution at angles of near 0° from hadronic interactions within the molecular cloud M-0.02-0.07. We note that with 500h of observation, an evaluation of the nature of the central TeV source can be made with more than 11σ confidence - without any reference to the radial distribution shown in Figure 4.2. Most importantly, this implies that in cases where the point-source, hadronic sources, and dark matter annihilation all contribute non-negligibly to the total TeV galactic center source, we can determine the relative contribution stemming from hadronic emission to within 20% with more than 2σ confidence. In Figure 4.6 we show the same analysis as in Figure 4.5, under the assumption of diffusively propagating protons and find the results to be qualitatively unchanged, with a $\chi^2/$dof which improves by about 25%.

4.3   Discussion and Conclusions

We have shown that while current TeV instruments are incapable of distinguishing between point-source and hadronic emission models for the GC, the upcoming CTA will definitively differentiate between the signals within its first hours of observation at the GC, and will determine the relative importance of each contributing source class at the 10% level over the course of its lifetime (see Fig. 4.2 and related discussion). These source

classes can be distinguished based on either their radial or angular morphology, yielding two independent handles for the determination of the γ-ray source. The angular information is particularly important, as it allows the hadronic scenario to be easily separated from *any* combination of a GC point source and models of dark matter annihilation.

While in this work, we have considered only γ-rays with an energy exceeding 1 TeV in our quantitative evaluation of the ability of CTA to distinguish between the hadronic and point-source signals, we note that the discrimination power of CTA could be further extended depending on the specific instrumental point spread function which the instrument attains at lower energies. The continuation, or even softening of the $E^{-2.0}$ γ-ray spectrum to energies as low as 1 GeV has been demonstrated by the combination of HESS Aharonian et al. (2009b) and Fermi-LAT Vitale et al. (2009b); Hooper & Goodenough (2011b); Hooper & Linden (2011c) results. This has the potential to create a much stronger statistical test, so long as the angular resolution of CTA remains on the same scale as the size of the circum-nuclear ring. Moreover, the differentiation between the Hadronic and point-source models improves in the diffusive regime, which is thought to control the propagation of the protons which create the γ-ray signal below $\sim$100 GeV Chernyakova et al. (2011); Linden et al. (2012).

We further note that while this study quantitatively examines only one specific scenario for hadronic diffusion through the GC region where the diffusion constant was fine tuned in order to match the softening of the γ-ray spectrum at energies $\sim$100 GeV Chernyakova et al. (2011), the model remains relevant for other physical models which have been proposed to control the propagation of high energy protons in the galactic center region. Specifically,

Fryer et al. (2007) employs a model which allows rectilinear propagation out to approximately 1 pc, after which the shocked winds produce a proton density which remains relatively flat between 1-3 pc, corresponding with the region dominated by the circum-nuclear ring. The comparison of our results in the case of both rectilinear ($\rho(\mathrm{r}) \propto \mathrm{r}^{-2}$) and diffusive ($\rho(\mathrm{r}) \propto \mathrm{r}^{-1}$) propagation show that the overall change in the pion production morphology is relatively unchanged by this factor of 3 change in the proton density at the outer edge of the circum-nuclear ring. In fact, from our results, we would expect a marginal improvement in the differentiation between the model of Fryer et al. (2007) and that of point-source γ-ray production. The same is also true in the models of Ballantyne et al. (2007b), where the diffusion constant varies inversely with the local gas density, producing a density of cosmic-rays which increases greatly in the region of the circum-nuclear ring.

There is however, one important caveat to the scenario employed here. The morphology of observed high energy gamma rays from the Hadronic scenario may become significantly less extended in cases where high energy protons are not isotropized by the galactic medium through which they are propagating. In this case, γ-rays observed at the solar position will preferentially stem from protons which were themselves originally pointed towards the solar position, due to the relativistic beaming of pions produced in p-p scattering. This complication may become important in scenarios where we have assumed rectilinear proton propagation, which in the case of a simple, homogeneous diffusion constant, would imply that protons do not become completely isotropized before leaving the diffusion zone. In this scenario, we find that for diffusion constants exceeding 9.3×10^{29} cm^2 s^{-1}, the random walk approximation for particle diffusion predicts that the average proton will not

undergo a change in direction before leaving the 10 pc diffusion region. In the studies of Chernyakova et al. (2011) and Linden et al. (2012) this corresponds to a proton energy of only 2.2 TeV. It is these protons which dominate the 1 TeV signal, since the E^{-2} proton injection signal implies that the most important contributor to γ-rays of a given energy are protons of a very similar energy. This could mean that some fraction of protons which are undergoing p-p scattering in our simulations are not isotropically distributed.

However, the random-walk approximation for proton diffusion is notably poor in this region, and all protons will undergo some scattering off of the magnetic field inhomogenities in the diffusion region. The exact degree of proton anisotropy will depend sensitively on the specifics of this diffusion scenario, and specifically on any inhomogenities in the magnetic field structure, which are both invariably present, and difficult to directly determine. Lastly, we note that even if the vast majority of the signal is anisotropic (thus appearing very similar to the point source calculation), even a small isotropic component could be distinguished from the point source calculation, given the incredible χ^2 detection of the Hadronic model by the CTA.

We note that this same process could also place constraints on the dark matter annihilation cross-section - using the observed angular and radial profiles to determine the maximum contribution of photons following a morphology consistent with dark matter annihilation. However, due to the small angular region considered, as well as the extremely bright point-source emission observed by H.E.S.S., these constraints are not competitive with those determined, for example, by H.E.S.S. observations of the regions directly above and below the Galactic plane Abramowski et al. (2011). While the GC remains an extremely

interesting region for setting dark matter constraints with CTA, the best limits will likely continue to be set by analysis of regions directly off of the Galactic plane. This scenario may become interesting, however, in cases where the dark matter density in the GC region is found to be *highly* adiabatically contracted (e.g. $\alpha >\sim 1.7$), leading to extremely enhanced fluxes within the inner pc of the Galaxy.

Pinpointing the nature of the GC source will allow us to more effectively search for a dark matter signal in this region, as the differentiation between the point source and hadronic models would allow for an extrapolation of their expected emission profiles into the regions where strong dark matter limits can be set. Additionally, the extrapolation of the observed CTA emission will greatly refine Fermi-LAT models of the morphology of the central point source, as shown in Linden et al. (2012). Thus TeV γ-ray observations will be critical to validate or constrain particle dark matter models that could explain other observations tentatively indicating signals from dark matter annihilation at lower energies (e.g Hooper (2012)). In this scenario, CTA will be highly complementary to an extended Fermi-LAT campaign, and will place strong limits on the spectrum of the central point source.
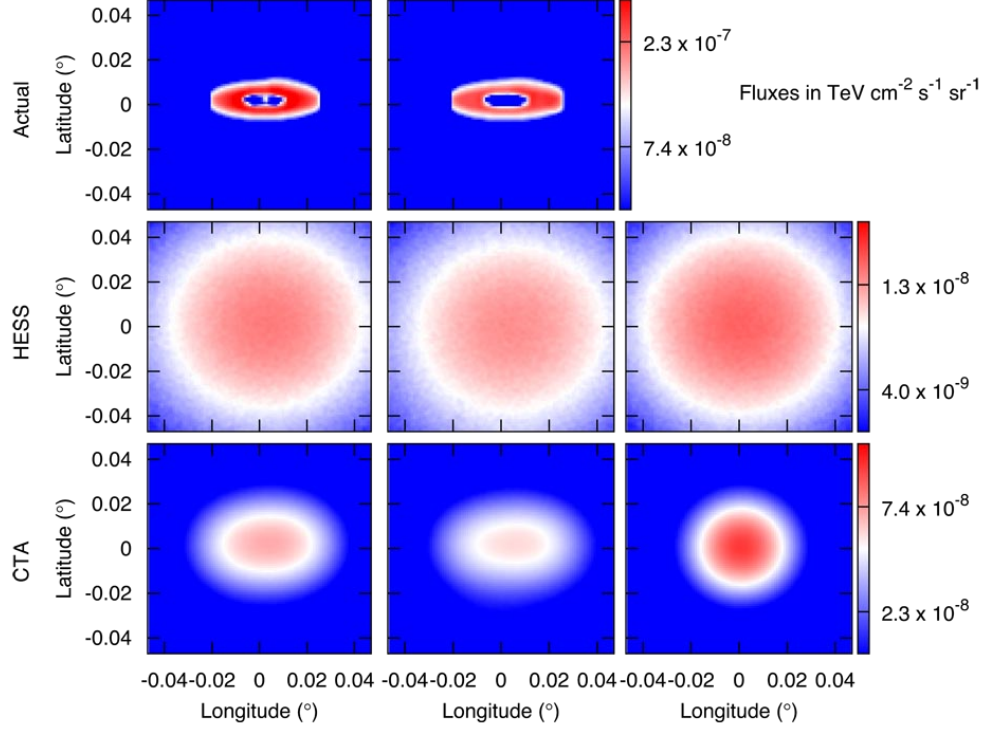
Figure 4.1 Observed flux at the solar position as a function of the angle from the galactic center from the actual emission morphology (i.e. for a machine with a perfect angular resolution, top row), the emission as observed by an instrument with the angular resolution of the HESS telescope (middle row) and for an instrument with the angular resolution of the CTA telescope (bottom row) in the case of hadronic emission in the regime rectilinear proton propagation (left column), hadronic emission in the regime of diffusive proton propagation (middle column), and point source emission. The fluxes are shown logarithmically and binned to regions of $10^{-4\circ}$. The pointsource emission for an instrument with perfect angular resolution is not shown, as it would would provide a delta function at the center of the image. The flux shown stands as the flux between 1-10 TeV in energy averaged over 10000 realizations of 93 hour HESS observations and 1000 realizations of 500 hour CTA observations.
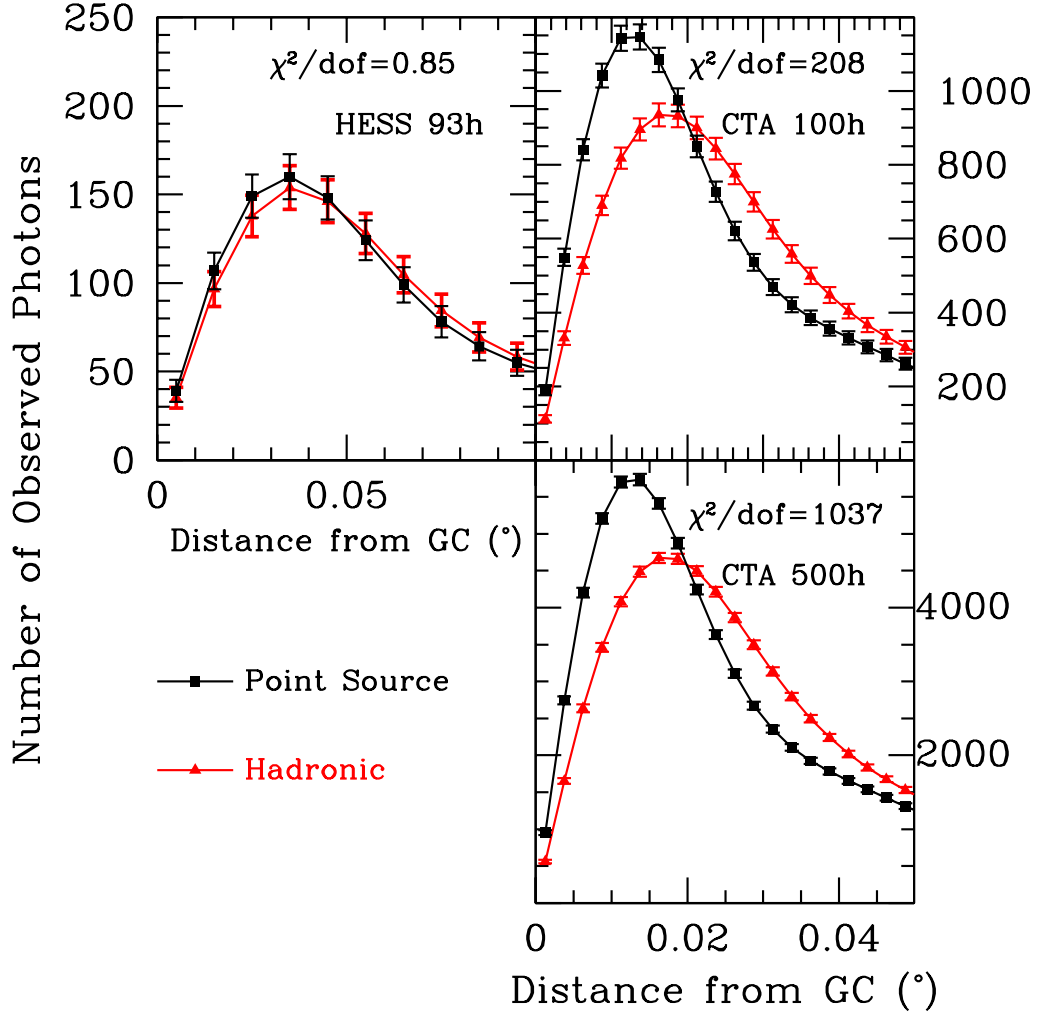
Figure 4.2 Expected photon counts as a function of the distance from the GC (° from Sgr A*), for models where the 1-10 TeV signal is generated by photons from a point source at the position of Sgr A* (black) or via hadronic emission from the central point source which propagates rectilinearly ($\rho(r) \propto r^{-2}$) and subsequently interacts with gas (red). The mean shown in each model is the average of 1000 realizations, and error bars indicate the $\sqrt{counts}$ for a the average simulation. The value of χ^2/d.o.f is computed via a two-sample K-S test which does not depend on the binning used in the figure.

Figure 4.3 Same as Figure 4.2 but for protons which are propagating diffusively ($\rho(r) \propto r^{-1}$) (red)
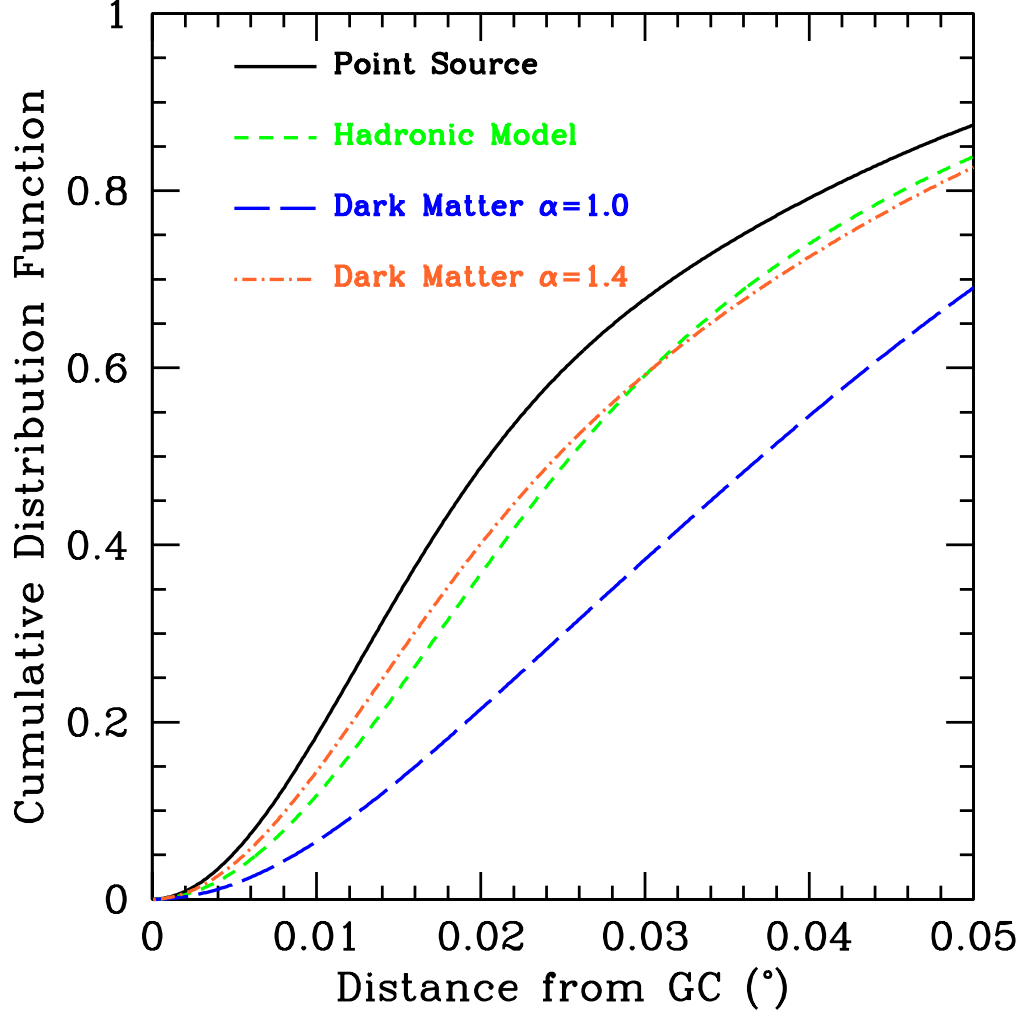
Figure 4.4 Cumulative Distribution Function (CDF) of photons observed within 0.05° of the GC for models of the total number of photons produced within ∼0.07° of the GC. We show the case of a point source at the position of the GC (solid black), the hadronic model as described in Section 4.1 (green short dash), dark matter following an NFW profile $\alpha = 1.0$ (blue long dash) and dark matter following a steeper profile with $\alpha = 1.4$ (orange dot-dashed).
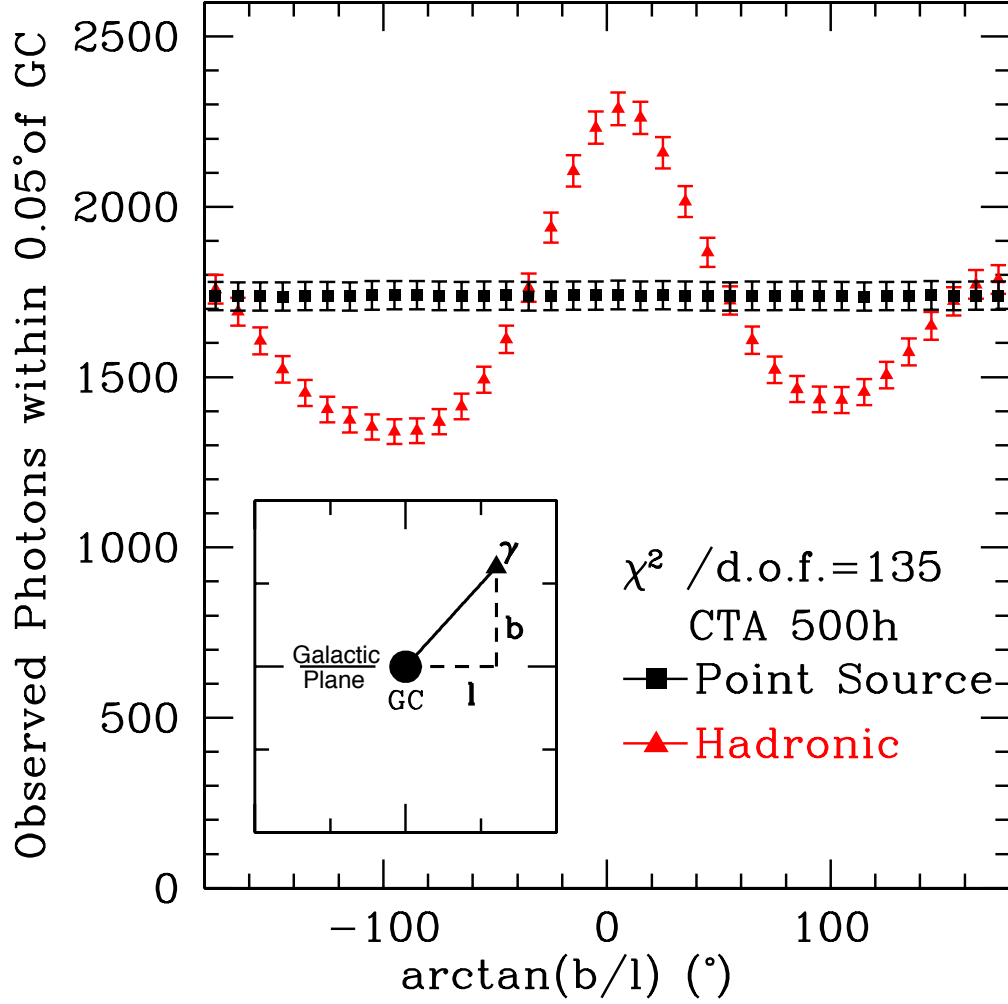
Figure 4.5 Expected photon counts as a function of the azimuthal angle $\phi = \arctan(b/l)$ (shown in the inset), for both the point-source (black squares) and the hadronic emission scenario for protons which propagate rectilinearly (red triangles) for photons observed within $0.05°$ of the GC. In the case of a point source, photons are symmetrically distributed around the position of the GC, while the majority of emission due to hadronic injection follows the distribution of gas, which is aligned more closely with the Galactic plane.
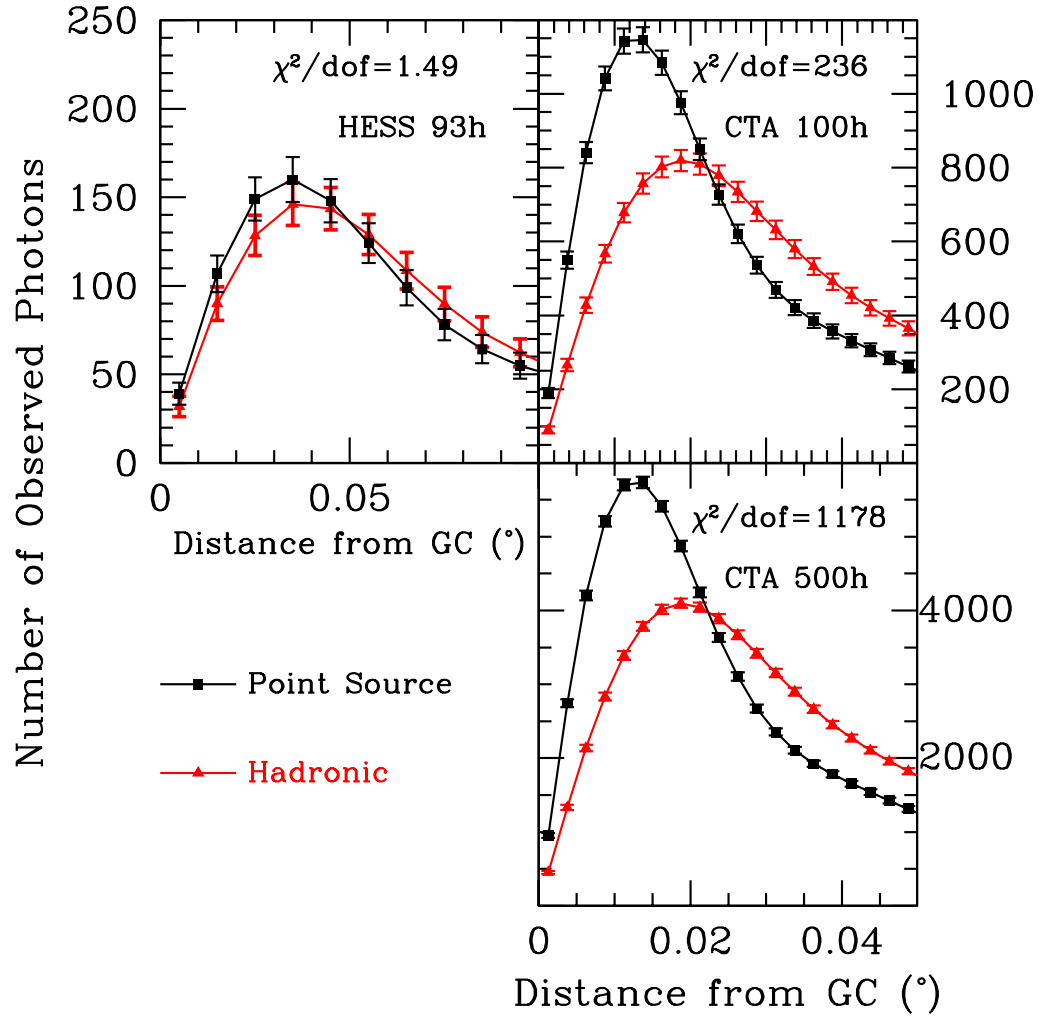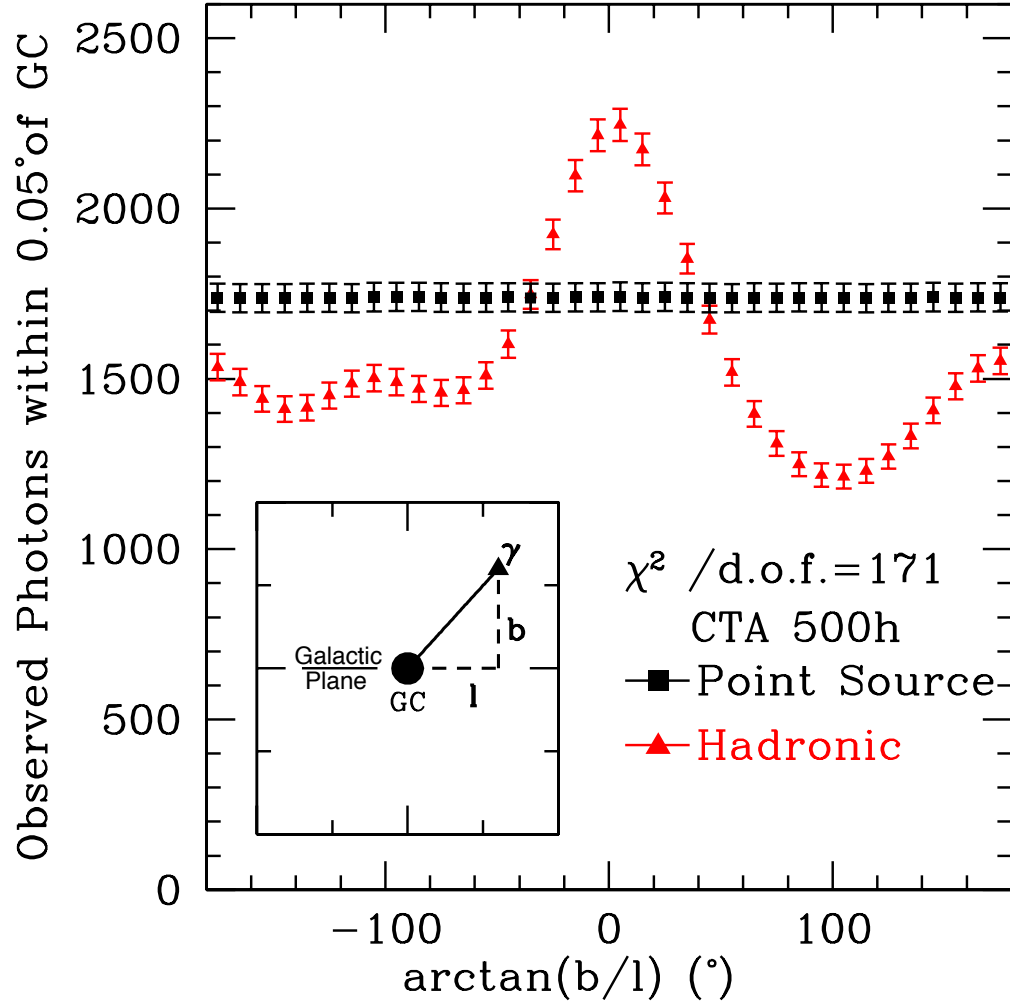
Figure 4.6 Same as Figure 4.5 but for protons which are propagating diffusively ($\rho(r) \propto r^{-1}$) (red)

Chapter 5

# Dark Matter and Synchrotron

Emission from Galactic Center

Radio Filaments

Weakly Interacting Massive Particles (WIMPs) provide an attractive class of candidates for the dark matter of our universe Bertone et al. (2005); Bergström (2009). The WIMP paradigm is motivated in part by the realization that particles with weak-scale interactions and masses will naturally freeze-out in the early universe with a relic abundance similar to the observed density of dark matter Steigman (1979b), an observation referred to as the "WIMP Miracle". Barring any complicating factors such as conannihilations, resonances, or S-wave suppression, dark matter candidates motivated by the WIMP miracle annihilate with a cross section of approximately $\sigma v \approx 3 \times 10^{-26}$ cm^3 s^{-1} (where v is the relative velocity of the annihilating WIMPs). These annihilations produce stable particles,

including photons at γ-ray energies, as well as protons, electrons, neutrinos, and their antiparticles. Because the dark matter annihilation rate scales with the square of the dark matter density, regions such as the Galactic center, dwarf spheroidal galaxies, and galaxy clusters represent promising locations for searches for indirect signatures of dark matter.

The launch of the Fermi Large Area Telescope (Fermi-LAT) in 2008 has greatly expanded our view of the γ-ray sky Atwood et al. (2009). In addition to its significantly enhanced effective area, the unparalleled spatial and energy resolution of the Fermi-LAT has allowed for the separation of point sources in the Galactic center, revealing much more detailed information about the diffuse γ-ray emission from this region Abdo et al. (2009a); Vitale et al. (2009c). Recently, Hooper & Goodenough (2011c) identified an excess of γ-rays within approximately 175 pc of the Galactic center in the energy range of $\sim$500 MeV to 7 GeV, and showed that this could be explained by 7-10 GeV dark matter particles annihilating into $\tau^+\tau^-$ pairs, possibly among other leptonic final states. This range of dark matter masses also provides a suitable match to the direct detection signals observed by the DAMA/LIBRA Bernabei et al. (2010b); Hooper et al. (2010) and CoGeNT collaborations Aalseth et al. (2011c,b); Hooper & Kelso (2011). While upcoming limits from CMB constraints Slatyer et al. (2009); Hütsi et al. (2011) as well as LEP constraints Fox et al. (2011), error bars in these measurements, along with uncertainties in the dark matter density both locally and near the galactic center, are more than sufficient to remedy any tension between these models.

If annihilating dark matter particles are in fact responsible for the flux of γ-rays observed from the Galactic center, this signal is guaranteed to be accompanied by the

production of a hard population of electrons and positrons carrying a significant percentage of the total annihilation energy. In the case of democratic annihilation (equal number of annihilations to each family of charged leptons: e^+e^-, $\mu^+\mu^-$, and $\tau^+\tau^-$), the combined electrons and positrons carry away nearly an order of magnitude more energy than the γ-rays observable by the Fermi-LAT (8.4 GeV per annihilation, as compared to 1.1 GeV into γ-rays for a 8 GeV WIMP). For this reason, the synchrotron radiation from the electrons and positrons produced in dark matter annihilations provides a particularly promising test of the dark matter interpretation of the γ-ray flux from the Galactic center. Along these lines, it has been shown that the characteristics of the galactic synchrotron excess known as the WMAP Haze are consistent with scenarios in which annihilating dark matter is the source of the observed Galactic center γ-rays Hooper & Linden (2011b).

In addition to the high dark matter density expected in the Galactic center Navarro et al. (1996b), galactic studies of dark matter synchrotron are enticing due to the many survey observations undertaken over several decades. Observations at 74 MHz Brogan et al. (2003), 330 MHz Pedlar et al. (1989); Anantharamaiah et al. (1991); LaRosa et al. (2000b); Nord et al. (2004), 1.4 GHz Yusef-Zadeh et al. (2004), 5 GHz LaRosa et al. (2004) and higher frequencies Sofue et al. (1986); Reich et al. (2000) allow for the additional modeling of spectral features, in addition to the spatial characteristics, of radio sources. A particularly interesting probe for synchrotron signals of dark matter annihilation concerns the population of long ($\sim$40 pc) and thin ($\sim$1 pc) filamentary structures located between 10 and 200 pc from the Galactic center, which have been identified at radio wavelengths Yusef-Zadeh et al. (1984). These structures, known as non-thermal radio filaments (NRFs), are characterized

primarily by their extremely hard radio spectra, with a spectral index α between -0.5 and +0.3 (where $S_\nu \sim \nu^\alpha$), as well as their preferential alignment perpendicular to the Galactic Plane. In several notable cases such as the Radio Arc, high resolution surveys have found a tangled network of separate NRFs which contribute to the overall emission in the structure Yusef-Zadeh et al. (1984). The radio emission from these filaments is highly polarized, implying that the radio sources are powered by synchrotron emission in a highly ordered poloidal magnetic field of strength $\sim$100 μG Tsuboi et al. (1986).

While several dynamical mechanisms have been proposed to explain the comparatively strong magnetic fields found in NRFs relative to the large scale Galactic magnetic field Rosner & Bodo (1996); Boldyrev & Yusef-Zadeh (2006), the hard synchrotron spectrum observed from NRFs presents a more difficult puzzle. The observed synchrotron spectral index, α, stemming from a power-law electron injection spectrum with index p can be modeled as $p = 2\alpha - 1$, where p is the power law index of the electron injection spectrum and α is the power law index of the output synchrotron spectrum. Thus, the p $\sim$ -2.4 spectrum observed to result from astrophysical shock acceleration Blandford & Eichler (1987); Jones & Ellison (1991); Malkov & O'C Drury (2001) would be expected to yield a spectrum of synchrotron emission softer than $\alpha \sim$ -0.7, which is significantly softer than observations of NRFs such as G0.2-0.0, commonly known as the Radio Arc. Lesch et al. (1988) modeled the observed synchrotron spectrum of the Radio Arc, finding the synchrotron spectrum to be best fit by an essentially monoenergetic electron spectrum at approximately 7 GeV. Further observations have found a $\sim$10 GHz turnover in the synchrotron spectrum of many NRFs, implying a strongly peaked electron energy spectrum at several GeV propagating in

a magnetic field on the order of 100 μG Boldyrev & Yusef-Zadeh (2006).

Several mechanisms have been proposed to explain the origin of such a highly peaked electron spectrum in NRFs. Most notably, Lesch & Reich (1992), and later Lieb et al. (2004), advocated a pile-up scenario in which magnetic reconnection zones formed in collisions between NRFs and molecular clouds create electrical potentials which can accelerate electrons to a single energy specified by the relative strength of the electromagnetic potential and the synchrotron energy loss rate. This explanation, however, is problematic for three reasons: (1) not all bright NRFs have observed molecular cloud associations Lang et al. (1999a); Law & Yusef-Zadeh (2004), (2) recent simulations of collisional reconnection regimes imply a maximum electron energy of less than 10 MeV, several orders of magnitude below that needed to explain the observed synchrotron signal Lyubarsky (2005); Zanotti & Dumbser (2011), although collisionless reconnection, already proposed in the case of γ-ray bursts, may be significantly more effective in accelerating leptons to high energies McKinney & Uzdensky (2012); Lazarian et al. (2011), and (3) the maximum energy of particles moving through magnetic reconnection is expected to depend sensitively on the geometry of the reconnection region Lazarian et al. (2011), which would be expected to produce very different synchrotron emission spectra in different NRFs. An alternate scenario involves electron acceleration in star formation regions Yusef-Zadeh (2003), although the necessary mechanism to create a peaked electron spectrum in star formation regions is not known.

In this chapter, we propose that dark matter annihilation may provide a physical basis for the nearly monoenergetic electron spectrum necessary to explain NRF emission. Specifically, we find that the highly peaked electron injection spectrum naturally produced

by annihilations of light dark matter particles correctly produces the hard and bright synchrotron emission spectrum observed in multiple NRFs. In § 5.1, we review the astrophysics of filimentary arcs and demonstrate that the ordered magnetic field structure within these objects requires that their synchrotron emission results from electrons and positrons injected from within the filaments themselves, rather than from external sources. In § 5.2, we show that relatively light dark matter particles annihilating to leptons, such as those proposed by Hooper & Goodenough (2011c) to explain the Galactic center γ-ray excess, are also predicted to inject electrons with a spectrum and intensity naturally capable of explaining the synchrotron intensity and spectrum observed from NRFs. In § 5.3, we show that synchrotron emission produced as a product of dark matter annihilation can explain the characteristics of the NRF population, including their spectral conformity and the spherical symmetry of their intensity with respect to the Galactic center. Finally, in § 5.4, we present several testable predictions for this dark matter annihilation scenario with the goal of discriminating this possibility from astrophysical source mechanisms. Further study of the Milky Way's radio filaments may play a critical role in untangling various interpretations of the γ-ray excess observed in the Galactic center.

5.1 The Astrophysics of the Non-Thermal Radio Filaments

The strength of the magnetic fields in NRFs have been estimated through a variety of means. Early estimates centered on the brightest NRF, G0.2-0.0 (the Radio Arc), and were based on a comparison between the magnetic field pressure and the estimated ram pressure from nearby molecular cloud interactions, which indicated magnetic field strengths

as high as 1 mG Yusef-Zadeh & Morris (1987); Morris & Yusef-Zadeh (1989). More recent observations, however, have pointed to somewhat weaker magnetic fields ($\sim 100~\mu$G) among the population of NRFs for three reasons: (1) the observations of kinks in several NRFs such as G359.1-0.2 (the Snake) and G358.85+0.47 (the Pelican) imply that the magnetic field pressure may be significantly smaller than the ram pressure Gray et al. (1995); Lang et al. (1999a), (2) the compact radial extent of the filaments is difficult to explain if a 1 mG magnetic field is surrounded by a region with a significantly weaker galactic magnetic field LaRosa et al. (2004), and (3) synchrotron models of the radio spectrum imply equipartition magnetic fields between approximately 50 and 200 μG Anantharamaiah et al. (1991). Furthermore, in the overall population of NRFs, a turnover of the hard synchrotron spectrum at $\sim$10 GHz is observed, implying a magnetic field strength on the order of 100 μG Boldyrev & Yusef-Zadeh (2006).

Although it has been suggested that these relatively strong magnetic fields may simply trace an extremely strong poloidal magnetic field formed in the Galactic center during the proto-halo phase of galaxy formation Sofue & Fujimoto (1987); Chandran et al. (2000); Crocker et al. (2010), more recent studies have instead interpreted NRFs to contain local enhancements of the relatively weak diffuse magnetic field (Boldyrev & Yusef-Zadeh, 2006; Ferrière, 2009, and references therein.). LaRosa et al. (2005) studied the synchrotron spectral index and flux densities at 74 and 330 MHz, and calculated the strength of the large-scale diffuse magnetic field to be approximately $\sim$10 μG in the inner Milky Way. Furthermore, a ubiquitous poloidal field is unable to explain recent observations of several NRFs which are not aligned perpendicular to the Galactic Disk Lang et al. (1999a); Nord

et al. (2004). Finally, depolarization due to Faraday rotation also implies the strength of the diffuse magnetic field along the line-of-sight to be ∼7 μG Gray et al. (1995).

The strong magnetic fields in NRFs relative to those in the surrounding galactic medium can greatly affect the propagation of cosmic rays into and out of the filaments. The high degree of polarization of the synchrotron emission from NRFs implies that their magnetic fields are highly ordered Yusef-Zadeh & Morris (1987). Assuming that depolarization is dominated by turbulence in the magnetic field, the observed fractional polarization can be approximated as:

$$p \approx p_0(\gamma) \frac{B_0^2}{B_0^2 + B_r^2} = p_0(\gamma) \frac{B_0^2}{B_T^2} \tag{5.1}$$

where $p_0(\gamma)$ is the intrinsic polarization (determined by the index γ of the electron injection spectrum), B_0 is the intensity of the ordered field, B_r is the intensity of a random field with variance $\frac{2}{3}B_r$, and $B_T = \sqrt{B_0^2 + B_r^2}$ is the total field. This solution stands as an equality in the case of a synchrotron spectrum α = -1, and varies only slightly in all relevant cases Burn (1966). Observations of ∼60% polarization in multiple NRFs Yusef-Zadeh et al. (2004) thus indicate magnetic fields with ordered fractions (B_0^2/B_T^2) greater than ∼80%. In reality, depolarizing effects such as Faraday rotation may dominate synchrotron depolarization Lang et al. (1999a), implying a magnetic field which is significantly more ordered than required by this lower limit.

In the presence of highly ordered magnetic fields, the gyroradius of electrons impinging perpendicular to the field lines of the NRFs is extremely small, leading the filaments to act as a magnetic mirror which quickly rejects incident electrons. In Fig. 5.1, we show

the average time that an electron impacting a cylindrical magnetic field with total strength 100 μG remains within a filament before being evicted, as a function of the ordered fraction of the magnetic field. We employ a filament radius of 0.412 pc (10"), and imagine the filament as an infinitely long tube in order to safely ignore any edge effects. Using Monte Carlo methods, we have averaged the result over all initial impact angles between the particle and filament. We find that, for the highly ordered magnetic fields required in NRFs, incident electrons are almost immediately expelled from the filament (within seconds) and thus do not significantly contribute to the synchrotron emission from these objects. While electrons may be able to enter through the edges of a filament aligned with the magnetic field, the geometry of NRFs suggests that this would occur for only a very small ($< 1\%$) fraction of electron impacts, greatly diminishing the electron population within the filament. The jaggedness of this dataset is statistical in nature, and is not relevant for the constraints established here.

5.2 Synchrotron Emission From Dark Matter Annihilation inside of Non-Thermal Radio Filaments

Since magnetic mirroring prevents external electrons from propagating into the NRFs, we are motivated to study the expected synchrotron contribution of electrons and positrons which originate from within the filaments themselves. The injection of energetic electrons/positrons through dark matter annihilations is particularly interesting for four reasons: (1) the dark matter annihilation rate will remain entirely unaffected by the peculiar magnetic properties of the NRFs, allowing for a rigorous comparison in flux between

the filaments and the surrounding interstellar medium, (2) the electron injection spectrum from dark matter will be identical at all locations, providing an explanation for the similar synchrotron spectra observed from multiple NRFs, (3) the dark matter density in the Galactic center is dominated by a smooth component Diemand et al. (2008b), and naturally explains the intensity observed from all NRFs, and (4) a dark matter annihilation scenario at very similar energies has already been proposed to explain Galactic center emission at γ-ray energies Hooper & Goodenough (2011c).

The local dark matter annihilation rate per volume at a location $\vec{x}$ is given by:

$$\Phi_{DM}(\vec{x}) = \frac{1}{2}\langle\sigma v\rangle \left(\frac{\rho(\vec{x})}{M_{DM}}\right)^2 \tag{5.2}$$

where $\rho(\vec{x})$ is the dark matter energy density, M_{DM} is the dark matter particle's mass, and $\langle\sigma v\rangle$ is dark matter's annihilation cross section multiplied by the relative velocity of the WIMPs. We adopt a dark matter distribution based on the results of numerical simulations Navarro et al. (1996b); Diemand et al. (2008b), and given by $\rho(r) = \rho_0 \left(r/8.5\,\mathrm{kpc}\right)^{-1.25}$, where r is the distance from the Galactic center and $\rho_0 = 0.385$ GeV cm^{-3} Catena & Ullio (2010b); Lisanti & Spergel (2012). We also adopt a dark matter annihilation cross section of $\langle\sigma v\rangle = 3 \times 10^{-26}$ cm^3 s^{-1}, which is the value predicted for a simple thermal relic.

Assuming approximate cylindrical symmetry for the filament geometry, the annihilation rate within a filament of length l and diameter w is given by:

$$\Phi_{DM} = 1.4 \times 10^{33}\,\mathrm{s}^{-1} \left(\frac{8\,\mathrm{GeV}}{M_{DM}}\right)^2 \left(\frac{\langle\sigma v\rangle}{3 \times 10^{-26}\mathrm{cm}^3/\mathrm{s}}\right) \times \left(\frac{r}{100\,\mathrm{pc}}\right)^{-2.5} \left(\frac{l}{40\,\mathrm{pc}}\right) \left(\frac{w}{1\,\mathrm{pc}}\right)^2 \tag{5.3}$$

where r is the distance of the filament from the Galactic center. We note that in many NRFs, the distance from the Galactic center changes considerably across the length of the filaments - we will discuss the effect of this when modeling specific filaments.

The types and spectra of particles produced in dark matter annihilations depend on the details of the particle physics model. In order to generate a bright flux of synchrotron emission with a spectrum peaking at $\sim$10 GHz, we will focus on dark matter which annihilates dominantly to charged leptons. In particular, we will consider a democratic model which annihilates equally to $e^\pm$, $\mu^\pm$, and $\tau^\pm$ final states. The nearly instantaneous decays of the taus and muons produce lower energy electrons/positrons, as well as a prompt flux of γ-rays (as opposed to γ-rays from the inverse-Compton scattering of energetic electrons). It is this prompt flux of γ-rays which Hooper & Goodenough (2011c) find to be consistent with the excess observed in the Galactic center by Fermi-LAT.

The spectrum of electrons and positrons produced through dark matter annihilations within a given NRF is calculated using the Pythia package Sjöstrand et al. (2001b); Gondolo et al. (2004). In the left frame of Fig. 5.2, we show the injected electron spectrum per dark matter annihilation for our canonical case of a dark matter particle with a mass of 8 GeV, annihilating equally into e^+e^-, $\mu^+\mu^-$ and $\tau^+\tau^-$. We note that the electron/positron spectrum is very hard, following a spectrum between $\mathrm{E}^{-0.5}$ and E^0 between 100 MeV and 8 GeV, although we caution that this spectrum is not a continuous power law. The majority ($\sim$2/3) of the electron energy is deposited in a delta function at 8 GeV following the dark matter annihilations directly into electrons. These 8 GeV electrons will dominate the synchrotron spectrum from NRFs, in part due to their shorter synchrotron energy loss

time. We note that the positron spectrum is identical and lends another factor of two to the overall synchrotron flux.

In order to determine the synchrotron spectrum expected from dark matter annihilations, we must also model the diffusion of electrons throughout the NRFs. Models of the filaments typically require an electron diffusion timescale similar to the energy loss time of the electron population in the NRF's magnetic field Gray et al. (1995); Lang et al. (1999b). This has the effect of smearing out the electron energy distribution and softening the overall synchrotron spectrum. Through considerations of the electron gyroradius similar to those discussed in § 5.1, electrons created within the NRFs are constrained from effective diffusion perpendicular to the ordered magnetic field. In the case of an entirely ordered magnetic field, charged leptons would spiral freely along the magnetic field lines until exiting the filament. However, in the observed regime containing significant ordered and unordered fields, diffusion is expected to be significantly more complicated.

In the case of very low turbulence levels, much work has been done within the perturbative framework of quasi-linear theory which seeks to calculate the parallel and perpendicular diffusion components as a function of the power in turbulent modes of the magnetic field with a wavenumber resonant with the inverse of the particles momentum Jokipii (1966, 1971). The amplitude of these modes, however, is poorly constrained in galactic simulations. More recently, numerical simulations have been used to analyze the parallel and perpendicular diffusion constants in regimes in which the ordered and unordered field are co-dominant. Notably, Casse et al. (2002) found that in the case of a magnetic field which is approximately 80% ordered, the parallel diffusion constant exceeds the perpendic-

ular diffusion constant by a factor of ∼125. Very similar results were later obtained for the case of more energetic cosmic rays DeMarco et al. (2007). Since the length travelled by diffusive particles can be written as $\ell = \sqrt{2Dt}$, where D is the assumed diffusion constant. This implies that perpendicular and parallel diffusion will remove particles from the filaments on equivalent timescales if the parallel and perpendicular extent of the NRFs is approximately 125 to 1. This length-scale is similar to the observed length to width ratio in multiple filamentary structures Yusef-Zadeh et al. (2004), implying that diffusion along the length of the filamentary arcs acts on a similar time frame to diffusion across the much smaller NRF width. Since the calculation of magnetic field order stands as a lower limit in this calculation, it is feasible that perpendicular diffusion is in fact entirely irrelevant in the population of NRF structures.

The overall normalization of the diffusion constant depends sensitively on the length scale of the turbulent disturbances in the magnetic medium Jokipii (1966) and is highly uncertain. While simulations are able to constrain the mean galactic diffusion constant through observations of cosmic ray primary-to-secondary ratios at the solar position (e.g Strong & Moskalenko, 1998), these simulations do not constrain local diffusion constants, especially in magnetically unique regions such as NRFs.

The synchrotron energy loss time of an electron is given by:

$$\frac{E}{\dot{E}} \;=\; 6.6 \times 10^{12} \text{ s} \; \left(\frac{8 \,\text{GeV}}{E}\right) \left(\frac{100 \;\mu G}{B}\right)^{2} \qquad (5.4)$$

Due to the difficulties of calculating the diffusion constant within a partially ordered magnetic field, we choose a parallel diffusion constant such that electrons remain

within the NRF for a length of time given by:

$$T_{\text{confinement}} = \frac{E}{\dot{E}} \times \left(\frac{8\,\text{GeV}}{E}\right)^{0.33} = 6.6 \times 10^{12} \text{ s } \left(\frac{\tau}{1}\right) \left(\frac{8\,\text{GeV}}{E}\right)^{1.33} \left(\frac{100\,\mu G}{B}\right)^2 \quad (5.5)$$

where τ is the ratio of the diffusion timescale for 8 GeV electrons compared to their synchrotron energy loss time. For example, in the case $\tau = 1.0$, 8 GeV electrons diffuse out of the NRF on a timescale equal to their synchrotron energy loss time. Thus the τ parameter can also be seen as an indicator of the average synchrotron exhaustion, or the average time that an electron generated by dark matter annihilation has propagated through the NRF before producing the synchrotron emission presently observed. The additional factor of $E^{-0.33}$ accounts for the energy dependence of the diffusion constant calculated by Kolmogorov (1941). We note that the synchrotron softening of an electron spectrum for a given value of τ is independent of the magnetic field strength. In Fig. 5.2 (right), we show the spectrum of electrons from dark matter annihilations after accounting for synchrotron energy losses for $\tau = 1.0$.

We are now prepared to calculate the synchrotron spectrum resulting from dark matter annihilations taking place within a NRF. In Fig. 5.3, we plot the synchrotron spectrum from dark matter annihilations for magnetic field strengths of 50 μG, 100 μG, and 200μG and for values $\tau =$0.1, 1.0 and 2.0. In each case, we predict a peak in synchrotron energy at $\sim$1-10 GHz followed by a suppression of the synchrotron emissivity at higher frequencies. In the following section, we will compare this prediction to the synchrotron spectrum observed from specific NRFs.

5.3 Comparison to Specific Filaments

In astrophysical interpretations of NRF observations, variations in the electron injection spectrum can be invoked to effectively explain the different spectral features in each NRF, since the peak of the synchrotron emission spectrum depends on the square of the electron energy. However, in the case of dark matter annihilations, the injected electron spectrum must be uniform in each filament. Variations in the observed synchrotron spectra may still originate from differences in either the magnetic field strength or diffusion timescales of each NRF. These effects are relatively weak, however, and would be unable to explain extreme variations in the spectral turnover of different NRFs. Thus a population survey of the synchrotron spectra in NRFs remains a powerful diagnostic for testing the dark matter interpretation.

In Table 5.1, we have compiled the observed synchrotron spectra of the most thoroughly studied NRFs. We find the population to be relatively homogeneous, with a hard spectrum below $\sim$5 GHz that quickly turns over at higher frequencies. The variation in the spectral turnover from the hardest NRF (G0.2-0.0, Radio Arc) to the softest (G0.08+0.15, Northern Thread) is approximately an order of magnitude.

In order to test whether magnetic field and diffusion timescale variations can explain these spectral and intensity variations within the highly constrained framework of a uniform electron injection spectrum, we consider four NRFs with particularly well measured spectra and intensities: G0.2-0.0 (the Radio Arc, Reich, 2003), G0.16-0.14 (the Arc Filament, Sofue et al., 1992), G0.08+0.15 (the Northern Thread, Lang et al., 1999b) and G359.1-0.2 (the Snake, Gray et al., 1995). Data were extracted using the Dexter pack-

Name	Alternative	$\alpha_{0.33}^{1.4}$	$\alpha_{1.4}^{4.8}$	$\alpha_{4.8}^{>}$	References
G0.08+0.15	N. Thread	-0.5	-0.5	-2.0	Lang et al. (1999b)
G358.85+0.47	The Pelican	-0.6	-0.8±0.2	-1.5±0.3	Kassim et al. (1999)
G359.1-0.2	The Snake	-1.1	∼0.0	*	Nicholls & Gray (1993)
G0.2-0.0	Radio Arc	——-	+0.3	+0.3	Sofue et al. (1992)
G0.16-0.14	Arc Fil.	——-	0.0	-0.8	Sofue et al. (1992)
G359.32-0.16	——-	-0.1	-1.0	————	LaRosa et al. (2004)
G359.79+0.17	RF-N8	-0.6±0.1	-0.9;-1.3	———-	Law et al. (2008a)
G359.85+0.39	RF-N10	0.2;-1.1**	-0.6;-1.5**	——-	LaRosa et al. (2001)
G359.96+0.09	S. Thread	-0.5	———	———	LaRosa et al. (2000b)
G359.45-0.040	Sgr C	-0.5	———	-0.5±0.3	Liszt & Spiker (1995)
G359.54+0.18	Ripple	———	-0.5;-0.8	——-	Law et al. (2008a)
G359.36+0.10	RF-C12	———	-0.5;-1.8	——-	Law et al. (2008a)
G0.15+0.23	RF-N1	———	+0.2;-0.5	——-	Law et al. (2008a)
G0.09-0.09	———	———	——-	0.15	Reich (2003)

Table 5.1 Spectral Characteristics of Observed Non-Thermal Radio Filaments

*Spectrum is highly position dependent, but shows a clear trend towards steeper spectral slopes at high frequencies for any given position

**Two very different values exist in the literature for the high frequency spectrum of G359.1-0.2. Gray et al. (1995) cites a value of -0.2 ± 0.2, while a more recent analysis by Law et al. (2008b) yields $\alpha_{4.8GHz}^{8.33}$ = -1.86 ± 0.64

age Demleitner et al. (2001), and is shown with the statistical errors and astrophysical background subtraction determined by each study. In each case, we calculate the flux at the point of maximum 1.4 GHz emission, with the exception of the Snake. For that filament, the peak emission corresponds to a "kink" in the NRF morphology which shows a spectral index representative of astrophysical injection. Thus for the Snake, the flux is determined at a point where the spectral index $\alpha_{1.4\ GHz}^{4.8\ GHz}$ is entirely flat, which lies at approximately 19' in the Gray et al. (1995) nomenclature.

In Fig. 5.4, we provide dark matter fits to the intensity and spectrum of these four NRFs. For the Radio Arc (top left), we adopt a representative distance from the Galactic center of 20 pc, a diameter of 20 pc, a magnetic field of 290 μG and a diffusion timescale of 7.9 x 10^{11} s ($\tau = 1.0$). For the Arc Filament (bottom left), we adopt the same distance of 20 pc, using a filamentary diameter of 0.62 pc, a magnetic field of 100 μG and a diffusion timescale of 1.7 x 10^{13} s ($\tau = 2.5$). For the Northern Thread, we employ a Galactic center distance of 30 pc, a diameter of 1 pc, a magnetic field of 50 μG, and a diffusion timescale of 2.5×10^{14} s. Finally, for the Snake we adopt a Galctic Center distance of 120 pc, a diameter of 7 pc, a magnetic field of 100 μG and a diffusion timescale of 1.9 x 10^{13} s ($\tau = 2.0$).

One potential mismatch in our best fit parameters concerns the larger widths necessary for the dark matter component to match the intensity of the observed radio filaments. While we have produced best fit widths of 7' for the Radio Arc, 0.4' for the Northern Thread, 0.25' for the Arc Filament, and 2.8' for the Snake, observational data supports smaller widths of 4' for the Radio Arc Reich (2003), 0.07'-0.2' for the Northern Thread Lang et al. (1999b), 0.3' for the Arc Filament Sofue et al. (1992) and 0.2'-1.0' for

the Snake Gray et al. (1995); Anantharamaiah et al. (1991). However this mismatch may be expected for three reasons. First, we have in general attempted to match the peak luminosities observed within the NRFs, while our simulations calculate the average luminosity expected throughout the enhanced magnetic field region of the NRF. Changes in the magnetic field intensity and structure may confine electrons more effectively in specific regions of a NRF, which would then show luminosities significantly brighter than those predicted by dark matter. Secondly, observations calculating the width of the NRFs would be expected to miss the outer regions of enhanced magnetic field, where the decreased width of the filament would produce only negligible emission. Third, the distance to the Galactic center may change considerably over the length of the NRF, producing enhanced annihilation rates at regions near the Galactic center. For instance, if the Northern Thread is more correctly modeled to extend linearly from 20 pc to 45 pc from the Galactic center, the total annihilation rate is enhanced by over 50%. However, even these features may be insufficient to explain the extremely large diameters necessary to explain synchrotron emission in G359.1-0.2 (the Snake). We note that our analysis does not preclude astrophysical mechanisms formed within the filament from also contributing to the synchrotron emission spectrum, which may be the case in this particularly bright filament.

A second issue in this analysis concerns the implication that the diffusion constant is significantly lower in filaments with particularly soft spectra. These disparities are not unique to a dark matter scenario, and have traditionally existed in astrophysical interpretations of these NRFs (cf. Tsuboi et al., 1995; Lang et al., 1999b). In both dark matter and astrophysical scenarios, this may be understood in a model where the filaments exist as an

entirely ordered magnetic enhancement superimposed on a random diffuse magnetic field of approximately 10 μG which permeates the Galactic center region. The differing ratios of the ordered to random magnetic fields (e.g 80% in the Northern Thread vs. nearly 100% in the Radio Arc) would then drive significantly enhanced parallel diffusion in the Radio Arc. Alternatively, assumptions that the Alfvèn velocity places an upper limit on the speed of electron diffusion implies a diffusion timescale which scales as B^{-1} and would approximately match the ratio of diffusion timescales observed in these two systems Alfvén (1942). We note, however, that this effect is not well understood and remains a significant assumption in our model. Lastly, it is possible that the magnetic field structures at the edges of the NRFs are configured to allow significant reflection of trapped electrons Heyvaerts et al. (1988).

Another necessary feature in any dark matter model of NRFs concerns the radial dependence of the electron injection spectrum. As shown in Eqn. 5.3, the dark matter annihilation rate within a given filament falls off as $\sim r^{-2.5}$, where r is the distance of the filament to the dynamical center of the galaxy. A quantitative observation of the electron injection spectrum in individual filaments is difficult, due to the varying lengths, widths, magnetic fields, and diffusion constants in the observed filaments. However, the distance from the Galactic center to various NRFs is thought to span nearly an order of magnitude, which implies an injection spectrum that varies by more than a factor of 300 throughout the NRF population. This makes the statistical observation of such a feature possible, even with extremely crude estimations for the astrophysical parameters of individual NRFs. In order to examine this necessary trend, we have studied the observations of 7 NRFs with

integrated fluxes and lengths observed at 330 MHz in the LaRosa et al. (2000b) catalog, as well as the 13 NRFs observed at 1.4 GHz in the Yusef-Zadeh et al. (2004) catalog. In both cases, integrated fluxes as well as lengths, are provided. We assume a constant radial width for all NRF, noting that quoted widths for most NRFs fall approximately within a factor of two. For this reason, we have removed the Radio Arc from our datasets as this assumption is particularly poor for that filament.

The total luminosity of a NRF is expected to depend sensitively on its length. In addition to the linear dependence of the dark matter annihilation rate on the length of a filament, longer filaments are expected to retain electrons for longer periods of time and as a result will deposit a greater fraction of their initial energy into synchrotron radiation within the filament. In this work, we consider three scenarios to account for the influence of a NRF's length. First, we we consider the case in which electrons are effectively confined and lose their energy to synchrotron radiation on timescales much smaller than the diffusion timescale ($\tau \gg 1$). In this case the total flux in an NRF should depend only linearly on the length of the filament. Second, in the case that electrons free stream through the filaments on timescales much smaller than the synchrotron energy loss time ($\tau \ll 1$), the amount of energy deposited by a single electron into the filament is expected to scale with the length of the filament, providing a total flux which scales with the length of the filament squared. Finally, in the case that electrons diffusively propagate through the filament on a timescale smaller than the synchrotron energy loss time ($\tau \ll 1$ with $D_0/c \ll$ filament length) the total energy deposited by an electron inside the filament will vary as the square of the filaments length, providing a total flux which varies as the cube of the length of

the filament. The cases in which the total flux scales with l and l^3 effectively bracket the possible degrees of correlation between the length of a NRF and it's total flux, while the l^2 case can be considered something of a median expectation.

We first examine the observed dataset at 330 MHz. In the left frames of Fig. 5.5, we plot the flux per unit length (top), per unit length squared (middle) and per unit length cubed (bottom) as a function of the projected distance of each NRF to the Galactic center. In each case, we note no significant trend between the distance of a given filament from the Galactic center. In other words, the distance of a given filament from Galactic center does not appear to have significant bearing on its emission at 330 MHz, suggesting that astrophysical mechanisms (*i.e.* not dark matter annihilations) are responsible for the emission at this frequency.

The same conclusion is not found at 1.4 GHz, however. At this frequency (right), we see a very significant correlation between the projected distance of a filament to the Galactic center and its observed intensity. In particular, filaments closer to the Galactic center tend to be considerably brighter at 1.4 GHz than those farther away. We note that for the dark matter halo profile used in this chapter, we predict a flux which scales with $r^{-2.5}$, while a more generic range of profiles predicts behavior between roughly r^{-2} and r^{-3}.

There are several interesting features of the results shown in Fig. 5.5. First, although the correlation observed among the filaments in the 1.4 GHz dataset could have plausibly been the result of a selection effect resulting from the presence of greater astrophysical backgrounds closer to the Galactic center, the 330 Mhz observations dispute this reasoning, as does the lack of any bright NRFs at 1.4 GHz far from the Galactic center. The

different trends observed in these datasets instead support the surprising conclusion that the electron injection spectra which produces the emission at 1.4 GHz is physically distinct from the emission mechanism which dominates at 330 MHz. Both trends are naturally explained in the case of a light dark matter particle in a magnetic field of $\sim 100~\mu$G, as the synchrotron spectrum will peak at approximately 1 GHz, with astrophysical processes dominating the emission at lower frequencies.

We caution that this relationship is still somewhat tenuous, due to the varying NRF widths, magnetic fields, three dimensional distances, and diffusion constants which are not modeled in this analysis, and additional studies will be necessary to better identify and refine this apparent trend. If dark matter annihilations are in fact responsible for a sizable fraction of the emission observed at 1.4 GHz, improved measurements of these parameters should enhance the correlation shown in Fig. 5.5. Furthermore, if astrophysical mechanisms dominate the low energy synchrotron emission, then we would expect the spectral slope in this region to be relatively soft. We note that the observed trend is steepest among the 1.4 GHz NRFs which were not included in the 330 MHz analysis, making additional measurements in this region necessary to better understand the apparent mismatch between low and high frequency observations. Finally, we note that no correlation such as that described here would be expected in reconnection or shock acceleration models of NRF. However, models based on a monoenergetic electron flux from Sgr A* could plausibly lead to a similar relation, although as argued in § 5.1, such electrons are not expected to penetrate into the NRFs.

5.4 Discussion and Conclusions

The observed synchrotron emission from non-thermal radio filaments (NRFs) in the Inner Milky Way have long been difficult to explain with known astrophysical mechanisms. In this chapter, we have proposed that dark matter annihilations taking place within these filaments could produce the nearly monoenergetic electron spectrum necessary to generate the hard synchrotron emission that is observed. In this regard, dark matter annihilations have several advantages over proposed astrophysical mechanisms. First, electrons produced through dark matter annihilations yield a synchrotron spectrum in good agreement with the hard spectral index and turnover observed from NRFs, without mandating finely tuned magneto-hydrodynamic interactions to move electrons independently into equivalent monoenergetic electron distributions. Second, WIMPs annihilating into leptonic final states, such as those employed at low masses in order to explain the Fermi-Galactic center excess Hooper & Goodenough (2011c), are predicted to inject electrons into the Galactic center region with an energy density very similar to the synchrotron signal observed from NRFs. Lastly, as shown in Fig. 5.5, dark matter annihilations naturally explain the observed correlation between the radial distance of NRFs to the Galactic center and the inferred electron injection spectrum in the filaments.

A dark matter origin of the observed radio emission from NRFs yields several concrete and testable predictions. In particular, the dark matter annihilation rate and corresponding flux of injected electrons must show approximate spherical symmetry with respect to the Galactic center (Diemand et al., 2008b), and the injected spectrum of electrons must be identical for all filaments throughout the Galactic center. This is not the case for

other proposed astrophysical mechanisms, for which the electron injection spectrum can vary from filament to filament. Furthermore, we have demonstrated that the intensity of 1.4 GHz emission is significantly enhanced for NRFs near the Galactic center compared to those farther away, as would be expected from dark matter distributed in a cusped halo profile. Observations which are able to independently determine or constrain the magnetic field strengths and other characteristics among a population of NRFs could be used to further examine any scenario requiring a single electron injection spectrum. If dark matter annihilations are found not to power NRFs, these objects may be used to place stringent constraints on the dark matter annihilation rate in the region surrounding the Galactic center. New observations of NRFs will thus be integral to resolving both the astrophysics and particle physics of these unusual regions.
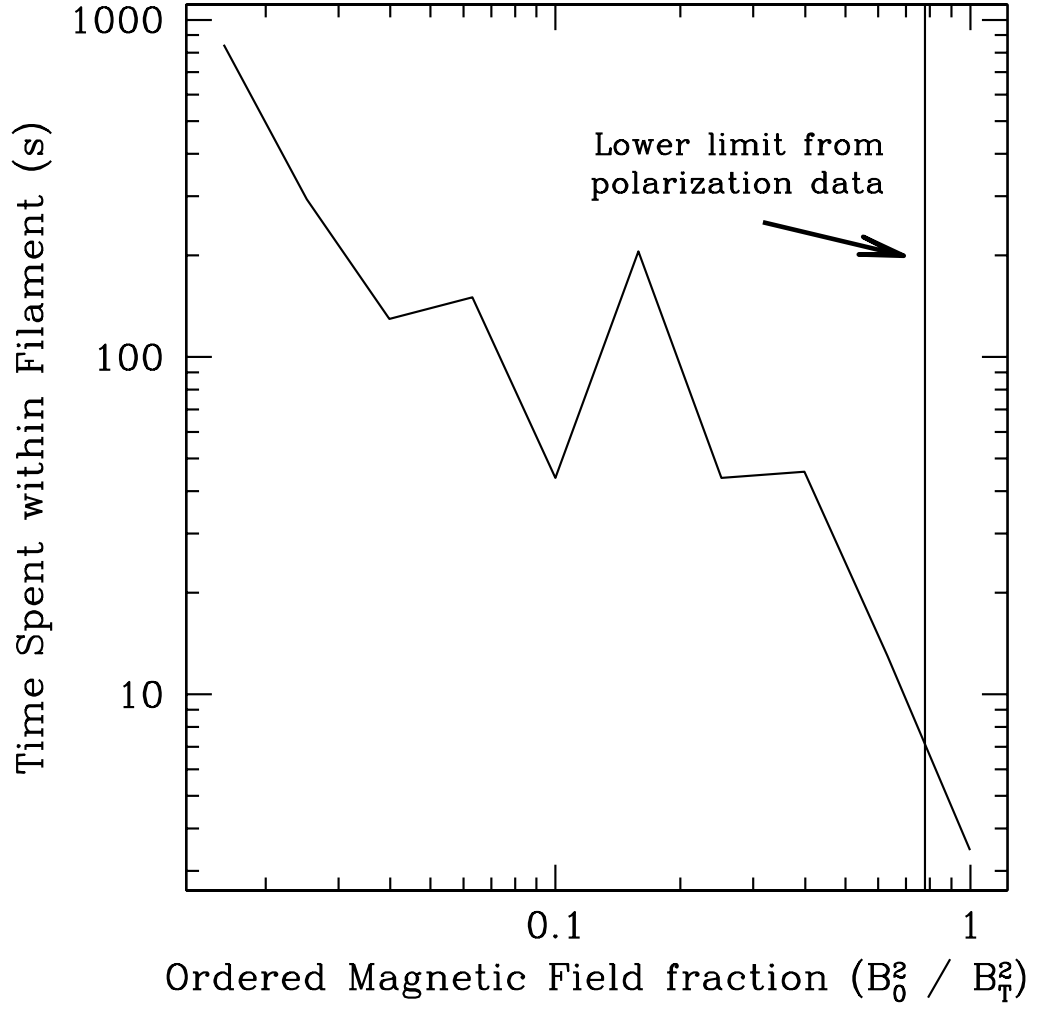
Figure 5.1 The average time that 10 GeV electrons spend within a filament of total magnetic field of 100 μG after impacting its side, as a function of the ordered fraction of the magnetic field energy density within the filament. This time is insignificant compared to the $\sim 10^{12}$ second energy loss time for these particles, indicating that externally produced electrons contribute only a negligible fraction of the synchrotron radiation from NRFs.
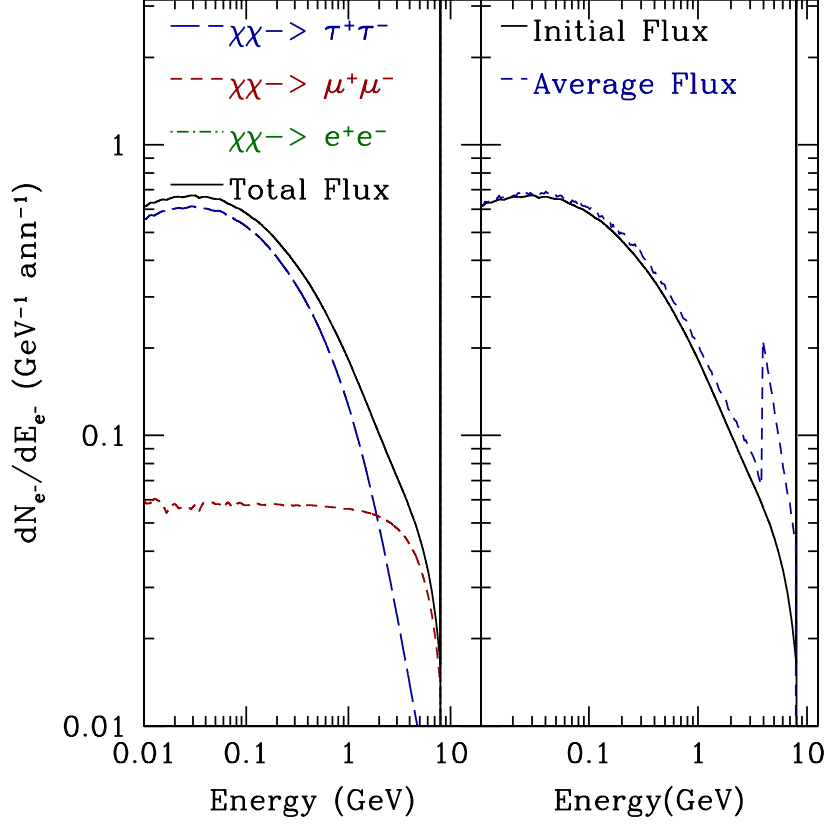
Figure 5.2 (Left) The spectrum of electrons injected through the annihilation of an 8 GeV dark matter particle to e^+e^-, $\mu^+\mu^-$ and $\tau^+\tau^-$ (democratically). Note that the contribution from e^+e^- takes the form of a delta function at 8 GeV and is concealed by the line denoting the "Total Flux". (Right) The spectrum of electrons from dark matter annihilations before (solid) and after (dashed) synchrotron energy losses for an energy loss time of $\tau = 1.0$ (as defined in Eqn. 5.5). The direct flux to electrons represents a delta function at the 8 GeV mass of the dark matter particle which carries approximately 2/3 of the total electron energy. The positron flux has an identical energy dependence and lends a factor of two to the total lepton flux from dark matter annihilation.
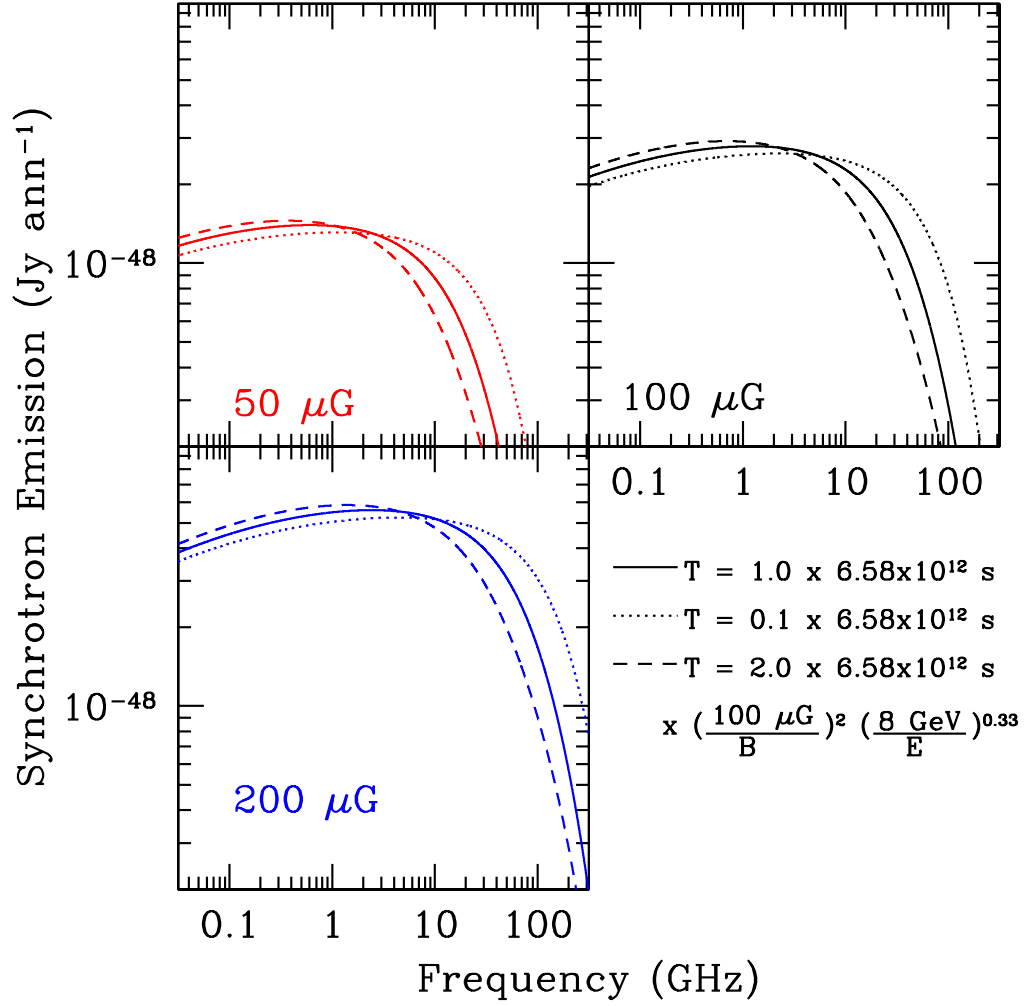
Figure 5.3 The spectrum of synchrotron radiation (in Janskys, defined as 10^{-26} watts per square meter per Hz) from electrons produced by the annihilation of an 8 GeV dark matter particle democratically into leptonic final states in magnetic fields of 50 μG (red, top left), 100 μG (black, top right), and 200 μG (blue, bottom), with the electron distribution softened during propagation times of $\tau = 1.0$ (solid), 0.1 (dotted) and 2.0 (dashed).
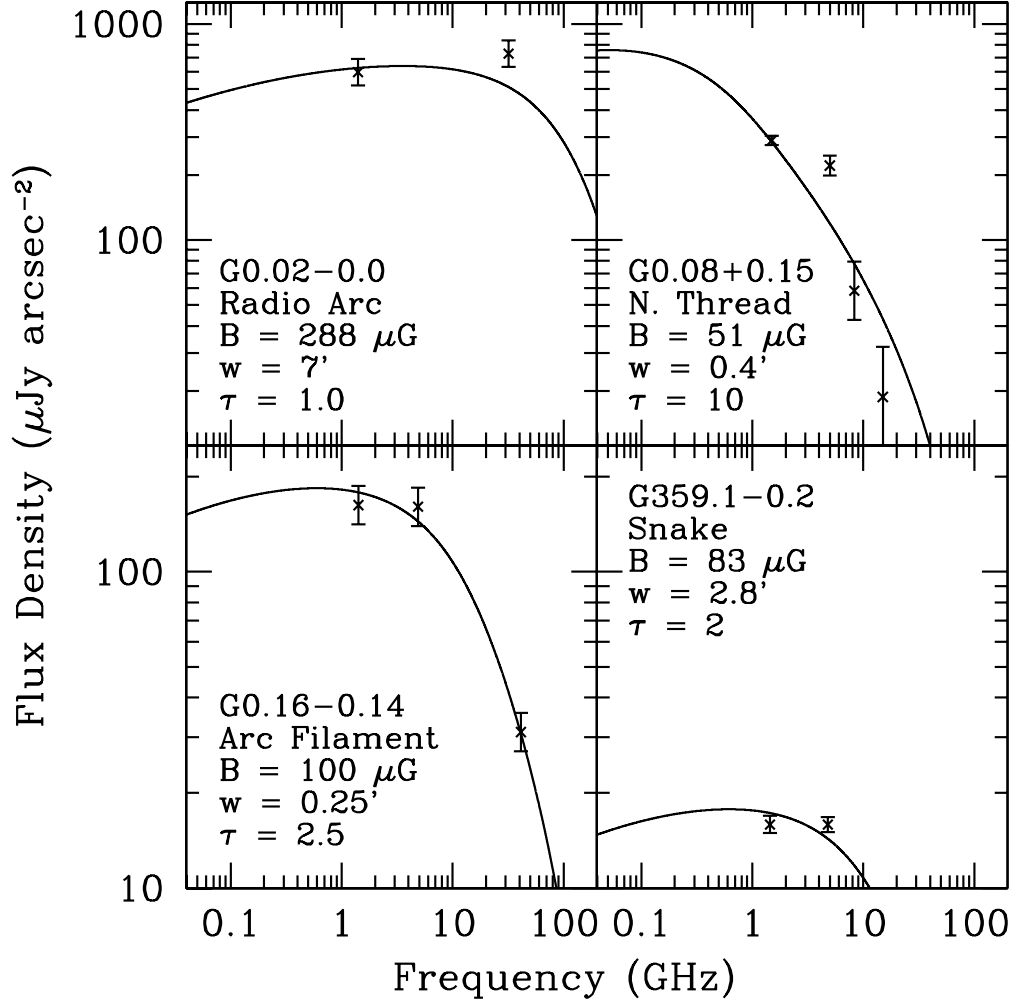
Figure 5.4 The synchrotron energy spectrum predicted from dark matter annihilations ($M_{\text{DM}} = 8$ GeV, annihilating to e^+e^-, $\mu^+\mu^-$ and $\tau^+\tau^-$ with $\langle\sigma v\rangle = 3 \times 10^{-26}$ cm^3 s^{-1}) compared to the observed intensity and spectrum of G0.2-0.0 (the Radio Arc, top left), G0.08+0.15 (Northern Thread, top right), G0.16-0.14 (Arc Filament, bottom left) and G359.1-0.2 (the Snake, bottom right). The magnetic fields, filamentary width, and synchrotron energy loss times are shown for the synchrotron match to each filament.
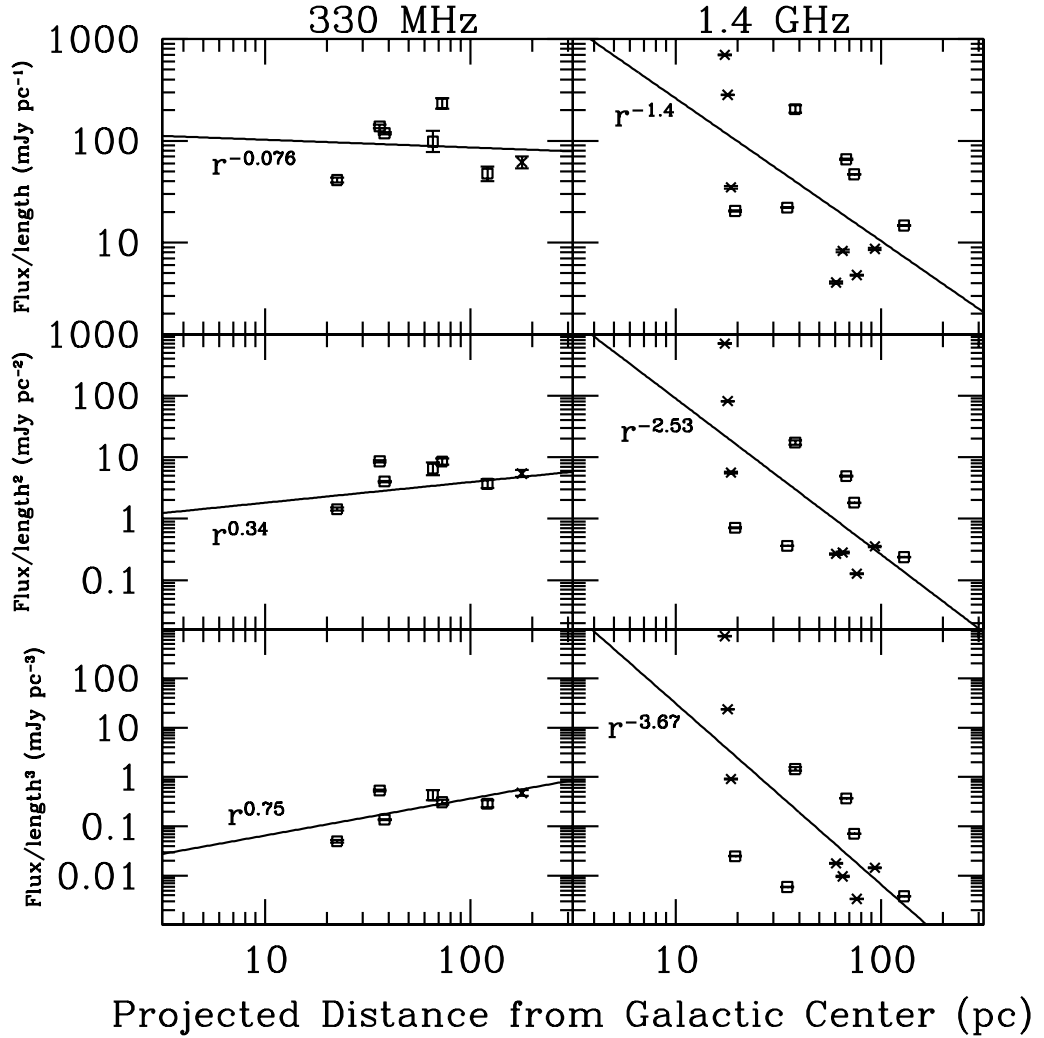
Figure 5.5 Flux per unit length (top), per length squared (center), and per length cubed (bottom) for NRFs at 330 MHz (left)LaRosa et al. (2000b) and 1.4 GHz (right) Yusef-Zadeh et al. (2004), as a function of the projected distance of each filament from the Galactic center. Error bars based on the integrated flux, as well as a best-fit linear regression are shown for each frame. Boxed points indicate NRFs which are listed in both the 1.4 GHz and 330 MHz datasets. At 330 MHz, there is no clear correlation between the flux and the distance of a filament from the Galactic center. At 1.4 GHz, however, those filaments closer to the Galactic center are clearly brighter than those farther away.

123

Chapter 6

Conclusion

6.1 The Status of Light Dark Matter Models

Since the original observations of the extended γ-ray excess at the galactic center (Hooper & Goodenough, 2011b; Hooper & Linden, 2011c), several follow up studies have improved on the modeling an interpretation of the studies, with similar qualitative results. Models by Abazajian & Kaplinghat (2012) employed a sophisticated template-approach in order to model the GC excess, under the assumption that relaxing the point-source models from those used in Hooper & Linden (2011c) would reduce the significance of the excess. Instead, they found a $>20\sigma$ preference for an extended, spherically symmetric excess, with a spectrum almost identical to that of Hooper & Linden (2011c). Since this more sophisticated model allows all fluxes to be recomputed in order to present a best fit model of the data, it demonstrates that the spherically symmetric excess is a significant component of the γ-ray sky in the GC region.

Additionally, work by Hooper & Slatyer (2013) examined the spectral variation

in the Fermi bubbles as a function of the galactic latitude, hoping to pinpoint a source of spectral softening which might indicate the origin of the bubble γ-rays. Interestingly, they instead discovered at low galactic latitudes (10-30° above the Galactic plane) a spectral feature nearly identical to that observed in the GC Hooper & Slatyer (2013). The power of this signal as a function of galactic latitude is equivalent to expectations from a dark matter particle following a density profile $\rho(r) \propto \mathrm{r}^{-1.2}$, which is equivalent to the best fit measurements from the GC. We have recently worked to determine whether this excess may be due to a population of MSPs in the galactic bulge, and found that the spectrum and luminosity distributions of MSPs necessary to explain this excess are highly disfavored (Hooper et al., 2013).

Finally, additional evidence has accumulated indicating the existence of a light dark matter particle. Work by Hooper et al. (2012a) observed the hard excess in synchrotron radiation reported by the ARCADE-II collaboration (Fixsen et al., 2009) and found that it is well modeled by light, leptophilic, dark matter candidates. Additionally, results by the CDMS collaboration have found a statistically significant excess in low energy events, compared to background expectations. If interpreted as a dark matter signal, their excess is best interpreted as a dark matter particle of 8.6 GeV (CDMS Collaboration et al., 2013a). These observations are in reasonable agreement with observations by the CoGeNT (Aalseth et al., 2011c,a), DAMA/LIBRA (Bernabei et al., 2010a) and CRESST (Angloher et al., 2012) experiments. However, these models are also currently ruled out by the Xenon 100 collaboration (Aprile et al., 2011; Angle et al., 2011). As these experiments are currently at odds with each-other, more work will be necessary in order to understand the current

evidence pointing towards the direct detection of a light dark matter particle.

However, several astrophysical observations also exist which disfavor a the interpretation of the GC and bubble excesses as light dark matter. For instance, observations by the Wilkinson Microwave Anisotropy Probe (WMAP) satellite found an excess in hard synchrotron emission in regions between 7-20° off of the GC, which was initially interpreted as a possible signal of dark matter annihilation (Hooper et al., 2007; Finkbeiner, 2004). Specifically, it was shown in Hooper & Linden (2011a) that this residual could be fit by the synchrotron radiation produced by light, leptophilic dark matter - with similar properties to models needed to explain the GC excess. However, an analysis by Dobler (2012) found the excess to be highly correlated to the Fermi-bubbles observed by Dobler et al. (2010) and Su et al. (2010). This excess does not appear to be compatible with a dark matter interpretation, due to the sharp edges observed in the excess emission morphology. Additionally, this signal is definitely incompatible with models of light dark matter annihilation, as the Fermi bubble spectrum extends to energies far higher than the light dark matter mass. However, it is worth noting that the failure of dark matter to explain the WMAP excess does not greatly constrain light dark matter models, as the updated magnetic field measurements in the bubble region obtained by Hooper & Slatyer (2013) imply that the dark matter contribution to the observed synchrotron radiation would fall nearly an order of magnitude below current bounds.

Additionally, a survey of synchrotron radiation from nearby galaxies by Carlson et al. (2013a) indicates that a reasonable population of nearby galaxies with similar physical characteristics to the Milky Way have synchrotron intensities which are suppressed com-

pared to our galaxy by several orders of magnitude. In astrophysical models of the WMAP haze, the galaxy-to-galaxy variability of the synchrotron emission strength can be explained by transient events, such as recent supernovae or AGN activity, which vary highly between galaxies. However, in dark matter annihilation models, the electron injection intensity must remain constant in time. This implies that the diffusion parameters of some "Milky Way twin" galaxies must highly disfavor synchrotron emission compared to the Milky Way. For example, the magnetic fields strengths of these galaxies might have to be an order of magnitude weaker than Milky Way observations indicate. While the diffusion parameters of nearby galaxies are highly uncertain (making any quantitative constraint on dark matter difficult to ascertain) it is concerning that many nearby galaxies have synchrotron signals which are underluminous by several orders of magnitude compared to dark matter expectations.

Additional work will certainly be necessary in order to verify, or rule out, the multiple tentative pieces of evidence pointing towards a light WIMP particle. It is unfortunately somewhat difficult to test the dark matter interpretation of the γ-ray excess at the galactic center with Fermi-LAT observations of other sources, such as dwarf spheroidal galaxies or galaxy clusters, and the current limits from each regime are not projected to reach the cross-section compatible with GC observations by the end of the Fermi-LAT lifespan Geringer-Sameth & Koushiappas (2011); Ackermann et al. (2010). Perhaps the most promising future constraint comes from CMB observations, which currently fall only a factor of $\sim$2 above light dark matter cross-section (Galli et al., 2011). Notably, CMB limits are able to place the strongest constraints on leptophilic interactions, since they produce

the most significant reheating of the universe. Updated constraints from the PLANCK collaboration are likely to push this experimental bound well into the best fit region of the GC γ-ray signal. Additionally, collider constraints from the LHC are likely to greatly constrain specific dark matter particle models (Goodman et al., 2010, 2011; Rajaraman et al., 2011).

6.2 Observations Indicating Other Dark Matter Models

Additionally, recent observations have produced evidence supporting dark matter particles with other parameters that are not compatible with the excess at the GC. One such signal is the anomalous rise in the positron fraction as a function of energy observed by the PAMELA satellite (Adriani et al., 2009b), as well as the Fermi-LAT (Ackermann et al., 2012) and AMS-02 (Aguilar et al., 2013). This stands in direct contrast to expectations from the secondary production of positrons via pion-decay produced by a steeply falling primary proton injection spectrum. This idea is well-motivated, as Majorana dark matter annihilation would be expected to produce electrons and positrons in equal abundance, explaining the substantial rise in the positron fraction. A dark matter candidate explaining the PAMELA excess must have three generic properties: (1) the dark matter particle must be relatively massive E > 350 GeV, in order to explain the highest energy positrons observed by AMS-02, (2) the dark matter particle must annihilate primarily to leptonic final states, in order to avoid the overproduction of antiprotons compared to observations, and (3) the dark matter particle must annihilate at rates significantly above the thermal cross-section, in order to explain the large excess of observed positrons. Myriad dark matter models have been formulated which satisfy these three constraints, e.g. Arkani-Hamed et al. (2009),

Cholis et al. (2009), Cirelli et al. (2009) and others too numerous to be listed here.

However, the rising positron fraction observed by PAMELA, Fermi-LAT and AMS-02 can also be explained by an astrophysical source. Energetic pulsars are thought to produce electron/positron pairs as electromagnetic waves propagate through the super-strong magnetic fields produced by pulsar rotation. The PAMELA excess can be fit adequately by both models of galactic pulsars (Hooper et al., 2009; Barger et al., 2009), and also by considering the contribution from only a few nearby pulsars, which may dominate the total pulsar contribution to the positron excess (Profumo, 2012). Interestingly, if nearby pulsars dominate the signal, then they may also induce an anisotropy in the total electron-plus-positron flux, a result which may be tested by the Fermi-LAT (Profumo, 2012). A recent analysis by Linden & Profumo (2013) found that the slight flattening of the increasing positron spectrum favors a nearby pulsar explanation, and also posits that the large effective area of ACTs may allow them to provide stronger limits on the total electron anisotropy compared to the space-based telescopes.

Perhaps the most exciting recent evidence for particle dark matter is the observation by Weniger (2012) of a line in the Fermi-LAT data with an energy of approximately 130 GeV and observed near the GC. This finding, which was quickly confirmed by an analysis by Su & Finkbeiner (2012), lead to an outburst of activity from the physics community, as a line signature is extremely difficult to generate with astrophysical sources. A peculiar feature of the γ-ray line is that the intensity of line photons is consistent with an interaction cross-section which is approximately an order of magnitude higher than that expected by loop-suppressed diagrams of dark matter annihilation into two γ-ray photons. However,

nearly 100 papers (see Carlson et al. (2013b) for a nearly complete list) have thus far been written in order to discuss various models which may resolve this inconsistency.

More troubling, perhaps, is the possibility that inconsistencies in the event reconstruction by the Fermi-LAT telescope at high energies may be artificially inducing a line into the Fermi-LAT data. This is particularly worrisome, as the number of events at these very high energies is relatively small, making it difficult to adequately check instrumental systematics. An early analysis by Finkbeiner et al. (2013) found evidence that the 130 GeV line also existed in Albedo photons observed in Earth's atmosphere, a region which should be dominated by π^0 decay γ-rays produced via high energy protons colliding with the Earth's upper atmosphere. This signal should definitely not contain any γ-ray line, since the π^0 decay spectrum is well studied by colliders. However, the same analysis found no method by which the line observed in the Earth's albedo could be translated only to the GC, without also producing extremely bright γ-ray line emission in the galactic plane, where it is not observed.

A further analysis of systematics by Bloom et al. (2013) indicated several possible systematics in the Fermi-LAT data, including some evidence pointing towards a decreased instrumental effective area above and below the γ-ray line energy compared to Monte Carlo simulations. This error could potentially produce a γ-ray line, as it would decrease the number of photons compared to expectations both above and below the tentative line. However, no systematic observed in the Fermi-LAT data had the appropriate strength in order to explain the entire γ-ray line signal observed at the GC. Finally, a recent analysis by Whiteson (2013) found that the 130 GeV line may also exist in photons taken from within

5° of the sun. Again, this appears to be a problem for dark matter interpretations of the γ-ray line, as the sun should not produce monoenergetic photons.

The ultimate fate of the γ-ray line analysis is still extremely uncertain. While astrophysical backgrounds are unlikely, instrumental artifacts still appear very probable. Several efforts are currently underway in order to elucidate the reliability of line observations. By altering the survey strategy of the Fermi-LAT telescope in order to increase the total exposure at the GC, the Fermi-LAT could increase the low number statistics currently hampering our understanding of the γ-ray line phenomenon (Su & Finkbeiner, 2012). Additionally, upcoming observatories such as the Gamma-400 telescope and the H.E.S.S.-II instrument may provide independent tests of the line phenomenon (Bergström et al., 2012).

6.3   Constraints on WIMP Models

In addition to these enticing signals, several important constraints have also been placed on the dark matter cross-section. Perhaps most notably, a systematic stacking of dwarf spheroidal galaxies has ruled out WIMPs below 30 GeV interacting with a cross-section above 3×10^{-26} cm^{-3}s^{-1} (Ackermann et al., 2011). Additionally, data from Xenon100 has placed extremely strong limits on the scattering cross-section with baryonic matter which is several orders of magnitude below previous constraints (Aprile et al., 2011; Angle et al., 2011).

At low energies, an analysis by Regis & Ullio (2008) set constraints on the dark matter cross-section using multiwavelength constraints at radio and X-Ray energies of the point source near the GC. Because the magnetic field strength is expected to be very high in

131

this region, the synchrotron radiation from energetic electrons should be produced promptly. These limits were thus able to set extremely strong limits on the dark matter annihilation cross-section. Notably, constraints from synchrotron radiation were able to rule out dark matter annihilating at the thermal cross-section by four orders of magnitude under specific sets of assumptions. However, these models also rely on extreme extrapolations of the dark matter density profile and magnetic field energy density into the center of the galaxy (on scales of $\sim 10^{-5}$ pc). These extrapolations have not been tested, and are unlikely to hold over such extreme regions.

6.4   Future Progress

In order to set strong constraints on the dark matter parameter space, new instruments, observations, and models will need to be produced. A convincing signal from dark matter annihilation would optimally have three important qualities: (1) it should be clearly separable from instrumental systematics and backgrounds, (2) it should produce consistent signals among multiwavelength scans and in both direct, indirect, and collider searches, (3) it should not violate constraints from any experiment.

In the theater of indirect detection, this requires multiwavelength observations of a single source, using models which are capable of taking into account the technical advantages of both γ-ray and radio observatories. For GC observations, upcoming models will need to be more sophisticated, in order to recreate the complexity of the observed radio morphology while predicting the γ-ray flux from the same models. Any correct model containing both dark matter and astrophysical emission sources should be able to recreate the

entire multiwavelength spectrum, while not exceeding the observed emission in any energy band or region. The upcoming years will be an exciting time for searches of dark matter annihilation, and as we close in on the expected cross-section for dark matter annihilation, more curiosities are likely to present themselves.

Bibliography

Aalseth, C. E., Barbeau, P. S., Bowden, N. S., Cabrera-Palmer, B., Colaresi, J., Collar, J. I., Dazeley, S., de Lurgio, P., & et al. 2011a, Physical Review Letters, 106, 131301

—. 2011b, Physical Review Letters, 106, 131301

Aalseth, C. E., Barbeau, P. S., Colaresi, J., Collar, J. I., Diaz Leon, J., Fast, J. E., Fields, N., Hossbach, T. W., & et al. 2011c, Physical Review Letters, 107, 141301

—. 2011d, Physical Review Letters, 107, 141301

Abazajian, K. N. 2011a, JCAP, 3, 10

—. 2011b, JCAP, 3, 10

Abazajian, K. N., Agrawal, P., Chacko, Z., & Kilic, C. 2010, JCAP, 11, 41

Abazajian, K. N., & Harding, J. P. 2012, JCAP, 1, 41

Abazajian, K. N., & Kaplinghat, M. 2012, PRD, 86, 083511

Abdo, A. A., Ackermann, M., Ajello, M., Allafort, A., Antolini, E., Atwood, W. B., Axelsson, M., Baldini, L., Ballet, J., Barbiellini, G., & et al. 2010a, ApJ Supp, 188, 405

Abdo, A. A., Ackermann, M., Ajello, M., Atwood, W. B., Axelsson, M., Baldini, L., Ballet, J., Band, D. L., Barbiellini, G., Bastieri, D., & et al. 2009a, ApJ Supp, 183, 46

Abdo, A. A., Ackermann, M., Ajello, M., Atwood, W. B., Axelsson, M., Baldini, L., Ballet, J., Barbiellini, G., Baring, M. G., Bastieri, D., & et al. 2010b, ApJ Supplement, 187, 460

Abdo, A. A., Ackermann, M., Ajello, M., Atwood, W. B., Axelsson, M., Baldini, L., Ballet, J., Barbiellini, G., & et al. 2009b, Science, 325, 848

Abdo, A. A., Ackermann, M., Ajello, M., Baldini, L., Ballet, J., Barbiellini, G., Bastieri, D., Bechtol, K., & et al. 2010c, JCAP, 4, 14

Abdo, A. A., Ackermann, M., Ajello, M., Baldini, L., Ballet, J., Barbiellini, G., Bastieri, D., Bellazzini, R., & et al. ????

Abramowski, A., Acero, F., Aharonian, F., Akhperjanian, A. G., Anton, G., Barnacka, A., Barres de Almeida, U., Bazer-Bachi, A. R., & et al. 2011, Physical Review Letters, 106, 161301

Acero, F., Aharonian, F., Akhperjanian, A. G., Anton, G., Barres de Almeida, U., Bazer-Bachi, A. R., Becherini, Y., Behera, B., & et al. 2010a, MNRAS, 402, 1877

Acero, F., Aharonian, F., Akhperjanian, A. G., Anton, G., Barres de Almeida, U., Bazer-Bachi, A. R., Becherini, Y., Behera, B., & HESS Collaboration. 2010b, MNRAS, 402, 1877

Ackermann, M., Ajello, M., Albert, A., Atwood, W. B., Baldini, L., Ballet, J., Barbiellini, G., Bastieri, D., & et al. 2011, Physical Review Letters, 107, 241302

135

Ackermann, M., Ajello, M., Allafort, A., Atwood, W. B., Baldini, L., Barbiellini, G., Bastieri, D., Bechtol, K., & et al. 2012, Physical Review Letters, 108, 011103

Ackermann, M., Ajello, M., Allafort, A., Baldini, L., Ballet, J., Barbiellini, G., Bastieri, D., Bechtol, K., & et al. 2010, JCAP, 5, 25

Adriani, O., Barbarino, G. C., Bazilevskaya, G. A., Bellotti, R., Boezio, M., Bogomolov, E. A., Bonechi, L., Bongi, M., & et al. 2009a, Nature, 458, 607

—. 2009b, Nature, 458, 607

Aguilar, M., Alberti, G., Alpat, B., Alvino, A., Ambrosi, G., Andeen, K. Anderhub, H., Arruda, L., & et al. 2013, PRL, 110

Aharonian, F. 2005, in KITP Conference: The Paradoxes of Massive Black Holes: A Case Study in the Milky Way

Aharonian, F., Akhperjanian, A. G., Anton, G., Barres de Almeida, U., Bazer-Bachi, A. R., Becherini, Y., Behera, B., Bernlöhr, K., & et al. 2009a, A&A, 503, 817

—. 2009b, A&A, 503, 817

Aharonian, F., Akhperjanian, A. G., Aye, K.-M., Bazer-Bachi, A. R., Beilicke, M., Benbow, W., Berge, D., Berghaus, P., & et al. 2004a, Astroparticle Physics, 22, 109

—. 2004b, A&A, 425, L13

Aharonian, F., Akhperjanian, A. G., Barres de Almeida, U., Bazer-Bachi, A. R., Becherini, Y., Behera, B., Benbow, W., Bernlöhr, K., & et al. 2008a, A&A, 492, L25

—. 2008b, A&A, 492, L25

Aharonian, F., Akhperjanian, A. G., Bazer-Bachi, A. R., Beilicke, M., Benbow, W., Berge, D., Bernlöhr, K., Boisson, C., & et al. 2006a, Nature, 439, 695

—. 2006b, Physical Review Letters, 97, 221102

—. 2006c, Physical Review Letters, 97, 221102

—. 2006d, A&A, 457, 899

—. 2006e, ApJ, 636, 777

Aharonian, F., Akhperjanian, A. G., Bazer-Bachi, A. R., Beilicke, M., Benbow, W., Berge, D., Bernlöhr, K., C., B., & et al. 2006f, ApJ, 636, 777

Aharonian, F., Khangulyan, D., & Malyshev, D. 2012, AAP, 547, A114

Aharonian, F., & Neronov, A. 2005a, ApJ, 619, 306

—. 2005b, Astrophysics and Space Science, 300, 255

—. 2005c, Astrophysics and Space Science, 300, 255

Ahmed, Z., Akerib, D. S., Arrenberg, S., Bailey, C. N., Balakishiyeva, D., Baudis, L., Bauer, D. A., Brink, P. L., & et al. 2011, Physical Review Letters, 106, 131302

Akerib, D. S., Attisha, M. J., Baudis, L., Bauer, D. A., Bolozdynya, A. I., Brink, P. L., Bunker, R., Cabrera, B., & et al. 2010, PRD, 82, 122004

Albert, J., Aliu, E., Anderhub, H., Antoranz, P., Armada, A., Asensio, M., Baixeras, C., Barrio, J. A., & et al. 2006, ApJL, 638, L101

Alfvén, H. 1942, Nature, 150, 405

Aloisio, R., Berezinsky, V., & Gazizov, A. 2009, ApJ, 693, 1275

Anantharamaiah, K. R., Pedlar, A., Ekers, R. D., & Goss, W. M. 1991, MNRAS, 249, 262

Angle, J., Aprile, E., Arneodo, F., Baudis, L., Bernstein, A., Bolozdynya, A. I., Coelho, L. C. C., Dahl, C. E., & et al. 2011, Physical Review Letters, 107, 051301

Angloher, G., Bauer, M., Bavykina, I., Bento, A., Bucci, C., Ciemniak, C., Deuter, G., von Feilitzsch, F., & et al. 2012, European Physical Journal C, 72, 1971

Aprile, E., Arisaka, K., Arneodo, F., Askin, A., Baudis, L., Behrens, A., Bokeloh, K., Brown, E., & et al.. 2011, Physical Review Letters, 107, 131302

Arkani-Hamed, N., Finkbeiner, D. P., Slatyer, T. R., & Weiner, N. 2009, PRD, 79, 015014

Atoyan, A., & Dermer, C. D. 2004, ApJL, 617, L123

Atwood, W. B., Abdo, A. A., Ackermann, M., Althouse, W., Anderson, B., Axelsson, M., Baldini, L., Ballet, J., Band, D. L., Barbiellini, G., & et al. 2009, ApJ, 697, 1071

Babcock, H. W. 1939, Lick Observatory Bulletin, 19, 41

Baganoff, F. K., Bautz, M. W., Brandt, W. N., Chartas, G., Feigelson, E. D., Garmire, G. P., Maeda, Y., Morris, M., Ricker, G. R., Townsley, L. K., & Walter, F. 2001, Nature, 413, 45

Ballantyne, D. R., Melia, F., Liu, S., & Crocker, R. M. 2007a, ApJL, 657, L13

—. 2007b, ApJL, 657, L13

Barger, V., Gao, Y., Keung, W.-Y., Marfatia, D., & Shaughnessy, G. 2009, Physics Letters B, 678, 283

Becklin, E. E., Gatley, I., & Werner, M. W. 1982a, ApJ, 258, 135

—. 1982b, ApJ, 258, 135

Bélanger, G., Goldwurm, A., Goldoni, P., Paul, J., Terrier, R., Falanga, M., Ubertini, P., Bazzano, A., Del Santo, M., Winkler, C., Parmar, A. N., Kuulkers, E., Ebisawa, K., Roques, J. P., Lund, N., & Melia, F. 2004, ApJL, 601, L163

Berezinsky, V., Bottino, A., & Mignola, G. 1994, Physics Letters B, 325, 136

Berezinsky, V. S., Gurevich, A. V., & Zybin, K. P. 1992, Physics Letters B, 294, 221

Bergström, L. 2009, New Journal of Physics, 11, 105006

Bergström, L., Bertone, G., Conrad, J., Farnier, C., & Weniger, C. 2012, JCAP, 11, 25

Bergström, L., Ullio, P., & Buckley, J. H. 1998, Astroparticle Physics, 9, 137

Bernabei, R., Belli, P., Cappella, F., Cerulli, R., Dai, C. J., D'Angelo, A., He, H. L., Incicchitti, A., Kuang, H. H., Ma, X. H., Montecchia, F., Nozzoli, F., Prosperi, D., Sheng, X. D., Wang, R. G., & Ye, Z. P. 2010a, European Physical Journal C, 67, 39

—. 2010b, European Physical Journal C, 67, 39

Bertone, G., Hooper, D., & Silk, J. 2005, Physics Reports, 405, 279

Blandford, R., & Eichler, D. 1987, Physics Reports, 154, 1

Blitz, L., Bloemen, J. B. G. M., Hermsen, W., & Bania, T. M. 1985, A&A, 143, 267

Bloom, E., Charles, E., Izaguirre, E., Snyder, A., Albert, A., Winer, B., Yang, Z., & Essig, R. 2013, ArXiv e-prints

Blumenthal, G. R., Faber, S. M., Flores, R., & Primack, J. R. 1986a, ApJ, 301, 27

—. 1986b, ApJ, 301, 27

Blumenthal, G. R., Faber, S. M., Primack, J. R., & Rees, M. J. 1984, Nature, 311, 517

Blumenthal, G. R., Pagels, H., & Primack, J. R. 1982, Nature, 299, 37

Boldyrev, S., & Yusef-Zadeh, F. 2006, ApJL, 637, L101

Bond, J. R., & Szalay, A. S. 1983, ApJ, 274, 443

Boyarsky, A., Malyshev, D., & Ruchayskiy, O. 2011, Physics Letters B, 705, 165

Bradač, M., Clowe, D., Gonzalez, A. H., Marshall, P., Forman, W., Jones, C., Markevitch, M., Randall, S., Schrabback, T., & Zaritsky, D. 2006, ApJ, 652, 937

Bradford, C. M., Stacey, G. J., Nikola, T., Bolatto, A. D., Jackson, J. M., Savage, M. L., & Davidson, J. A. 2005, ApJ, 623, 866

Braun, I., Bolz, O., van Eldik, C., Hermann, G., Hinton, J., & Hofmann, W. 2008, Journal of Physics Conference Series, 110, 062003

Brogan, C. L., Nord, M., Kassim, N., Lazio, J., & Anantharamaiah, K. 2003, Astronomische Nachrichten Supplement, 324, 17

Buckley, M. R., & Hooper, D. 2010, PRD, 82, 063501

Burn, B. J. 1966, MNRAS, 133, 67

Carlson, E., Linden, T., Profumo, S., & Weniger, C. 2013a, ArXiv e-prints

—. 2013b, ArXiv e-prints

Casse, F., Lemoine, M., & Pelletier, G. 2002, PRD, 65, 023002

Catena, R., & Ullio, P. 2010a, JCAP, 8, 4

—. 2010b, JCAP, 8, 4

CDMS Collaboration, Agnese, R., Ahmed, Z., Anderson, A. J., Arrenberg, S., Balak-
  ishiyeva, D., Basu Thakur, R., Bauer, D. A., Billard, J., & et al. 2013a, ArXiv e-prints

—. 2013b, ArXiv e-prints

Chandran, B. D. G., Cowley, S. C., & Morris, M. 2000, ApJ, 528, 723

Chernyakova, M., Malyshev, D., Aharonian, F. A., Crocker, R. M., & Jones, D. I. 2011,
  ApJ, 726, 60

Cholis, I., Dobler, G., Finkbeiner, D. P., Goodenough, L., & Weiner, N. 2009, PRD, 80,
  123518

Christopher, M. H., Scoville, N. Z., Stolovy, S. R., & Yun, M. S. 2005, ApJ, 622, 346

Cirelli, M., Kadastik, M., Raidal, M., & Strumia, A. 2009, Nuclear Physics B, 813, 1

Clowe, D., Bradač, M., Gonzalez, A. H., Markevitch, M., Randall, S. W., Jones, C., &
  Zaritsky, D. 2006, ApJL, 648, L109

Collar, J. I. 2010, ArXiv e-prints

—. 2011a, ArXiv e-prints

—. 2011b, ArXiv e-prints

Cowsik, R., & McClelland, J. 1973, ApJ, 180, 7

Crocker, R. M., & Aharonian, F. 2011, Physical Review Letters, 106, 101102

Crocker, R. M., Jones, D. I., Melia, F., Ott, J., & Protheroe, R. J. 2010, Nature, 463, 65

CTA Collaboration. 2011, ArXiv e-prints

CTA Consortium, T. 2011, ArXiv e-prints

DeMarco, D., Blasi, P., & Stanev, T. 2007, JCAP, 6, 27

Demleitner, M., Accomazzi, A., Eichhorn, G., Grant, C. S., Kurtz, M. J., & Murray, S. S.
  2001, in Astronomical Society of the Pacific Conference Series, Vol. 238, Astronomical
  Data Analysis Software and Systems X, ed. F. R. Harnden, Jr., F. A. Primini, & H. E.
  Payne, 321

Diemand, J., Kuhlen, M., Madau, P., Zemp, M., Moore, B., Potter, D., & Stadel, J. 2008a,
  Nature, 454, 735

—. 2008b, Nature, 454, 735

Diemand, J., Zemp, M., Moore, B., Stadel, J., & Carollo, C. M. 2005, MNRAS, 364, 665

Dine, M., & Fischler, W. 1983, Physics Letters B, 120, 137

Dobler, G. 2012, ApJ, 750, 17

Dobler, G., Finkbeiner, D. P., Cholis, I., Slatyer, T., & Weiner, N. 2010, ApJ, 717, 825

Dodelson, S., Hooper, D., & Serpico, P. D. 2008, PRD, 77, 063512

Doroshkevich, A. G., Khlopov, M. I., Sunyaev, R. A., Szalay, A. S., & Zeldovich, I. B. 1981,
   Annals of the New York Academy of Sciences, 375, 32

Dugger, L., Jeltema, T. E., & Profumo, S. 2010, JCAP, 12, 15

Ferrière, K. 2009, A&A, 505, 1183

—. 2012, A&A, 540, A50

Ferriere, K. 2012, ArXiv e-prints

Ferrière, K., Gillard, W., & Jean, P. 2007, A&A, 467, 611

Finkbeiner, D. P. 2004, ArXiv Astrophysics e-prints

Finkbeiner, D. P., Su, M., & Weniger, C. 2013, JCAP, 1, 29

Fixsen, D. J., Kogut, A., Levin, S., Limon, M., Lubin, P., Mirel, P., Seiffert, M., Singal, J.,
   Wollack, E., Villela, T., & Wuensche, C. A. 2009, ArXiv e-prints

—. 2011, ApJ, 734, 5

Fornengo, N., Lineros, R., Regis, M., & Taoso, M. 2011, Physical Review Letters, 107,
   A261302

Fox, P. J., Harnik, R., Kopp, J., & Tsai, Y. 2011, PRD, 84, 014028

Frenk, C. S., White, S. D. M., & Davis, M. 1983, ApJ, 271, 417

Fryer, C. L., Liu, S., Rockefeller, G., Hungerford, A., & Belanger, G. 2007, ApJ, 659, 389

Galli, S., Iocco, F., Bertone, G., & Melchiorri, A. 2011, PRD, 84, 027302

Geringer-Sameth, A., & Koushiappas, S. M. 2011, Physical Review Letters, 107, 241303

Ghez, A. M., Wright, S. A., Matthews, K., Thompson, D., Le Mignant, D., Tanner, A., Hornstein, S. D., Morris, M., Becklin, E. E., & Soifer, B. T. 2004, ApJL, 601, L159

Gnedin, O. Y., Ceverino, D., Gnedin, N. Y., Klypin, A. A., Kravtsov, A. V., Levine, R., Nagai, D., & Yepes, G. 2011a, ArXiv e-prints

—. 2011b, ArXiv e-prints

Gnedin, O. Y., Kravtsov, A. V., Klypin, A. A., & Nagai, D. 2004a, ApJ, 616, 16

—. 2004b, ApJ, 616, 16

Goldberg, H. 1983, Physical Review Letters, 50, 1419

Gondolo, P., Edsjö, J., Ullio, P., Bergström, L., Schelke, M., & Baltz, E. A. 2004, JCAP, 7, 8

Goodenough, L., & Hooper, D. 2009, ArXiv e-prints

Goodman, J., Ibe, M., Rajaraman, A., Shepherd, W., Tait, T. M. P., & Yu, H.-B. 2010, PRD, 82, 116010

—. 2011, Physics Letters B, 695, 185

Governato, F., Brook, C., Mayer, L., Brooks, A., Rhee, G., Wadsley, J., Jonsson, P., Willman, B., Stinson, G., Quinn, T., & Madau, P. 2010, Nature, 463, 203

Graff, D. S., & Freese, K. 1996, ApJL, 456, L49

Gray, A. D., Nicholls, J., Ekers, R. D., & Cram, L. E. 1995, ApJ, 448, 164

Heyvaerts, J., Norman, C., & Pudritz, R. E. 1988, ApJ, 330, 718

Hinton, J. A. 2004, NAR, 48, 331

Hinton, J. A., & Aharonian, F. A. 2007, ApJ, 657, 302

Hooper, D., , D. P., & Dobler, G. 2007, PRD, 76, 083012

Hooper, D. 2012, ArXiv e-prints

Hooper, D., Belikov, A. V., Jeltema, T. E., Linden, T., Profumo, S., & Slatyer, T. R. 2012a, PRD, 86, 103003

Hooper, D., Blasi, P., & Dario Serpico, P. 2009, JCAP, 1, 25

Hooper, D., Cholis, I., Linden, T., Siegal-Gaskins, J., & Slatyer, T. 2013, ArXiv e-prints

Hooper, D., Collar, J. I., Hall, J., McKinsey, D., & Kelso, C. M. 2010, PRD, 82, 123509

Hooper, D., de la Calle Perez, I., Silk, J., Ferrer, F., & Sarkar, S. 2004a, JCAP, 9, 2

—. 2004b, JCAP, 9, 2

Hooper, D., & Dingus, B. L. 2004, PRD, 70, 113007

Hooper, D., & Goodenough, L. 2011a, Physics Letters B, 697, 412

—. 2011b, Physics Letters B, 697, 412

—. 2011c, Physics Letters B, 697, 412

Hooper, D., & Kelso, C. 2011, PRD, 84, 083001

Hooper, D., Kelso, C., & Queiroz, F. S. 2012b, ArXiv e-prints

Hooper, D., & Linden, T. 2011a, PRD, 83, 083517

—. 2011b, PRD, 83, 083517

—. 2011c, PRD, 84, 123005

Hooper, D., & Slatyer, T. R. 2013, ArXiv e-prints

Hütsi, G., Chluba, J., Hektor, A., & Raidal, M. 2011, A&A, 535, A26

Iocco, F., Pato, M., Bertone, G., & Jetzer, P. 2011, JCAP, 11, 29

Jokipii, J. R. 1966, ApJ, 146, 480

—. 1971, Reviews of Geophysics and Space Physics, 9, 27

Jones, F. C., & Ellison, D. C. 1991, Space Science Reviews, 58, 259

Kahn, F. D., & Woltjer, L. 1959, ApJ, 130, 705

Kalberla, P. M. W., & Kerp, J. 2009, Annual Review of Astron and Astrophys, 47, 27

Kamae, T., Karlsson, N., Mizuno, T., Abe, T., & Koi, T. 2006, ApJ, 647, 692

Kassim, N. E., Larosa, T. N., Lazio, T. J. W., & Hyman, S. D. 1999, in Astronomical
  Society of the Pacific Conference Series, Vol. 186, The Central Parsecs of the Galaxy, ed.
  H. Falcke, A. Cotera, W. J. Duschl, F. Melia, & M. J. Rieke, 403

Kolmogorov, A. 1941, Akademiia Nauk SSSR Doklady, 30, 301

Kosack, K., Badran, H. M., Bond, I. H., Boyle, P. J., Bradbury, S. M., Buckley, J. H., Carter-Lewis, D. A., Celik, O., & et al. 2004, ApJL, 608, L97

Kuchowicz, B. 1969, Fortschritte der Physik, 17, 517

Kusunose, M., & Takahara, F. 2012, ArXiv e-prints

Lang, C. C., Anantharamaiah, K. R., Kassim, N. E., & Lazio, T. J. W. 1999a, ApJL, 521, L41

Lang, C. C., Morris, M., & Echevarria, L. 1999b, ApJ, 526, 727

LaRosa, T. N., Brogan, C. L., Shore, S. N., Lazio, T. J., Kassim, N. E., & Nord, M. E. 2005, ApJL, 626, L23

LaRosa, T. N., Kassim, N. E., Lazio, T. J. W., & Hyman, S. D. 2000a, Astronomical Journal, 119, 207

—. 2000b, Astronomical Journal, 119, 207

LaRosa, T. N., Lazio, T. J. W., & Kassim, N. E. 2001, ApJ, 563, 163

LaRosa, T. N., Nord, M. E., Lazio, T. J. W., & Kassim, N. E. 2004, ApJ, 607, 302

Law, C., & Yusef-Zadeh, F. 2004, ApJ, 611, 858

Law, C. J., Yusef-Zadeh, F., & Cotton, W. D. 2008a, ApJ Supp, 177, 515

Law, C. J., Yusef-Zadeh, F., Cotton, W. D., & Maddalena, R. J. 2008b, ApJ Supp, 177, 255

Lazarian, A., Kowal, G., Vishniac, E., & de Gouveia Dal Pino, E. 2011, Planetary Space Science, 59, 537

Lee, B. W., & Weinberg, S. 1977, Physical Review Letters, 39, 165

Lesch, H., & Reich, W. 1992, A&A, 264, 493

Lesch, H., Schlickeiser, R., & Crusius, A. 1988, A&A, 200, L9

Levine, R., Gnedin, N. Y., Hamilton, A. J. S., & Kravtsov, A. V. 2008, ApJ, 678, 154

Lieb, S., Lesch, H., & Birk, G. T. 2004, A&A, 419, 161

Linden, T., Hooper, D., & Yusef-Zadeh, F. 2011, ApJ, 741, 95

Linden, T., Lovegrove, E., & Profumo, S. 2012, ApJ, 753, 41

Linden, T., & Profumo, S. 2013, ArXiv e-prints

Lisanti, M., & Spergel, D. N. 2012, Physics of the Dark Universe, 1, 155

Liszt, H. S., & Spiker, R. W. 1995, ApJ Supp, 98, 259

Liu, S., Melia, F., Petrosian, V., & Fatuzzo, M. 2006a, ApJ, 647, 1099

—. 2006b, ApJ, 647, 1099

Liu, S., Petrosian, V., Melia, F., & Fryer, C. L. 2006c, ApJ, 648, 1020

—. 2006d, ApJ, 648, 1020

Longair, M. S. 2010, High Energy Astrophysics, ed. Longair, M. S.

Lyubarsky, Y. E. 2005, MNRAS, 358, 113

Malkov, M. A., & O'C Drury, L. 2001, Reports on Progress in Physics, 64, 429

Malyshev, D., Cholis, I., & Gelfand, J. D. 2010, ApJ, 722, 1939

Mayer-Hasselwander, H. A., Bertsch, D. L., Dingus, B. L., Eckart, A., Esposito, J. A.,
  Genzel, R., Hartman, R. C., Hunter, S. D., & et. al. 1998, A&A, 335, 161

McKinney, J. C., & Uzdensky, D. A. 2012, MNRAS, 419, 573

Milgrom, M. 1983, ApJ, 270, 365

Montero-Castaño, M., Herrnstein, R. M., & Ho, P. T. P. 2009, ApJ, 695, 1477

Morris, M., & Yusef-Zadeh, F. 1989, ApJ, 343, 703

Nakanishi, H., & Sofue, Y. 2003, Publications of the ASJ, 55, 191

Navarro, J. F., Frenk, C. S., & White, S. D. 1997, Astrophys.J., 490, 493

Navarro, J. F., Frenk, C. S., & White, S. D. M. 1996a, ApJ, 462, 563

—. 1996b, ApJ, 462, 563

—. 1997, ApJ, 490, 493

Navarro, J. F., Hayashi, E., Power, C., Jenkins, A. R., Frenk, C. S., White, S. D. M.,
  Springel, V., Stadel, J., & Quinn, T. R. 2004, MNRAS, 349, 1039

Navarro, J. F., Ludlow, A., Springel, V., Wang, J., Vogelsberger, M., White, S. D. M.,
  Jenkins, A., Frenk, C. S., & Helmi, A. 2010, MNRAS, 402, 21

Nicholls, J., & Gray, A. D. 1993, Proceedings of the Astronomical Society of Australia, 10,
  233

Nolan, P. L., Abdo, A. A., Ackermann, M., Ajello, M., Allafort, A., Antolini, E., Atwood, W. B., Axelsson, M., Baldini, L., Ballet, J., & et al. 2012, ApJ Supplement, 199, 31

Nord, M. E., Lazio, T. J. W., Kassim, N. E., Hyman, S. D., LaRosa, T. N., Brogan, C. L., & Duric, N. 2004, Astronomical Journal, 128, 1646

Oh, S.-H., Brook, C., Governato, F., Brinks, E., Mayer, L., de Blok, W. J. G., Brooks, A., & Walter, F. 2011, Astronomical Journal, 142, 24

Oort, J. H. 1932, BAIN, 6, 249

—. 1940, ApJ, 91, 273

Ostriker, J. P., & Peebles, P. J. E. 1973, ApJ, 186, 467

Paczynski, B. 1986, ApJ, 304, 1

Pagels, H., & Primack, J. R. 1982, Physical Review Letters, 48, 223

Peñarrubia, J., Pontzen, A., Walker, M. G., & Koposov, S. E. 2012, ApJL, 759, L42

Pedlar, A., Anantharamaiah, K. R., Ekers, R. D., Goss, W. M., van Gorkom, J. H., Schwarz, U. J., & Zhao, J.-H. 1989, ApJ, 342, 769

Planck Collaboration, Ade, P. A. R., Aghanim, N., Armitage-Caplan, C., Arnaud, M., Ashdown, M., Atrio-Barandela, F., Aumont, J., Baccigalupi, C., Banday, A. J., & et al. 2013, ArXiv e-prints

Preskill, J., Wise, M. B., & Wilczek, F. 1983, Physics Letters B, 120, 127

Profumo, S. 2005, PRD, 72, 103521

—. 2012, Central European Journal of Physics, 10, 1

Rajaraman, A., Shepherd, W., Tait, T. M. P., & Wijangco, A. M. 2011, PRD, 84, 095013

Regis, M. 2011, personal communication

Regis, M., & Ullio, P. 2008, PRD, 78, 043505

Reich, W. 2003, A&A, 401, 1023

Reich, W., Sofue, Y., & Matsuo, H. 2000, Pub. of the ASJ, 52, 355

Requena-Torres, M. A., Guesten, R., Weiss, A., Harris, A. I., Marin-Pintado, J., Stutzki, J., Klein, B., Heyminck, S., & Risacher, C. 2012, ArXiv e-prints

Roberts, M. S., & Whitehurst, R. N. 1975, ApJ, 201, 327

Rockefeller, G., Fryer, C. L., Melia, F., & Warren, M. S. 2004, ApJ, 604, 662

Rosner, R., & Bodo, G. 1996, ApJL, 470, L49

Rubin, V. C., & Ford, Jr., W. K. 1970, ApJ, 159, 379

Ryden, B. S., & Gunn, J. E. 1987a, ApJ, 318, 15

—. 1987b, ApJ, 318, 15

Schödel, R., Merritt, D., & Eckart, A. 2009, A&A, 502, 91

Seiffert, M., Fixsen, D. J., Kogut, A., Levin, S. M., Limon, M., Lubin, P. M., Mirel, P., Singal, J., Villela, T., Wollack, E., & Wuensche, C. A. 2011, ApJ, 734, 6

Sjöstrand, T., Edén, P., Friberg, C., Lönnblad, L., Miu, G., Mrenna, S., & Norrbin, E. 2001a, Computer Physics Communications, 135, 238

—. 2001b, Computer Physics Communications, 135, 238

Slatyer, T. R., Padmanabhan, N., & Finkbeiner, D. P. 2009, PRD, 80, 043526

Sofue, Y., & Fujimoto, M. 1987, Pub. of the ASJ, 39, 843

Sofue, Y., Inoue, M., Handa, T., Tsuboi, M., Hirabayashi, H., Morimoto, M., & Akabane, K. 1986, Pub. of the ASJ, 38, 475

Sofue, Y., Murata, Y., & Reich, W. 1992, Pub. of the ASJ, 44, 367

Springel, V., Wang, J., Vogelsberger, M., Ludlow, A., Jenkins, A., Helmi, A., Navarro, J. F., Frenk, C. S., & White, S. D. M. 2008, MNRAS, 391, 1685

Steigman, G. 1979a, Annual Review of Nuclear and Particle Science, 29, 313

—. 1979b, Annual Review of Nuclear and Particle Science, 29, 313

Strong, A. W., & Moskalenko, I. V. 1998, ApJ, 509, 212

Su, M., & Finkbeiner, D. P. 2012, ArXiv e-prints

Su, M., Slatyer, T. R., & Finkbeiner, D. P. 2010, ApJ, 724, 1044

Thompson, D. J., Bertsch, D. L., Fichtel, C. E., Hartman, R. C., Hofstadter, R., Hughes, E. B., Hunter, S. D., Hughlock, B. W., & et al. 1993, ApJS, 86, 629

Tisserand, P., Le Guillou, L., Afonso, C., Albert, J. N., Andersen, J., Ansari, R., Aubourg, É., Bareyre, P., & et al. 2007, AAP, 469, 387

Tsuboi, M., Inoue, M., Handa, T., Tabara, H., Kato, T., Sofue, Y., & Kaifu, N. 1986, Astronomical Journal, 92, 818

Tsuboi, M., Kawabata, T., Kasuga, T., Handa, T., & Kato, T. 1995, Pub. of the ASJ, 47, 829

van den Bergh, S. 1999, PASP, 111, 657

Vitale, V., Morselli, A., & for the Fermi/LAT Collaboration. 2009a, ArXiv e-prints

—. 2009b, ArXiv e-prints

—. 2009c, ArXiv e-prints

Walker, M. G., & Peñarrubia, J. 2011, ApJ, 742, 20

Wang, Q. D., Gotthelf, E. V., & Lang, C. C. 2002, Nature, 415, 148

Weniger, C. 2012, JCAP, 8, 7

Wharton, R. S., Chatterjee, S., Cordes, J. M., Deneva, J. S., & Lazio, T. J. W. 2012, ApJ, 753, 108

White, S. D. M., Frenk, C. S., & Davis, M. 1983, ApJL, 274, L1

Whiteson, D. 2013, ArXiv e-prints

Yusef-Zadeh, F. 2003, ApJ, 598, 325

Yusef-Zadeh, F., Goss, W. M., Roberts, D. A., Robinson, B., & Frail, D. A. 1999, ApJ, 527, 172

Yusef-Zadeh, F., Hewitt, J. W., & Cotton, W. 2004, ApJ Supp, 155, 421

Yusef-Zadeh, F., Melia, F., & Wardle, M. 2000, Science, 287, 85

Yusef-Zadeh, F., & Morris, M. 1987, Astronomical Journal, 94, 1178

Yusef-Zadeh, F., Morris, M., & Chance, D. 1984, Nature, 310, 557

Zaharijas, G., & Hooper, D. 2006, PRD, 73, 103501

Zanotti, O., & Dumbser, M. 2011, MNRAS, 418, 1004

Zhang, L., & Cheng, K. S. 2001, A&A, 368, 1063

Zwicky, F. 1933, Helvetica Physica Acta, 6, 110